Vertical Hydraulic Transport for deep sea mining

a study into flow assurance

Jort van Wijk

VERTICAL HYDRAULIC TRANSPORT FOR DEEP SEA MINING

A STUDY INTO FLOW ASSURANCE

VERTICAL HYDRAULIC TRANSPORT FOR DEEP SEA MINING

A STUDY INTO FLOW ASSURANCE

Proefschrift

ter verkrijging van de graad van doctor
aan de Technische Universiteit Delft,
op gezag van de Rector Magnificus prof. ir. K. C. A. M. Luyben,
voorzitter van het College voor Promoties,
in het openbaar te verdedigen op maandag 8 februari 2016 om 15:00 uur

door

Jort Merijn VAN WIJK

ingenieur in de offshore- en baggertechnologie
geboren te Dordrecht, Nederland.

Dit proefschrift is goedgekeurd door de:

promotor: Prof. dr. ir. C. van Rhee en
copromotor: Dr. ir. A.M. Talmon

Samenstelling promotiecommissie:

Rector Magnificus,	voorzitter
Prof. dr. ir. C. van Rhee,	Technische Universiteit Delft, promotor
Dr. ir. A.M. Talmon,	Technische Universiteit Delft, copromotor
Onafhankelijke leden:	
Prof. dr. ir. R.A.W.M. Henkes,	Technische Universiteit Delft
Prof. dr. ir. R.F. Mudde,	Technische Universiteit Delft
Prof. dr. ir. W.S.J. Uijttewaal,	Technische Universiteit Delft
Prof. dr. ing. V. Matoušek,	Czech Technical University in Prague, Tsjechië
Prof. dr. R.S. Sanders,	University of Alberta, Canada

The research presented in this thesis has been financed by Royal IHC, The Netherlands and the European Union Seventh Framework Programme for research, technological development and demonstration under Grant Agreement no. 604500:

Keywords: Vertical Hydraulic Transport, Flow Assurance, Deep Sea Mining

Printed by: Drukkerij Haveka, Alblasserdam

Front & Back: A density wave propagating through a vertical transparent pipe.

ISBN 978-90-9029-540-4

An electronic version of this dissertation is available at
http://repository.tudelft.nl/.

Voor mijn vader

SUMMARY

In this thesis the specific case of vertical hydraulic transport for deep sea mining applications is investigated. Transport distances from sea floor to sea surface are often hundreds to thousands of meters, and the combination of these distances with solid particles with different shapes and sizes poses the risk of riser blockage.

During the design phase of a transport system knowledge about the internal flow is crucial. In this thesis a one dimensional flow model is presented for this purpose. The model solves the continuity equation and conservation of momentum for the entire mixture of solids and liquid. The particle size distribution of the solids at hand is discretized in the model, and for each fraction the advection-diffusion equation is solved. The slip velocity of the solid phase is modelled with hindered settling theory, which is experimentally validated in this thesis for use with relatively large particles. The axial dispersion coefficient in the advection-diffusion equation has an upper limit given by Taylor dispersion, and it has an empirical correction taking into account particle inertia based on experiments described in this thesis.

There are different mechanisms potentially leading to riser blockage. The most important one in this thesis is the merging and overtaking process of batches with different transport velocities. The second mechanism is the formation of wall attached clusters as seen for flat particles. The third mechanism is the occurrence of density waves that could grow into solid plugs.

Clustering of flat particles and the associated risk of riser blockage is related to particle shape on one hand and the relative particle size on the other. The smaller the sphericity (i.e. the flatter the particle), the more the particle tends to form clusters, and the larger the particle is compared to the riser, the larger the risk it forms a wall attached cluster and grows into a blockage. The occurrence of density waves has been investigated with a fluidization experiment and a transport experiment. It proves that the stability of the transport process is larger than the stability of the fluidization processes investigated, and the risk of riser blockage due to density waves seems no issue. The one dimensional flow model does not hold for irregularly shaped particles and the model does not include the formation of clusters or density waves.

When the riser is loaded with consecutive batches with increasing transport velocities, merging and overtaking of batches causes formation of highly concentrated plugs. In this thesis this mechanism has been experimentally investigated. It proves that not only relative particle velocity, but also relative particle size between fractions plays an important role. This phenomenon follows from simulation with the 1DVHT model as well, based on hindered settling theory, but criteria on the relative particle size related to plug formation are not included.

Once a plug has developed it is important to know how its properties relate to the friction it exerts on the riser, because the amount of friction determines the risk of blockage. The general models for wall friction of mixtures as used in the one dimensional model consist of contributions by the fluid phase and the suspended solids, and the latter shows infinite friction when the volume fraction of solids reaches the maximum, which is not realistic.

In this thesis the principles of soil mechanics have been used to propose an alternative friction model for layered sediment plugs. It has been shown by means of an experiment that the relative permeability of the layers and the order of layering with respect to the flow direction determine the wall friction. The model has been shown to perform well compared to laboratory measurements. The model has been implemented in the one dimensional flow model.

Both simulations and experiments show that the development of a highly concentrated plug in a vertical transport system is well possible, and they show it could actually block the riser, but the chance for the formation of such a blockage is only small. The inlet conditions in the riser and the grain properties should meet a specific set of requirements for the riser to get blocked, but these conditions are not probable to occur when the mixture is well-mixed before entering the riser.

SAMENVATTING

Verticaal Hydraulisch Transport. Soms voorgesteld als de meest eenvoudige variant van hydraulisch transport, maar op zichzelf complex genoeg om er een heel proefschrift aan te wijden.

In dit proefschrift wordt het specifieke geval van verticaal transport voor toepassing in de diepzee mijnbouw besproken, waarbij de transportafstanden honderden tot duizenden meters van zeebodem tot zeespiegel kunnen bedragen. De combinatie van lange transportafstanden en getransporteerd materiaal van allerlei vormen en grootten brengt het risico op blokkade van het transportsysteem met zich mee.

Men zou op voorhand, al tijdens het ontwerpproces, willen weten hoe de interne stroming in een verticaal transportsysteem eruit ziet. Daartoe is in dit proefschrift een eendimensionaal model opgezet. Het model lost de behoudswetten op voor het gehele mengsel van vaste stof en de draagvloeistof. Het bevat een gediscretiseerde deeltjesverdeling, en voor iedere fractie van de vaste stof wordt de transportvergelijking opgelost. De relatieve snelheid van de deeltjes is gemodelleerd met de theorie van gehinderde deeltjesbezinking, die bovendien experimenteel is gevalideerd voor de relatief grote deeltjes waarvan sprake is in diepzeemijnbouw toepassingen. De axiale dispersie coefficiënt in de transportvergelijking heeft Taylor dispersie als bovengrens en een empirische correctie voor de deeltjestraagheid, eveneens experimenteel onderbouwd.

Blokkades kunnen langs verschillende wegen plaatsvinden. De belangrijkste daarvan is de interactie tussen fracties met verschillende transportsnelheden, gevolgd door het clusteren van met name platte deeltjes, en het optreden van dichtheidsgolven in een transportsysteem. Het eerste mechanisme is in dit proefschrift uitvoerig beschreven met een speciaal experiment.

Het tweede en derde mechanisme zijn eveneens experimenteel verkend in dit proefschrift. Clustervorming en de daarmee samenhangende kans op verstopping is sterk gerelateerd aan enerzijds de vorm van de deeltjes, en anderzijds aan de relatieve deeltjesgrootte ten opzichte van de leiding. Hoe platter het deeltje, hoe meer het clustert met andere deeltjes, en hoe groter het deeltje ten opzichte van de transportleiding, hoe eerder een cluster zal vormen aan de wand van de leiding en zal uitgroeien tot een verstopping. Het optreden van dichtheidsgolven is onderzocht met zowel een fluidisatieproef als met een transportproef. Het blijkt dat tijdens het transport van materiaal de stabiliteit van het proces groter is dan tijdens fluidisatie, en de kans op blokkade ten gevolge van groeiende dichtheidsgolven lijkt niet aan de orde te zijn. Het stromingsmodel voorziet niet in simulaties van transport van zeer grillig gevormde deeltjes en het optreden van dichtheidsgolven.

Uit simulaties met het stromingsmodel blijkt dat, wanneer de transportleiding op ongelukkige wijze wordt beladen met opeenvolgende fracties met oplopende transportsnelheid van de fracties, er zich een hooggeconcentreerde prop kan vormen in de leiding. Dit hypothetische geval is in dit proefschrift experimenteel aangetoond met een

speciaal daarvoor geconstrueerde proefopstelling. Het blijkt dat niet alleen de relatieve deeltjessnelheid van belang is, maar ook de relatieve korrelgrootten tussen de opeenvolgende fracties.

Wanneer zich een prop vormt is het zeer interessant om te weten hoeveel wrijving een dergelijke prop uitoefent op de transportleiding, omdat de hoeveelheid wrijving mede bepalend is voor het al dan niet verstopt raken van de leiding. De gangbare wrijvingsmodellen voor mengsels, zoals ook toegepast in het eendimensionale model, bevatten een vloeistofterm en een vaste stof term. Die laatste wordt oneindig wanneer de concentratie vaste stof de dichtste pakking nadert, maar dit is niet realistisch.

In dit proefschrift is daarom op basis van grondmechanische beginselen een alternatief wrijvingsmodel afgeleid voor gelaagde sedimentproppen. Met een experiment is aangetoond dat de relatieve doorlatendheid van de diverse lagen en hun ordening ten opzichte van de stromingsrichting bepalend is voor de wrijving, en bovendien is de werkbaarheid van het model voor kwantitatieve voorspellingen aangetoond. Dit model is geïmplementeerd in het eendimensionale stromingsmodel.

Simulaties en experimenten tonen aan dat het vormen van een hooggeconcentreerde prop zeer goed mogelijk is, en dat een dergelijke prop tot verstopping kan leiden, maar de kans op de vorming van een dergelijke prop is erg klein. Zowel de begincondities van het transportproces als de korreleigenschappen moeten aan strikte eisen voldoen om propvorming en een verstopping mogelijk te maken, maar deze condities zijn niet heel waarschijnlijk wanneer het mengsel goed doormengd wordt aangeboden aan het transportsysteem.

CONTENTS

List of Symbols

Roman symbol	Description	unit
a	Empirical parameter, Eq. 2.21	[-]
A	Cross sectional area	$[m^2]$
Ar	Archimedes number	[-]
b	Empirical parameter, Eq. 2.21	[-]
Ba	Bagnold number	[-]
c_v	Volume fraction of solids	[-]
$c_{v,0}$	Initial volume fraction of solids	[-]
$c_{v,b}$	Volume fraction of solids at the perimeter of a pipeline	[-]
$c_{v,h}$	Volume fraction of solids in a shock	[-]
$c_{v,k}$	Volume fraction of solids of particle fraction k	[-]
$c_{v,l}$	Volume fraction of solids in front of a shock	[-]
$c_{v,max}$	Maximum volume fraction of solids	[-]
$c_{v,tr}$	Volume fraction of solids at regime transition	[-]
C_D	Drag coefficient	[-]
d_i	Particle diameter of fraction i, with $i = 10...100$	$[m]$
d_k	Particle diameter of fraction k	$[m]$
d_m	Mean particle diameter	$[m]$
d_s	Equivalent surface diameter	$[m]$
d_v	Equivalent volume diameter	$[m]$
D	Pipe diameter	$[m]$
e	Error in control loop Eq.6.10	$[m/s]$
E	Modulus of elasticity	$[Pa]$
f	Friction factor	[-]
f_l	Moody friction factor for laminar flow	[-]
f_t	Moody friction factor for turbulent flow	[-]
F	Solid's flux	$[m/s]$
F_B	Buoyancy force	$[N]$
F_F	Wall friction force	$[N]$
F_G	Gravity force	$[N]$
g	Gravitational acceleration	$[m/s^2]$
h	Bed height	$[m]$
h_0	Initial bed height	$[m]$
H	Water depth	$[m]$
i_t	Total hydraulic gradient	[-]
i_s	Hydraulic gradient of solid fractions	[-]

$i_{s,c}$	Hydraulic gradient due to wall friction of solids	[-]
i_f	Hydraulic gradient due to wall friction of fluid	[-]
i_m	Hydraulic gradient of the mixture	[-]
$i_{m,static}$	Hydraulic gradient of the static weight of the mixture	[-]
j	Time instance in numerical method: general simulation	[-]
J	Time instance in numerical method: pump dynamics	[-]
K	Number of fractions	[-]
k	fraction index	[-]
k_e	Coefficient in Eq. 2.4	[-]
k_f	Fluid conductivity	$[S/m]$
$k_{f,T}$	Fluid conductivity at temperature T	$[S/m]$
k_m	Mixture conductivity	$[S/m]$
k_r	Coefficient in Eq. 2.4	[-]
K_i	Bagnold grain inertia regime constant	[-]
K_D	Control variable: derivative gain	$[s^2/m]$
K_I	Control variable: integration gain	$[1/m]$
K_P	Control variable: proportional gain	$[s/m]$
L	Length (riser or plug)	$[m]$
L_0	Initial length	$[m]$
m	Mass	$[kg]$
m_a	Added mass	$[kg]$
m_s	Solids mass	$[kg]$
m_m	Measured mass	$[kg]$
m_i	Mass inserted in system	$[kg]$
M	Forcing term in Eq. 6.42	$[N/m^3]$
n	Richardson and Zaki Exponent	[-]
n_p	Drive speed	$[RPM]$
nof	Number of frames	[-]
p	Pressure	$[Pa]$
p_e	External pressure source (centrifugal pump)	$[Pa]$
$p_{e,f}$	External pressure source (centrifugal pump, fluid specification)	$[Pa]$
$p_{e,f,max}$	External pressure source (centrifugal pump, fluid specification, maximum value)	$[Pa]$
Pe	Peclet number	[-]
P_h	Hydraulic power	$[W]$
Q_m	Mixture volume flow	$[m^3/s]$
Q_s	Solids volume flow	$[m^3/s]$
Q_f	Carrier fluid volume flow	$[m^3/s]$
r	Radius	$[m]$
r_i	Ratio of gradients in flux limiter function	[-]
Re	Reynolds number	[-]

Re_p	Particle Reynolds number	[-]
$\overline{s}$	Average solids production	$[kg/s]$
s_{max}	Maximum solids production	$[kg/s]$
Stk	Stokes number	[-]
t	Time	$[s]$
t_e	Pump startup time	$[s]$
t_f	Fluid time scale	$[s]$
t_p	Particle time scale	$[s]$
t_{sim}	Simulated time span	$[s]$
T	Temperature	$[^oC]$
T_0	Reference temperature	$[^oC]$
v_d	Dynamic wave velocity	$[m/s]$
v_f	Fluid velocity	$[m/s]$
v_{front}	Shock front velocity	$[m/s]$
$v_{f,fl}$	Fluid velocity in a fluidization experiment	$[m/s]$
$v_{f,tr}$	Fluid velocity at regime transition	$[m/s]$
v_k	Kinematic wave velocity	$[m/s]$
$v_{k,s}$	Kinematic shock wave velocity	$[m/s]$
v_m	Mixture velocity	$[m/s]$
$\overline{v_m}$	Mixture bulk velocity	$[m/s]$
v_s	Solid fraction velocity	$[m/s]$
v_{set}	Solid fraction velocity	$[m/s]$
$\overline{v_s}$	Average solid fraction velocity	$[m/s]$
V	Volume	$[m^3]$
V_m	Mixture volume	$[m^3]$
V_s	Solids fraction volume	$[m^3]$
w	Settling velocity	$[m/s]$
w_k	Weight fraction of particle fraction k	$[-]$
w_t	Terminal settling velocity	$[m/s]$
$w_{t,a}$	Terminal settling velocity including the effect of wall friction	$[m/s]$
w_h	Hindered settling velocity	$[m/s]$
Y	Control parameter Eq.6.10	[-]

Greek symbol	**Description**	**unit**
α	Constant of proportionality	[-]
χ	Maximum packing limiter	[-]
δ	Axial dispersion parameter	[-]
δ_A	Axial dispersion parameter: deformation due to advection only	[-]
δ_D	Axial dispersion parameter: deformation due to dispersion only	[-]
ϵ_{pipe}	Pipe wall roughness	$[m]$

ϵ_z	Axial dispersion coefficient	$[m^2/s]$
ϵ_{Taylor}	Taylor dispersion coefficient	$[m^2/s]$
κ	Permeability	$[m^2]$
λ	Linear volume fraction of solids	[-]
μ_f	Dynamic viscosity of carrier fluid	$[Pa \cdot s]$
μ_k	Kinematic friction coefficient	[-]
ν_f	Kinematic fluid viscosity	$[m^2/s]$
ρ_f	Fluid density	$[kg/m^3]$
ρ_m	Mixture density	$[kg/m^3]$
$\overline{\rho_m}$	Average mixture density	$[kg/m^3]$
ρ_s	Solid particle density	$[kg/m^3]$
$\rho_{s,k}$	Solid particle density of fraction k	$[kg/m^3]$
σ	Stress	$[Pa]$
σ'	Effective stress	$[Pa]$
σ_r	Radial stress	$[Pa]$
σ_z	Axial stress	$[Pa]$
τ_f	Fluid shear stress	$[Pa]$
τ_m	Mixture shear stress	$[Pa]$
τ_s	Solids shear stress	$[Pa]$
τ_w	Wall shear stress	$[Pa]$
τ'_w	Effective wall shear stress	$[Pa]$
$\overline{\tau'_w}$	Average effective plug wall shear stress	$[Pa]$
ϕ	Sphericity	[-]
Φ	Internal friction angle	$[^o]$
Ψ	Flux limiter function	[-]
ξ	Exponent in Archie's equation	[-]
ζ	Exponent in CCM data fit equation	[-]

Abbreviation	**Description**
1DVHT	One Dimensional Vertical Hydraulic Transport (model)
CCM	Conductivity Concentration Meter
CCZ	Clarion Clipperton Zone
PSD	Particle Size Distribution
VTS	Vertical Transport System

1

INTRODUCTION

In the period 1872-1876, the H.M.S. Challenger set sail for a scientific cruise on the oceans to learn about the deep sea environment. The crew members were one of the first to discover manganese nodules, a deep sea deposit rich of metals. Since then deep sea deposits have been considered for mining, but only recently the first real steps into deep sea mining have been taken.

This chapter gives an introduction to deep sea mining and its technological challenges, one of them being the vertical transport of deep sea deposits from the sea floor to the sea surface. The combination of large transport distances with particles of many different sizes could lead to riser blockage. Flow assurance of the vertical transport process, or more specifically prediction of riser blockage, is the main topic of this thesis.

1.1. BACKGROUND

MAnkind's prosperity is depending on the availability of food, water, energy resources and raw materials. The consumption of natural resources is still increasing worldwide, with countries becoming more and more developed, but access to resources on land is not equally distributed.

Since the discoveries of the H.M.S. Challenger (Murray and Renard, 1876), deep sea deposits have been known to the public, but interest in deep sea mining as an alternative to terrestrial mining emerged only in the 1960's with J.L. Mero's book "The mineral resources of the sea" (Mero, 1965).

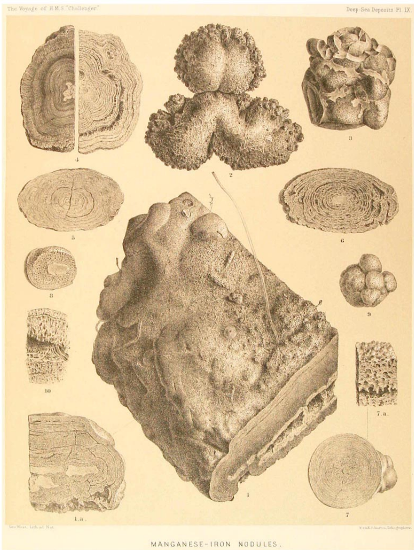

(a) Manganese nodules found by the H.M.S. Challenger crew.

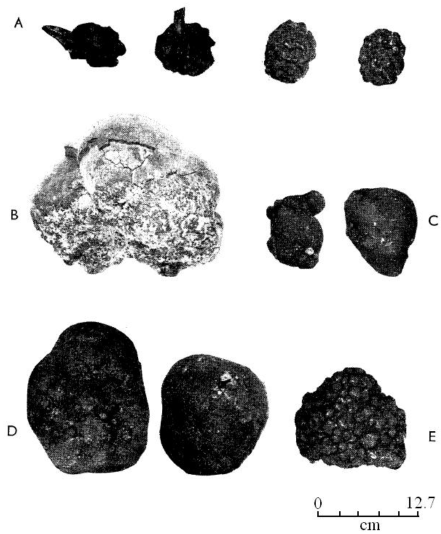

(b) Manganese nodules found in the South Pacific Ocean.

Figure 1.1: Drawing of the manganese nodules found by the H.M.S. Challenger crew, Murray and Renard (1876) and manganese nodules found at the bottom of the South Pacific Ocean at depths of 1270 m (A) to 5000 m (C). Picture reproduced from Mero (1965).

Deep sea deposits of interest are amongst others marine diamonds and phosphate nodules at depths of several hundreds of meters, sea floor massive sulfide deposits at depths up to two kilometers and polymetallic (manganese) nodules at depths up to six thousand meters.

Due to the high deposit value, marine diamond mining is already common practice, but mining other deposits is only in a very early stage. The Chatham Rise phosphate nodule deposit in New-Zealand was indicated as an option for producing artificial fertilizers (Falconer, 1989). In 2011 interest in this deposit revived, but in 2015 New Zealand's Environmental Protection Authority prohibited mining by refusing the consent application.

In the 1980's hydrothermal vents were discovered at the bottom of the ocean (Rona, 2008). Ocean water seeps through porous rock and reacts with the rock to form minerals and acid water. Induced by high temperature bedrock in the vicinity of tectonic ridges, metals (predominantly Fe, Cu, Zn, Au and Sn) are leached into the acid fluid. When heated up to about 400 ^{o}C, the hydrothermal fluid rises and exits the sea floor through a vent. When the hot fluid meets the cold sea water, minerals precipitate forming chimney-like structures. Sulfuric minerals in the fluid colors the venting plumes black, hence their name black smokers (Drew, 2009). In general black smokers and their surrounding sulfuric deposits are called Sea floor Massive Sulfide deposits. In 2005 Nautilus Minerals Inc. started exploring the SMS deposits in the Exclusive Economic Zone of Papua New Guinea. In 2010 several drilling trials in the Solwara 1 project in Papua New Guinea showed the presence of high graded copper deposits, and mining is expected to start within a few years from 2015. SMS deposits need to be cut and excavated before small, transportable pieces are obtained. Due to the excavation process, rock cuttings from hydrothermal vents are expected to have very unspherical, angular shapes. Crushing during excavation will cause many fines and large pieces can be expected as well. The particle size distribution emerging from this deposit will be wide.

Nodule mining at depths of several kilometers has only been accomplished during several test trials, but no commercial activities towards nodule mining are planned yet. Manganese nodules occur in a wide variety of sizes and shapes. They are found at various depths. Normally nodule sizes range from 5 – 250 mm. They have a rate of formation of approximately 0.1 mm per 1000 years, so nodule formation is a long term process on human scale. Many nodules form around small nuclei, and the nodule shape tends to follow the shape of the nucleus. Often spherical shapes are encountered, but due to agglomeration of nodules in different stages of formation basically any shape (from almost perfectly spherical to angular and elongated shapes) can be obtained. Figure 1.1 shows examples of manganese nodules.

Nodules can be found lying scattered on the seabed, mostly under a small layer of fines. These nodules could be picked up relatively easily, without the need for cutting or excavation.

It is clear that the combination of the open ocean, the large depths and the relatively unknown environment at the sea floor poses many challenges to deep sea mining activities. The general approach to deep sea mining is cutting or collecting the deposits from the sea floor and transporting the solids to a support vessel, followed by shipping and processing. There are several options for the vertical transport operation, ranging from grabs to continuous hydraulic transport through a riser using booster stations. An example of a mining support vessel with a vertical transport system and a subsea mining tool is given in Figure 1.2.

When aiming for continuous and stable production at a high level, vertical hydraulic transport of solid-water mixtures with a riser with booster stations prevails. This system is the subject of study in this thesis.

1.2. EARLIER WORK AND STATE OF THE ART

HYdraulic transport of sand-water mixtures is common practice in dredging. Vertical transport distances however often are modest, just in the order of tens of meters.

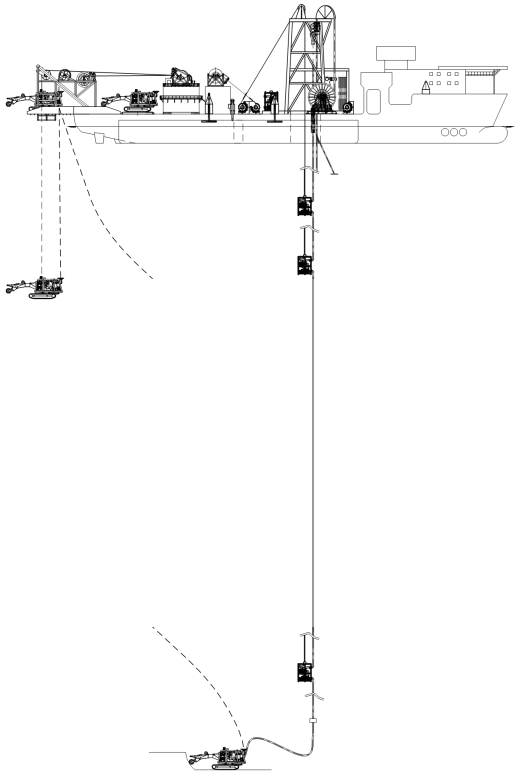

Figure 1.2: Schematic picture of a deep sea mining system, comprising a mining support vessel, a vertical transport system with riser and booster stations and a subsea mining tool.

Even modern dredgers do not exceed 150 m dredging depth.

"The time is now and the tools are at hand." (Flipse, 1969). In the period of late 1960's to early 1980's much research to deep sea mining has been conducted by companies and institutions all over the world. Several consortia were active in the premature deep sea mining industry, committed to technology development and pilot scale testing: The Ocean Mining Associates (OMA) contracted Deepsea Ventures, who successfully tested nodule mining on the Blake Plateau near Florida (at a depth of about 750 m) using an airlift system. Successful metalliferous sediment mining tests in the Red Sea at a depth of 2200 m were conducted by the German company Preussag AG and the Red Sea Commission (Zaki and Amann, 1980). Ocean Management Inc. (OMI) conducted nodule mining tests using hydraulic transport with submerged pumps and airlift systems (Bath, 1989). The Kennecott Group developed a draghead and hydraulic transport system that were to be operated from a ship. The Ocean Minerals Company (OMCO, including the Dutch companies Shell and Boskalis) developed mining and processing technology, led by Lockheed Martin, and conducted mining equipment tests at a depth of 5000 m (Welling, 1981). The governments of France, China, India, Japan, Korea and Russia also initiated deep sea mining initiatives. Some of the programs are still running, for instance the China Ocean Mineral Resources Research and Development Association (COMRA) looks amongst others into pump technology development and simulation of the mining process (Liu et al., 2003; Li et al., 2005; Zou, 2007).

IHC had futuristic ideas about deep sea mining equipment, as shown by the artist impression in Figure 1.3. Mero (1965) discusses some concepts for deep sea mining, ranging from bucket ladder dredges to long distance air lift systems. More concepts are presented in Pearson (1975), amongst which is a transport system with floating containers. He even makes note of a continuous bucket line system (a long cable with buckets mounted to it) that is said to have successfully retrieved manganese nodules from the sea floor at a depth of 3650 m.

Interest in deep sea mining declined in the 1980's due to project failures (large investments, immature technology) and sufficient supply of resources from terrestrial mines. In an elaborate overview of deep sea mining technology development, Chung (2009) remarks that despite of the large amount of research and development activities in the 1970's, deep sea mining technology is still in a very early learning stage.

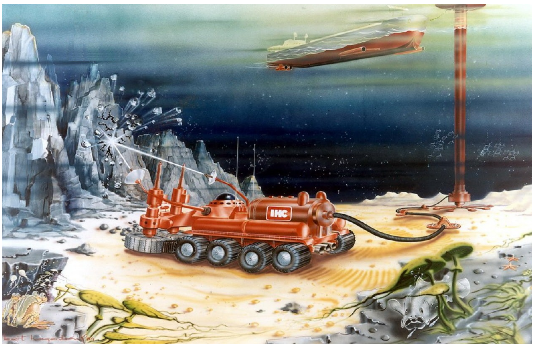

Figure 1.3: Artist impression of a deep sea mining crawler from 1982 as presented by IHC.

Much laboratory work on vertical hydraulic transport has been concerned mainly with the basic system parameters such as flow, pressure loss and production. Few researchers have looked into flow assurance. The following overview of work explicitly related to deep sea mining is not an exhaustive summary of all work in the field, but it governs the main topics of research of the past decades.

Newitt et al. (1961); Condolios et al. (1963); Brebner and Wilson (1964) and Cloete et al. (1967) aimed at system optimization by studying stationary vertical transport situations, with a focus on transport velocities, hydraulic losses and production capacity.

Nederveen (1968) (Former IHC Holland Marine Mining Division) reports on a calculation method to determine the frictional losses and required pump capacity of a vertical transport system. The mixture is treated as a continuum, and the solids velocity is found by superposition of the fluid velocity and the solids settling velocity.

Clauss (1971) investigated the vertical hydraulic transport of manganese nodules at volume fractions of solids of about $c_v \approx 0.16$. The slip velocity of particles with respect to the fluid is calculated using the terminal settling velocity of a particle, corrected for the influence of the riser walls. Combined with expressions for frictional losses between the fluid and riser, Clauss (1971) aims at optimization of the system's energy consumption per ton of ore. In his paper an experimental setup is depicted consisting of a hydraulic circuit with a 9 m transparent riser with $D = 100\,mm$. In the experiments the delivered volume fraction of solids (by determining the output solids weight in time), frictional losses, particle velocities and radial solids distributions are measured. Velocities and solids distributions are measured by means of photography.

Engelmann (1978) performed tests with ceramic spheres with diameters of 13−52 mm in a vertical test setup. This facility consisted of a riser of 30 m length and it had a diameter of 200 mm. Solids were injected at the bottom of the riser and were lifted by a continuous flow of water. The experiments aimed at determining mass flow rates and pressure drops.

Sellgren (1982) conducted tests with coarse granular material in water. Based on the observation that the drag coefficient of particles might suddenly drop in turbulent flow, and the required fluid velocity thus increases, he suggests that the fluid velocity should be in the order of 4 – 5 times the settling velocity of the largest particle to assure safe operation.

Shook (1988) studied the development of a riser blockage in time, starting at the point of blockage, for plugs consisting of differently sized particles. To ensure that the vertical pipe will not get blocked, he advised to transport small particles with a narrow particle size distribution using large fluid velocities.

Evans and Shook (1991) report on numerical simulation of hydraulic hoisting of solid particles by solving the advection–diffusion equation for a single batch of solids. The advection velocity of solid particles is modeled using a method quite similar to hindered settling theory. Where Shook only used advection, Evans and Shook also use dispersion of the solid fraction, modeled by Taylor dispersion. They conducted experiments in a single riser having $L = 10.76\,m$ and $D = 26.3\,mm$. For fine particles ($d = 0.175\,mm$) in a narrowly graded batch the modeling approach worked well, but for more coarse material ($d = 4.1\,mm$) Taylor dispersion proved less successful. In contrary to Sellgren, they found minimum transport velocities in the order of 2 – 3 times the terminal settling velocity of the largest particle.

Xia et al. (2004a) studied the vertical transport of manganese nodules. They made nodules out of concrete scale 1 : 1, with diameters in the range $d = 30 - 50\ mm$. They gathered data on transport velocities and wall friction in a test setup of about 10 m high. In a transparent section particle behaviour could be monitored. Their main results are an empirical equation for calculating the pressure loss for large particles in upward flow, an empirical equation (data fit) for the transport velocity of nodules and an empirical equation for calculating the effect of the volume fraction of solids on the nodule's transport velocity. In Xia et al. (2004b) this research is extended by including the effect of swaying risers on wall friction.

At IHC MTI Choi (2008) conducted experiments in which the vertical hydraulic transport of glass beads in a $D = 100\,mm$ riser was studied. He made video recordings of the transport process, in which it could be clearly seen that under some conditions, density waves or plugs are transported through the riser.

Yang et al. (2011) used a setup of 30 m high, comparable to the setup presented in Engelmann. They report on the existence of different flow regimes, similar to those found by Choi (2008), but no further information on their nature is provided.

Van den Berg and Cooke (2004) compare hydraulic hoisting systems for use in the terrestrial platinum mining industry, with vertical transport distances of 270 m to 2200 m. They report on the use of a fluidization feeder, which induces particle stratification at the inlet of the riser. Coarse particles will enter the riser first, followed by fines. They mention the risk of riser blockage as a result of the increasing volume fraction of solids as the fines overtake the coarse particles.

Van Dijke (2010) made a one dimensional steady state model of the transport of differently sized solid particles in a vertical riser, which showed that concentration peaks could develop during transport. This mechanism has been identified by Talmon and Van Rhee (2011) as a potential risk to hydraulic transport operations for deep sea mining. When a batch of material is transported with velocity $v_{s,1}$, directly followed by a batch of material with velocity $v_{s,2} > v_{s,1}$, the second batch will run into the first. Upon merging, the volume fraction of solids in the mixing zone increases, resulting in a larger transport velocity in the mixing zone (which follows from the dependency of the transport velocity on the volume fraction of solids c_v). In this way the volume fraction of solids can reach the maximum packing. This mechanism is depicted in Figure 1.4.

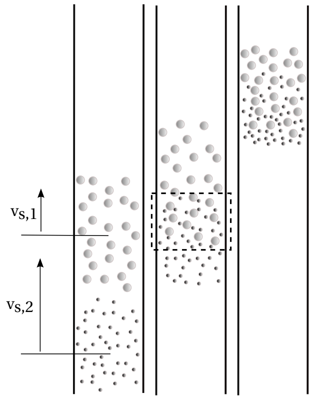

Figure 1.4: The merging of two batches with velocities $v_{s,2} > v_{s,1}$. In the merging zone (dashed rectangle) the transport velocity increases, thus creating a densely packed plug.

Plugs developing this way typically have a layered structure, with coarser (or more dense) material on top of finer (or less dense) material.

The above overview shows that the performance of vertical hydraulic transport systems has been investigated thoroughly in the past, but the focus has mainly been on systems working at desirable operating conditions. There is only little known about off-design operations and flow assurance in vertical transport systems, i.e. the occurrence of plugs, density waves and possible riser blockage, while flow assurance is a key element in any deep sea mining operation.

1

1.3. PROBLEM DEFINITION

THe general design and operation of vertical hydraulic transport systems has got much attention in the past, which enables us to determine pressure requirements, flow velocities and the production capacity of a system. Only few researchers point at potential problems related to flow assurance.

One aspect of flow assurance is flow stability, which relates to the occurrence of different flow regimes. Especially the occurrence of plugs or density waves is of interest, because they are detrimental for the transport system. An absolute show stopper would be blockage of the riser. Flow assurance needs to be an integral part of the design of vertical transport systems, but the current state of knowledge on vertical hydraulic transport is not sufficient to do so.

Since typical vertical transport systems will be extremely large and expensive, research to their operation has to be done by scale model testing and numerical modeling. With respect to flow assurance, we are interested in the entire riser rather than subsections of the system, but processes on particle level will be of importance to the macroscopic system behaviour. Given the large computational domain, the use of models with discrete particles will be computationally too expensive, so we are aiming at a continuum model. A significant amount of relatively large particles ($d/D = O(10^{-1})$) will be present in the transport system, so the applicability of continuum theory should be studied in more detail. Especially the verification of hindered settling theory for large particles, modeling the axial dispersion of large particles and the description of wall friction of plugs all require (experimental) investigation. Furthermore, the hypothesis of blockage due to merging of batches has to be validated. For building a model of the entire vertical transport system, we thus need to study individual processes first.

The experiments envisaged in this project all comprise the transport of suspended particles in an upward flow of water, from which isolated phenomena will be studied. This asks for dedicated experiments for each subject. Experimental research introduces scale effects and model effects. Scale effects come from force ratio's that do not scale properly between model and prototype, while model effects come from differences between the actual model and prototype (Heller, 2011). Both effects are present in the experiments in this thesis.

While in real deep sea mining applications one would expect some variation in particle densities and shapes, only a small subset of densities and shapes could be covered in this thesis. Furthermore deep sea fluid properties (density and viscosity) are different from the properties of the tap water used in our research. These make up the model effects.

Scale effects are mainly present in the choice of the riser dimensions. Real vertical transport systems will have diameters roughly in the range $200-800\,mm$ and they will employ transport velocities of about $3-6\,m/s$. Our experiments however are conducted in risers with a diameter of $D \approx 100\,mm$ and $D \approx 150\,mm$ with velocities of $v_m \approx 2\,m/s$. This introduces a scale effect which can be clearly seen in the Reynolds numbers of the model and prototype. In both cases water is the carrier liquid, so the ratio of Reynolds numbers is $Re_{model}/Re_{prototype} \approx (v_{m,model} \cdot D_{model})/(v_{m,prototype} \cdot D_{prototype})$. When the model properties are $v_{m,model} = 2\,m/s$ and $D_{model} = 0.1\,m$, and the prototype properties are $v_{m,prototype} = 5\,m/s$ and $D_{prototype} = 0.5\,m$, then the ratio of Reynolds numbers is $Re_{model}/Re_{prototype} = 0.08$. This means the model underestimates the prototype Reynolds numbers with more than a factor ten. With a model Reynolds number of $Re_{model} \approx 2 \cdot 10^5$, both the model flow and the prototype flow are highly turbulent and the scale effect has not much influence on the experiment.

1.4. RESEARCH QUESTIONS AND OBJECTIVE

THE main question in this research project is: *Can a vertical transport system get blocked?*

The subquestions to be answered are:

- *Which flow regimes can be expected during transport?*
- *How does a blockage develop?*
- *What is the wall friction between a plug and the riser wall?*
- *How to model transient mixture flow in vertical transport systems?*

The objectives of this research project are to validate the blockage hypothesis (merging of batches) and to develop a model that describes the vertical hydraulic transport of solids, both in space and time, in a riser with booster stations.

1.5. OUTLINE OF THIS THESIS

THE two main components of this thesis are the development of a one dimensional flow model and laboratory experiments in support of the model. Both parts are strongly related. Theory from one part will be used to interpret experimental data, and data will be used to support the development of new theory.

The one dimensional flow model needs closure relations for the solids transport velocity, the axial dispersion of solids and wall friction of solids. These topics are covered in Chapters 2, 3 and 5.

Chapter 2 describes the results of a fluidization experiment and transport experiment. With these experiments we show that the hindered settling theory of Richardson and Zaki (1954) can be used to calculate the slip velocities of particles in the 1DVHT model beyond the d/D range in the original work of Richardson and Zaki. Then we explore the stability of vertical transport systems by using the analogy with a fluidized bed and theory developed for stability analysis of fluidized beds.

Chapter 3 describes the results of a hydraulic transport experiment in which batches of sediment and granulate are transported through a vertical pipe. By monitoring the volume fraction of solids along the course of a batch, the deformation of the batch can be studied, which gives information about the axial dispersion process. We relate the axial dispersion to particle inertia, which is used in the 1DVHT model.

Models for wall friction of vertical slurry flows are well established, but no friction model existed for the case when the volume fraction of solids reaches the maximum packing and the particles start behaving like a solid plug. Chapter 5 introduces a friction model for layered sediment plugs, which is verified with an experiment.

Besides the experiments for the closure relations of the 1DVHT model, we also needed to find experimental proof of the blockage hypothesis posed in this chapter. For this purpose a dedicated experiment was designed, in which the plug formation by merging of two batches of particles is studied. The experiment is discussed in Chapter 4.

The complete 1DVHT model is presented in Chapter 6. The model is used for a case study of mining manganese nodules, which is presented in Chapter 7.

Each chapter contains conclusions and recommendations regarding the specific topic of that chapter. The overall conclusions and recommendations are given in Chapter 8.

2

EXPERIMENTAL STUDY OF THE SOLIDS TRANSPORT VELOCITY AND THE STABILITY OF THE VERTICAL TRANSPORT PROCESS

Vertical hydraulic transport systems for deep ocean mining have lengths up to a few kilometers from sea floor to sea surface. Typical ratios of particle diameter d over riser diameter D are $d/D = O(10^{-1})$, and the feeding of the riser is irregular. These conditions make the vertical transport operation susceptible to propagating density waves which is detrimental for the transport process. There is however few experience with hydraulic transport on this scale.

In this chapter a continuum description of the transport process and stability analysis theory from the field of fluidization technology are used. By Indicating the similarities and differences between fluidization and vertical hydraulic transport, it is shown that the theory can be extended to transport conditions as well.

The applicability of the theory is demonstrated with a fluidization experiment using particles having $d/D \leq 0.26$, which is an extension of the d/D range in classic hindered settling theory. The transport experiment with similar particles shows differences with the fluidization experiments, indicating that flow stability in vertical transport might actually improve compared to fluidization.

The last topic of this chapter is the fluidization of irregularly shaped particles.

Sections 2.1 to 2.3 of this chapter have been submitted to Ocean Engineering.

2.1. INTRODUCTION

IN deep ocean mining, the vertical hydraulic transport of polymetallic nodules or large rock cuttings is a key process. With $d/D = O(10^{-1})$ (particle diameter d, riser diameter D), relative particle sizes found in this industry exceed the conventional hydraulic transport parameter range by far. Different transport modes or regimes are very likely to occur, so knowledge of these regimes is essential for design and operation of vertical transport systems. Since there is a strong analogy between vertical hydraulic transport and fluidization technology, we will use the latter as a starting point for this research.

In fluidization theory, two extreme regimes are discerned. There is the state of homogeneous fluidization on one side, where all particles in the fluidized bed are homogeneously distributed, and there is the plug flow regime on the other side of the spectrum. In the plug flow regime, particles move through the fluidization column as density waves, collecting particles on top of the plug and loosing particles at the bottom. The plug flow is associated with system instability, i.e. the density waves might actually grow and form large solid plugs. It is expected that similar regimes can also occur in vertical transport systems. The occurrence of the plug flow regime in a vertical transport system will be detrimental for the operation, so this regime should be avoided.

In his review article, Di Felice (1995) reports on 26 liquid-solid fluidization experiments from the period 1948-1991 in 10 of which void waves or plugs have been observed. In a fluidized bed plugs thus are a quite common feature. Studies in the field of fluidization technology that focus on stability criteria for fluidized beds are for instance Verloop and Heertjes (1970), Foscolo and Gibilaro (1984), Foscolo and Gibilaro (1987), Batchelor (1988) and Nicolas et al. (1994). Only few researchers however have addressed the problem of plug flow occurring in transport systems.

The vertical transport of large particles (manganese nodules) has been studied by amongst others Clauss (1971), Engelmann (1978), Xia et al. (2004a) and Yang et al. (2011), but only the latter shows a photograph of different flow regimes. Research at IHC MTI in 2008, in which monodisperse mixtures of glass beads were transported in a vertical water flow, showed the occurrence of plugs that propagated through the riser ($D = 100\,mm$) as waves with a very large volume fraction. The density waves seemed to be dependent on particle properties. Especially the larger particles ($d > 20\,mm$) showed propagating plugs. These experiments motivated us to conduct more experiments, which are reported in this chapter.

Yang et al. (2011) conducted hydraulic lifting experiments in a setup of 30 m high and 200 mm in diameter. They provide pictures showing plugs similar to those observed in the IHC MTI laboratory in 2008, but no information is given on the demarcation of the different regimes. It is however clear from these experiments that particles with $d/D = O(10^{-1})$ typically show the plug flow behaviour.

Propagating plugs have been studied more thoroughly in the field of vertical pneumatic conveying. Niederreiter and Sommer (2004) developed a sensor for measuring the forces on pneumatically conveyed plugs of solids. Their experimental facility has a transparent vertical pipe with $D = 50\,mm$, in which plastic beads with $d = 3\,mm$ are transported. Camera stills given in their paper display the propagation of a plug very similar to those observed in our experiments in 2008 and those shown in Yang et al. (2011). In Strauss et al. (2006) experiments with the setup of Niederreiter and Sommer

(2004) are compared with DEM simulations. These simulations again show plugs being propagated through the riser, but no analysis is made of possible flow regime transitions.

An extensive analysis of flow regimes and regime transitions for vertical pneumatic conveying systems and fluidized beds (gas-solid, liquid-solid) is given by Rabinovich and Kalman (2011). They differentiate between dense phase flow and dilute phase flow. Within the dense phase flow, one can find the separate plugs and plugs with particle rain, and in the dilute phase flow one finds transport of homogeneous mixtures. The plugs with particle rain or density waves are in fact the plugs that are studied by Niederreiter and Sommer (2004) and Strauss et al. (2006). For our research the regime transition from plug flow to the state of homogeneous flow is important.

The occurrence of propagating plugs would be a serious risk for the hydraulic transport operation as they can result in riser blockage. This problem has not got much attention so far, while instabilities in fluidized beds have been investigated thoroughly. Therefor we start our analysis of the problem by a review of literature on fluidization, and from there we take the step to the occurrence of plug flow in vertical hydraulic transport. When the conditions at which plugs occur are known, the design of vertical hydraulic transport systems can be optimized for flow stability. To this end, first a continuum model is presented to find a theoretical description of the propagation of disturbances through a riser. Then fluidization experiments and transport experiments are presented in which the propagation velocities of disturbances are measured and compared with theory. Based on these results we discuss the stability of the internal flow in vertical transport systems.

2.2. THEORY

2.2.1. STABILITY OF FLUIDIZED BEDS

Di Felice (1995) reports on many instable liquid-solid fluidized beds, in which density waves, plugs, voidage waves etc. were observed. The propagation of disturbances has been studied extensively in the literature in an attempt to explain the turbulent nature of many fluidized beds, and the sometimes sudden transition from highly instable to almost perfect homogeneous fluidization.

Much of the work on stability of fluidized beds can be traced back to Wallis (1969). The essence of his stability theory of fluidized beds is the existence of two types of propagating disturbances: kinematic waves (with velocity v_k) and dynamic waves (with velocity v_d). Kinematic waves are propagating disturbances in a homogeneous fluidized bed (i.e. the propagation of a local increase in the volume fraction of solids c_v). Dynamic waves are related to the propagation of a force field.

The kinematic wave velocity can be found from the solids flux $F(c_v) = c_v \cdot v_s$. The solids flux F is a nonlinear function in c_v. It will be discussed in detail in Section 2.2.2. From the solids flux $F(c_v)$ the kinematic wave velocity for small perturbations can be found (Leveque, 1990):

$$v_k(c_v) = \frac{\partial F(c_v)}{\partial c_v} \tag{2.1}$$

For dynamic waves to exist, the particle bed should behave like an elastic medium with modulus of elasticity E. The concept of elasticity of a fluidized bed was used by

Verloop and Heertjes (1970) to predict the transition from homogeneous to heterogeneous fluidization. They employed the stability criterion of Wallis (1969), which states that a fluidized bed is stable when $v_d > v_k$ and unstable when $v_d < v_k$. The main challenge in the work of Verloop and Heertjes (1970) was to find a suitable expression for the modulus of elasticity of the bed. They propose an expression for E as a function of the minimum fluidization velocity. According to their calculations, E should be in the order $10^2 - 10^4\ Pa$.

In pursuit of a similar criterion for fluidized bed stability, Foscolo and Gibilaro (1984) introduce the drag force on a particle in the fluidized bed as a function of the volume fraction of solids in the bed and particle properties. In this way, they derive the particle phase pressure gradient $\partial p/\partial z = E \cdot \partial c_v/\partial z$, so that the dynamic wave velocity could be computed as $v_d = \sqrt{\partial p/\partial \rho_s} = \sqrt{E/\rho_s}$. The particle phase pressure is due to the hydrodynamic interaction between particles and fluid, not to be confused with grain stresses. An extensive research program on the dynamics of fluidized beds by research groups in Italy and the UK in the period 1984-2001 is reported in Gibilaro (2001).

Foscolo and Gibilaro (1984) give for E:

$$E = 3.2 \cdot g \cdot d \cdot c_v \cdot \left(\rho_s - \rho_f\right) \tag{2.2}$$

so that the dynamic velocity is given by:

$$v_d = \sqrt{3.2 \cdot g \cdot d \cdot c_v \cdot \left(\rho_s - \rho_f\right) / \rho_s} \tag{2.3}$$

When the solids density and fluid density are of the same order of magnitude (which could be the case for practically all relevant vertical hydraulic transport processes), the added mass of particles should be taken into account. In Gibilaro et al. (1990) the work of Foscolo and Gibilaro (1984) is extended to yield the following description of the dynamic wave velocity v_d:

$$v_d = \frac{k_r \cdot v_{f,fl} + \sqrt{k_e \cdot (1 + k_r) - k_r \cdot v_{f,fl}^2}}{1 + k_r} \tag{2.4}$$

The coefficient k_e is defined as $k_e = (2 \cdot E) / \left(2 \cdot \rho_s + \rho_f\right)$, with E given by Equation 2.2, the coefficient k_r is defined as $k_r = \left(3 \cdot c_v \cdot \rho_f\right) / \left[(1 - c_v) \cdot \left(2 \cdot \rho_s + \rho_f\right)\right]$. The superficial velocity at fluidization is denoted $v_{f,fl}$. An important initial observation is that inclusion of added mass as in Equation 2.4 results in a smaller v_d, which is detrimental for the stability of a fluidized bed.

Several authors have conducted stability analyses of fluidized beds using the concept of dynamic waves relating to the particle phase pressure, see for instance Foscolo and Gibilaro (1987), Batchelor (1988), Nicolas et al. (1994) and Johri and Glasser (2002). Key concept is the actual modelling of the particle phase pressure because it defines the modulus of elasticity E of the mixture.

The theory can be summarized as follows. Irrespective of the source of a disturbance, the disturbance will propagate through the mixture at a finite velocity, which will be visible as travelling regions of large volume fractions of solids. Whether the amplitude of the disturbance grows or diminishes depends on the properties of the mixture. When

$v_d > v_k$ the amplitudes diminish and there is stable flow, while for $v_k > v_d$ amplitudes grow. For assessment of the stability, simply comparing v_d and v_k is sufficient. If we want to know whether a system is extremely instable or just slightly instable, a more detailed analysis can be conducted as outlined in Gibilaro (2001).

2.2.2. A CONTINUUM DESCRIPTION OF PARTICLE TRANSPORT

For the development of density waves we are interested in the axial development of the volume fraction of solids, hence the continuity equation can be simplified to the z direction only, with z positive upwards (anti-gravity). According to our previous research reported in Van Wijk et al. (2014a), for inert (in this case relatively large) particles the effect of axial dispersion is negligible. This results in the transport equation for the volume fraction of solids c_v:

$$\frac{\partial c_v}{\partial t} + \frac{\partial (c_v \cdot v_s)}{\partial z} = 0 \tag{2.5}$$

The solids transport velocity v_s is given by:

$$v_s = v_f - v_{slip} \tag{2.6}$$

In Equation 2.6, v_f is the superficial fluid velocity (i.e. the fluid velocity in an empty pipe $4 \cdot Q_f/(\pi \cdot D^2)$) and v_{slip} is the solids velocity with respect to the fluid. The slip velocity of solids in an upward flow of water is modelled by Richardson and Zaki (1954):

$$v_{slip} = 10^{-d/D} \cdot w_t \cdot (1 - c_v)^n \tag{2.7}$$

The factor $10^{-d/D}$ shown in Equation 2.7 proves to be very significant for relatively large solids. Note that in a sedimentation or fluidization experiment it holds $v_f = v_{slip}$, while the actual particle slip velocity with respect to the fluid surrounding the particle is $v_{slip} \cdot (1 - c_v)^{-1}$. The exponent n depends on the particle Reynolds number:

$$Re_p = \frac{\rho_f \cdot w_t \cdot d}{\mu_f} \tag{2.8}$$

The value of n ranges from $n = 2.36$ for relatively large particles to $n = 4.7$ for relatively small particles. The exponent n is modelled according to Rowe (1987):

$$n = \frac{4.7 + 0.41 \cdot Re_p^{0.75}}{1 + 0.175 \cdot Re_p^{0.75}} \tag{2.9}$$

In Equation 2.7, w_t is the terminal settling velocity of a single (spherical) particle. It is given by:

$$w_t = \sqrt{\frac{4 \cdot g \cdot (\rho_s - \rho_f) \cdot d}{3 \cdot \rho_f \cdot C_D}} \tag{2.10}$$

Typical solid's densities of deep sea deposits are in the range $2000\,kg/m^3 < \rho_s < 3000\,kg/m^3$. The drag coefficient C_D is a function of Re_p as well. Cheng (2009) provides a comparison of eight relations for $C_D(Re_p)$ of spherical particles. Based on his review, the equation of Brown and Lawler (2003) is used:

$$C_D = \frac{24}{Re_p} \cdot \left(1 + 0.15 \cdot Re_p^{0.681}\right) + \frac{0.407}{1 + 8710 \cdot Re_p^{-1}} \tag{2.11}$$

Having defined the terms in Equation 2.6, it can be rewritten to:

$$v_s = v_f - 10^{-d/D} \cdot w_t \cdot (1 - c_v)^n \tag{2.12}$$

Now the solids flux $F(c_v) = c_v \cdot v_s$ can be defined:

$$F(c_v) = c_v \cdot v_s = v_f \cdot c_v - 10^{-d/D} \cdot w_t \cdot c_v \cdot (1 - c_v)^n \tag{2.13}$$

And the kinematic wave velocity follows from Equation 2.1:

$$v_k(c_v) = \frac{\partial F(c_v)}{\partial c_v} = v_f - 10^{-d/D} \cdot w_t \cdot (1 - c_v)^n + 10^{-d/D} \cdot w_t \cdot c_v \cdot n \cdot (1 - c_v)^{n-1} \tag{2.14}$$

Foscolo and Gibilaro (1984), Batchelor (1988) and many others (Di Felice, 1995) use $v_k = n \cdot w_t \cdot c_v \cdot (1 - c_v)^{n-1}$ (omitting the factor $10^{-d/D}$). Indeed, in the case of fluidization it holds (by definition) $v_f = v_{slip}$, so then the first two terms in Equation 2.14 cancel.

For $n < 3$ (which is the case for all glass beads used in our experiments), Equation 2.14 is a monotonically increasing function of c_v up to $c_v = c_{v,max}$. It can be seen that a constant fluid velocity v_f only implies a shift in kinematic wave velocity, or in other words, the kinematic wave velocity manifests itself relative to the fluid velocity. This would be true in the absence of a significant influence of the riser wall on the solids transport velocity. In that case the propagation of discontinuities during fluidization and vertical hydraulic transport are equally comparable.

When perturbations are larger, the velocity of the front of the perturbation is given by the shock velocity $v_{k,s}$. If the volume fraction of the perturbation is denoted $c_{v,h}$ and if the volume fraction of the mixture (which the shock runs into) is denoted $c_{v,l}$, with $c_{v,h} > c_{v,l}$, then the shock velocity is given by:

$$v_{k,s} = \frac{F(c_{v,h}) - F(c_{v,l})}{c_{v,h} - c_{v,l}} \tag{2.15}$$

The envelope of the propagation of disturbances has an upper limit of v_k (Equation 2.14), a lower limit of v_s (Equation 2.12), and all possible $v_{k,s}$ are in between (Equation 2.15).

2.2.3. FROM FLUIDIZATION TO VERTICAL HYDRAULIC TRANSPORT

In order to use the stability criterion for fluidized beds $v_d = v_k$, we have to verify that the moving frame of reference (transport versus fluidization) has no significant influence. The interaction between the mixture and the riser during transport is evidently wall friction, which is absent in the case of fluidization.

The wall shear stress of the mixture is modelled as $\tau_m = \tau_f + \tau_s$ (Ferre and Shook, 1998). The fluid wall shear stress is given by:

$$\tau_f = \frac{f}{8} \cdot \rho_f \cdot v_f^2 \tag{2.16}$$

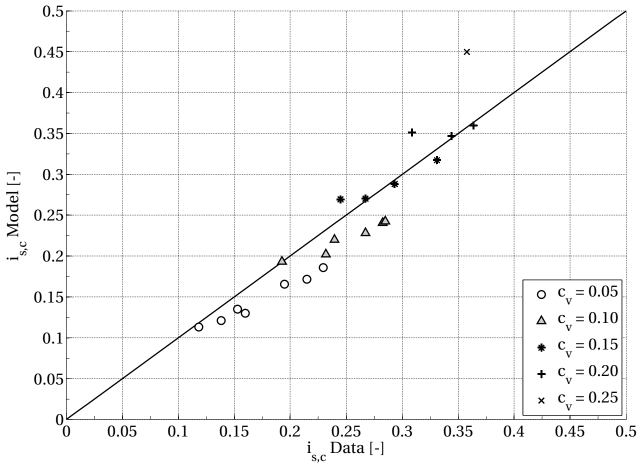

Figure 2.1: The solid's contribution to the hydraulic gradient compared with the data of Xia et al. (2004a). The model gives a good estimate of the order of magnitude of frictional losses.

Here, f is the Darcy-Weisbach friction factor which can be found with for instance the Moody diagram. The solids shear stress τ_s can be modelled with Ferre and Shook (1998):

$$\tau_s = 0.0214 \cdot \left(\frac{\rho_s \cdot \overline{v_m} \cdot d}{\mu_f}\right)^{-0.36} \cdot \left(\frac{d}{D}\right)^{0.99} \cdot \lambda^{1.31} \cdot \rho_s \cdot \overline{v_m}^2 \tag{2.17}$$

Note that Equation 2.17 uses the mixture bulk velocity $\overline{v_m}$, which is given by $\overline{v_m} = c_v \cdot v_s + (1-c_v) \cdot v_f$. The linear volume fraction of solids is given by $\lambda = \left((c_{v,max}/c_v)^{1/3} - 1\right)^{-1}$. Measurement in $D = 99.4\,mm$ and $D = 136.4\,mm$ pipe sections with glass beads in the range $d = 10 - 35\,mm$ have shown that the maximum volume fraction of solids takes the value $c_{v,max} \approx 0.6$.

Xia et al. (2004a) report frictional losses of surrogate manganese nodules in an upward water flow. The nodules have $d = 15\ mm$, $\rho_s = 2000\,kg/m^3$ and the riser has a diameter $D = 200\,mm$, a scale comparable to prototype scale. The data comprise the total hydraulic gradient $i_t = \frac{dp}{dz} \cdot \frac{1}{\rho_f \cdot g} = i_f + i_s + i_{s,c}$: the total gradient is given by the carrier fluid flow gradient i_f, the static contribution of the solids i_s and the solid's contribution due to collisions (friction) $i_{s,c}$. Figure 2.1 shows the measured solids gradient $i_{s,c}$ compared to the gradient computed with Equation 2.17. The transported volume fractions of solids as given in the paper ($c_v = 0.05, 0.1, 0.2$ and 0.25) have been corrected for the slip velocity in order to arrive at the actual volume fraction of solids in the riser. The corrected volume fractions have been used to obtain the static pressure contribution of the solids i_s. Comparison between the model of Ferre and Shook (1998) and data of Xia et al. (2004a) shows good agreement as can be seen in Figure 2.1.

To assess the influence of wall friction on the slip velocity, we calculate the settling

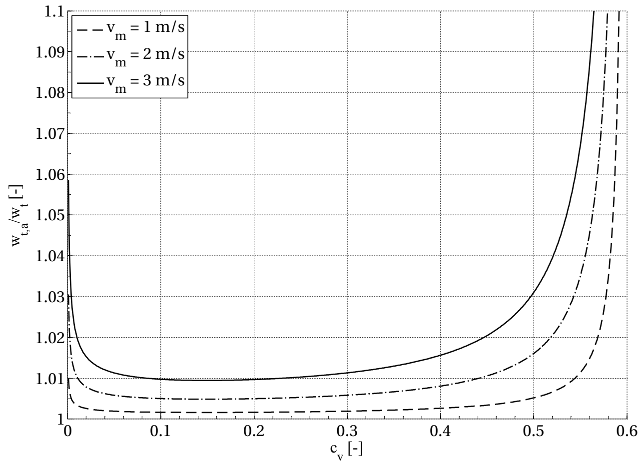

Figure 2.2: The settling velocity of a particle including the influence of wall friction, Equation 2.18, compared with the settling velocity without wall friction, Equation 2.10.

velocity $w_{t,a}$ of a particle with an additional friction force present. We assume that the wall shear stress τ_s as described by Equation 2.17 introduces an additional force $F_F = -V_p \cdot \frac{4 \cdot \tau_s}{c_v \cdot D}$ acting on the particle. Equilibrium of gravity $F_G = -V_p \cdot \rho_s \cdot g$, buoyancy $F_B = V_p \cdot \rho_f \cdot g$, drag $F_d = A_p \cdot C_D \cdot \frac{1}{2} \cdot \rho_f \cdot w_{t,a}^2$ and the additional friction force F_F, and elaboration for the terminal settling velocity with influence of wall friction $w_{t,a}$ gives:

$$w_{t,a} = \sqrt{\frac{4}{3} \cdot \frac{d}{\rho_f \cdot C_D} \cdot \left[\left(\rho_s - \rho_f\right) \cdot g + \frac{(1 - c_v)\, 4 \cdot \tau_s}{c_v \cdot D} \right]} \qquad (2.18)$$

Equation 2.18 has a vertical asymptote at $c_v = 0$ which has no physical meaning since wall friction is not present at zero volume fraction of solids.

In Figure 2.2 we show $w_{t,a}/w_t$ for $D = 154\,mm$, $d = 25\,mm$, $v_m = 1\,m/s$, $2\,m/s$ and $3\,m/s$. As can be seen, wall friction slightly increases the effective slip velocity, which has a small but stabilizing effect on the transport process. The maximum effect is well within 10 % increase in slip velocity.

In the next sections, the validity of hindered settling theory and the model for the kinematic wave velocity will be tested for fluidization of large particles. It will become clear that hindered settling theory gives a reasonable prediction of the relation between v_{slip} and c_v within a certain confidence interval, but it will also become clear that this confidence interval has a large impact on the assessment of stability.

2.3. FLUIDIZATION AND TRANSPORT EXPERIMENTS

2.3.1. TEST SETUPS

The experiments are conducted in the laboratory of IHC MTI in Kinderdijk, The Netherlands. The fluidization setup, Figure 2.3, consists of a loop with a single riser and downcomer, through which fresh water is pumped with a centrifugal pump (Linatex type $D4$, with a three bladed impeller). The suction side has $D_{suc} = 100\,mm$. The pump speed is controlled with a frequency drive. The pump's outlet is connected to a flow straightener: a bundle of small pipes suppressing rotation of the flow. The flow straightener also provides a steel wire grid for support of the bed of particles.

A transparent riser section is mounted on top of the flow straightener. Two risers are employed in successive experiments. The first has an inner diameter of $99.4\,mm$, with a length of $L = 2.7\,m$. The second has an inner diameter of $136.4\,mm$, with a length $L = 3.0\,m$.

Alongside the riser a large ruler is mounted so the vertical position of the particles can be monitored. The ruler has a blocked scale which measures $50\,mm$ per block. On top of the riser, there is a T-piece with on one end the particle inlet, and on the other end the exit of the riser towards a buffer tank. The buffer tank contains a steel grid to catch the particles. The bottom of the tank is connected to the downcomer ($D = 150\,mm$) that leads to the centrifugal pump's inlet.

A flow meter (a Krohne Optiflux 4000 with an inner diameter of $100\,mm$) and a temperature sensor (with a calibrated range of -25^oC to 100^oC and an accuracy of $0.1\,\%$) are mounted in the horizontal section before the pump inlet. Temperature fluctuations were very small, and an average water temperature of $T = 15^oC$ was measured.

A CCD video camera is used to record the fluidization column with a resolution of $720\,x\,576$ and a framerate of $25\,fps$. All sensors are logged with a frequency of $50\,Hz$.

The transport experiment test setup is a modification of the fluidization column, see Figure 2.3. The grid and flow straightener have been removed to allow circulation of particles. The flow sensor has been relocated to the downcomer, together with a temperature sensor. The riser section is equipped with a differential pressure sensor with a range $\Delta p = 0 - 160\,kPa$. The riser has a larger inner diameter, $D = 154\,mm$. During the experiments the water temperature was about $18\,^oC$.

2.3.2. TEST METHOD

A fluidization experiment starts with a packed bed of solid particles on the grid. The batch typically has a mass of about $5\,kg$. The initial batch height is measured. In order to assess the flow velocity range needed for each test, the pump is started and the water velocity is increased slowly until a volume fraction of solids $c_v \approx 0.1$ is obtained. The range between the velocity at $c_v \approx 0.1$ and zero velocity then is divided in fifteen to twenty steps typically. For a real test, the velocity is increased stepwise, and as a result of the increased velocity the bed of solids expands. Each newly set velocity is maintained for three minutes, so a new equilibrium can establish. The equilibrium bed height is measured by analysis of the camera recordings. Every frame the height is observed, the equilibrium bed height is the average of observed bed heights over the timespan of the flow step.

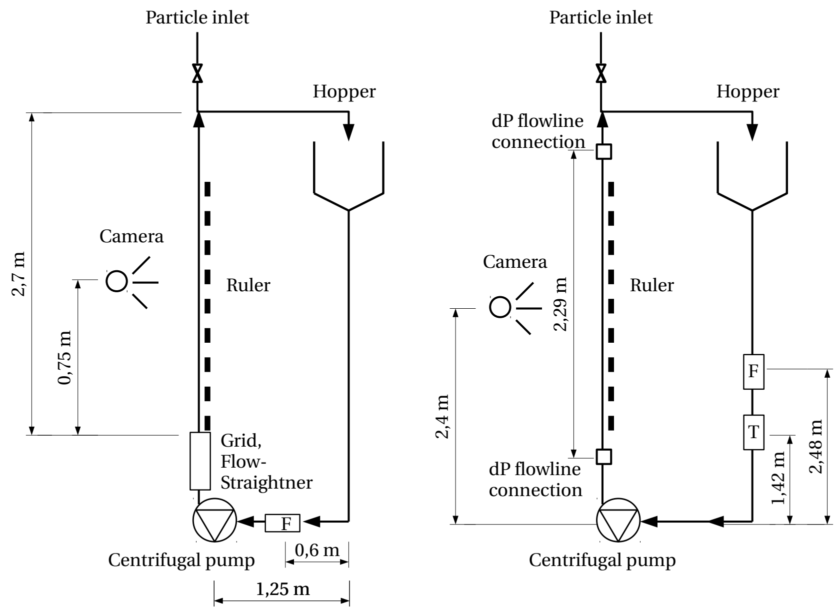

(a) Fluidization experiment test setup. (b) Transport experiment test setup.

Figure 2.3: Main parts and dimensions of the test setups. The fluidization column has inner diameters 99.4 mm and 136.4 mm (interchangeable section) and the transport experiment test setup has an inner diameter of 154 mm.

The initial volume fraction of solids is determined by measuring the particle's density ρ_s, the total mass of solids m_s and the initial bed height h_0. They are related by:

$$c_{v,0} = \frac{m_s/\rho_s}{0.25 \cdot \pi \cdot D^2 \cdot h_0} \tag{2.19}$$

The relation between the measured bed height h and the average volume fraction of solids in the riser $c_v(h)$ is given by:

$$c_v(h) = c_{v,0} \cdot \frac{h_0}{h} \tag{2.20}$$

The fluidization experiment primarily provides data relating fluid velocity and volume fraction of solids. Next to that we measure the kinematic wave velocities associated with the plugs by analysis of the video recordings (Section 2.4.2). Furthermore we use the fluidization experiment to determine the transition from plug flow to homogeneous fluidization, see Section 2.4.3.

The properties of the particles at test are summarized in Table 2.1. The diameter ratio d/D is given for $D = 99.4\,mm$ and $D = 136.4\,mm$. The water density at $T = 15\,^oC$ is $\rho_f = 999\,kgm^{-3}$, and the water viscosity is $\mu_f = 1.14 \cdot 10^{-3}\,Pa \cdot s$.

For the transport experiment we used the $d = 24.8\,mm$ particles from Table 2.1. Just above the centrifugal pump, there is an expansion piece from $D = 99.4\,mm$ to $D = 154\,mm$

Table 2.1: Properties of the glass beads used in the fluidization tests.

d [mm]	d/D	ρ_s [kg/m^3]
10.0	0.100, 0.073	2520
12.8	0.129, 0.094	2530
14.0	0.141, 0.103	2570
15.7	0.158, 0.115	2490
20.0	0.201, 0.147	2510
24.8	0.249, 0.182	2660
35.0	0.352, 0.257	2660

pipe. Due to continuity (i.e. F = constant), c_v increases over the expansion. This is the main disturbance source in the experiment, inducing kinematic waves. We then look at the propagation of this disturbance over the riser by visual observation and analysis of the camera recordings.

A transport experiment consists of gradually increasing the volume fraction of solids in the system by adding more and more particles while operating the system at a constant fluid velocity. We tested at several velocities in the range $0 < v_f < 2\,m/s$ to verify the velocity independency of the propagation of disturbances. The volume fraction of solids was varied in the range $0 < c_v < 0.3$ by inserting up to $50\,kg$ of glass beads in the system.

2.4. RESULTS AND DISCUSSION

2.4.1. VERIFICATION OF HINDERED SETTLING THEORY FOR LARGE PARTICLES

Upon fluidization, all particles first show plug flow with particle rain , however for the particles with $d = 10\,mm$ this was hardly visible. The larger d/D, the more pronounced the plug flow with particle rain. Ultimately at the end of each test, at the highest superficial flow velocity, the particle bed was at the onset of particle transport with no plugs present. Figure 2.4 shows the two main regimes encountered in the experiments.

The fluid velocity measured at equilibrium is compared with the outcome of Equation 2.7 using the measured volume fraction of solids, Equation 2.20. The terminal settling velocity w_t of a sphere is calculated by iteratively solving Equation 2.10 with the drag coefficient given by Equation 2.11. The hindered settling exponent n is calculated with Equation 2.9.

The comparison of the measured fluid velocities with the calculated fluid velocities according to hindered settling theory for all test data is shown in Figure 2.5. The lines indicate the ±25% confidence interval. There seems to be a minor nonlinearity in the data that is not covered by the model, e.g. the data show a slightly upward curve and has an asymmetric preference to the upperside of the $v_{f,measured} = v_{f,modelled}$ line. The mechanism behind this deviation is still matter of debate. Richardson and Zaki (1954) mentioned that for $d/D > 1/9$ their model failed. However, in these tests with $0.1 < d/D \leq 0.26$, the model seems to properly predict the hindered settling velocities.

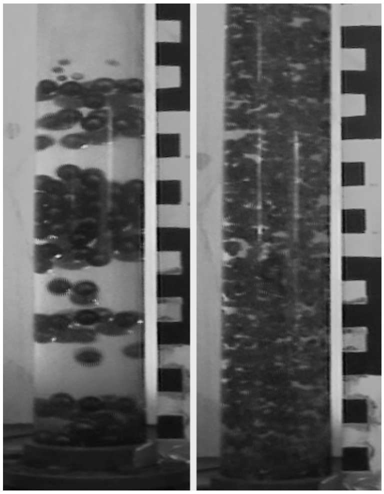

Figure 2.4: Glass beads ($d = 35\,mm$) in the plug flow mode with particle rain (left) and glass beads ($d = 10\,mm$) in the homogeneously fluidized state (right) in the $D = 136.4\,mm$ riser. Ultimately, every particle bed reached the particle transport mode when $v_f \rightarrow w_t$.

Given the fact that the data is well within the ±25% boundaries, we are confident that hindered settling theory is a good description of the slip velocities for particles with $d/D \leq 0.26$. Since typical mixture velocities in vertical transport systems are an order of magnitude larger than the slip velocities, the uncertainty of 25% will not have a large impact on any design calculation with hindered settling theory. We will however see that it has an impact on the calculation of the kinematic wave velocities.

2.4.2. THE PROPAGATION VELOCITY OF PLUGS

Now we have verified that hindered settling theory is well suited for describing the slip velocity of large particles in our fluidization test, the next step is to look at the propagation of disturbances. The plugs or disturbances observed in the experiments manifest themselves relative to the fluid velocity, Equation 2.14.

In order to find an estimate of the propagation velocity, we tracked the front of a disturbance in time (see Figure 2.6 for a typical situation). The camera has a framerate of $25\,fps$, so counting the number of frames nof needed for the front to propagate the distance Δz gives the front velocity $v_{front} = \Delta z \cdot 25/nof$.

We analyzed the front velocities of the $d = 15.7\,mm$ and $d = 20.0\,mm$ beads in the $D = 99.4\,mm$ fluidization column ($d/D = 0.16$ and $d/D = 0.20$) and the $d = 24.8\,mm$ and $d = 35.0\,mm$ beads in the $D = 136.4\,mm$ fluidization column ($d/D = 0.18$ and $d/D = 0.26$). In Figure 2.7 the front velocities relative to the superficial fluid velocity, $v_{front} - v_f$, are compared with the characteristic velocities of the mixtures relative to the fluid, $v_k - v_f$ (Equation 2.14 with v_f the measured superficial fluid). As can be seen the model predicts the order of magnitude reasonably well, but the scatter is very large. There does

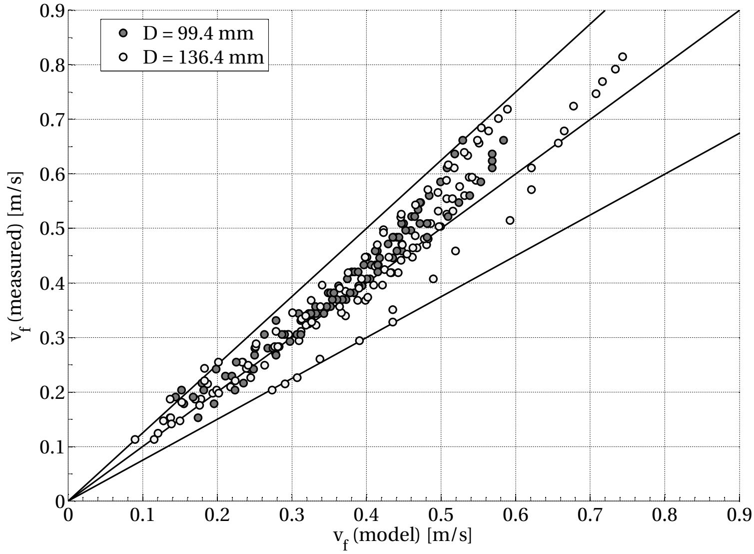

Figure 2.5: Velocities as measured in the fluidization column compared with model predictions of Equation 2.7. The particles have $d/D \leq 0.26$

.

not seem to be a strong relation between v_k and d/D, but from the data we know that especially at larger volume fractions of solids the error becomes large.

The next step is to look at the conditions under which the behaviour of the fluidized bed changes from plug flow (with particle rain) to a homogeneously fluidized bed, because this would give us insight in the validity of the $v_d = v_k$ criterion for regime transition. Since we found large scatter in the model predictions with Equation 2.14, it can be expected that the prediction of stability is uncertain as well.

2.4.3. REGIME TRANSITION FROM PLUG FLOW TO HOMOGENEOUS FLUIDIZATION

The flow regime can be indicated during the experiments by visual observation. The actual fluid velocity at regime transition, $v_{f,tr}$ can thus be deduced for all particle types. In the plug flow regime plugs travel upward, disintegrate and rain down again. This results in large fluctuations in bed height. A time lapse of camera observations of this process is shown in Figure 2.6. In case of homogeneous fluidization, the expanded bed height is much more stable. We define the velocity at regime transition $v_{f,tr}$ as the fluid velocity at which fluctuations in bed height are significantly diminished.

One way to look at the regime transition between plug flow and homogeneous fluidization is using the relation between the particle Reynolds number (at transition) $Re_{p,tr}$ and the Archimedes number Ar of the particles in the fluidized bed, as given by Rabi-

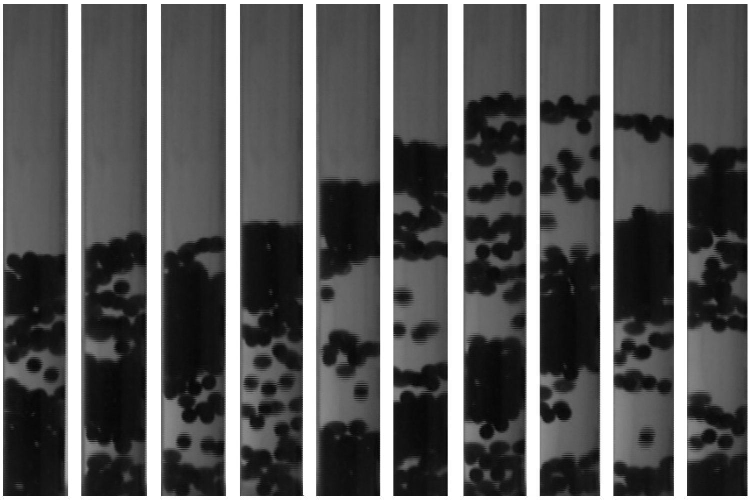

Figure 2.6: Time lapse ($\Delta t = 0.44\,s$ between frames) of particles with $d = 24.8\,mm$ in plug flow mode in the $D = 136.4\,mm$ riser. The plug accelerates upward and looses particles at the bottom upon increasing velocity.

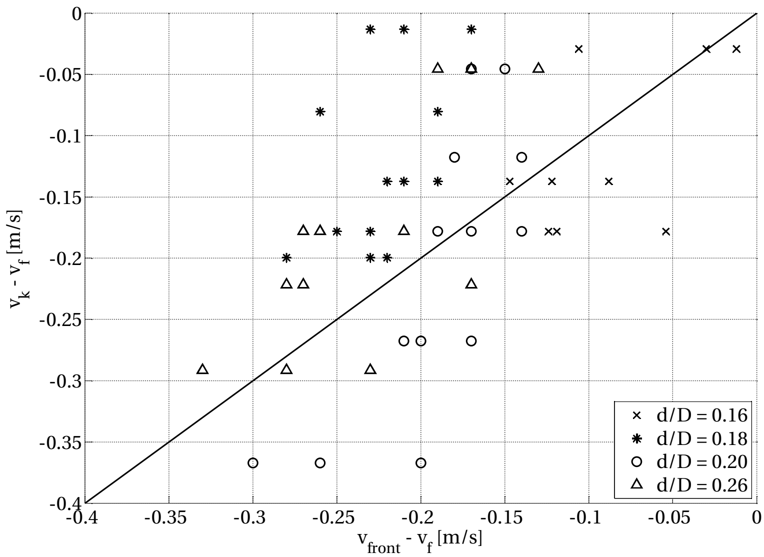

Figure 2.7: Measured front velocities compared with the kinematic wave velocity or characteristic velocity v_k, relative to the superficial fluid velocity v_f. The order of magnitude is predicted well, but the scatter is large.

novich and Kalman (2011):

$$Re_{p,tr} = a \cdot Ar^b \tag{2.21}$$

Equation 2.21 can also be formulated in terms of the superficial fluid velocity at regime transition $v_{f,tr}$:

$$Re_{p,tr} = \frac{\rho_f \cdot v_{f,tr} \cdot d}{\mu_f} \tag{2.22}$$

The Archimedes number Ar from Equation 2.21 is given by:

$$Ar = \frac{\rho_f \cdot (\rho_s - \rho_f) \cdot g \cdot d^3}{\mu_f^2} \tag{2.23}$$

The parameters a and b are used to fit the data to this framework.

The fluid velocity at regime transition between plug flow and homogeneous fluidization is determined by the velocity at which fluctuations in the expanded bed height diminish by visual observation. Table 2.2 shows the volume fraction of solids in the fluidized bed $c_{v,tr}$ and the fluid velocity $v_{f,tr}$ as measured at regime transition.

The particle Reynolds number at this point is defined by Equation 2.22. The $Re_{p,tr}$ values from the experiments are plotted versus the Ar numbers of the particles on a double log scale in Figure 2.8. The line in the plot is a least square fit to the data according to Equation 2.21. All data fit the general framework of Equation 2.21 well, although with coefficients different than found in Rabinovich and Kalman (2011). Once a and b are known for a specific batch of material, Equation 2.22 can be used for engineering purposes. To this end, first Ar is determined from the particle properties, with which $Re_{p,tr}$ can be determined. $Re_{p,tr}$ gives the fluid velocity through the batch at regime transition. The associated volume fraction of solids can be estimated with Equation 2.7, letting $v_{slip} = v_{f,tr}$. The volume fraction of solids thus found can be used as an upper limit for safe operation of the VTS.

We have shown that hindered settling theory is a good approximation of the particle slip velocities, and we have shown that based on our model, we are able to give a reasonable estimate of the kinematic wave velocities v_k. It is however the question whether the reasonable accuracy of the model in predicting v_k is sufficient to give a good prediction of the stability of the system.

The intersection between v_d and v_k should give the volume fraction of solids at the point of regime transition. However, comparison of v_d using Equation 2.3 and $v_k = w_t \cdot 10^{-d/D} \cdot c_v \cdot n \cdot (1 - c_v)^{n-1}$ (the ideal case in Equation 2.14 where the fluid velocity and hindered settling velocity cancel out) shows that $v_d > v_k$ for the fluidized beds examined in this research, so theoretically these fluidized beds should show stable behaviour.

This was clearly not the case and we anticipated that the accuracy in prediction of v_k is not sufficient for a stability analysis. Therefor we tried the full Equation 2.14, in which we substituted the measured value $v_f = v_{f,tr}$ from Table 2.2. The results were striking. Given the measured velocity at regime transition, the point of intersection $v_d = v_k$ corresponds almost perfectly with the measured volume fraction of solids at regime transition. A comparison between measurements and calculations is given in Figure 2.9.

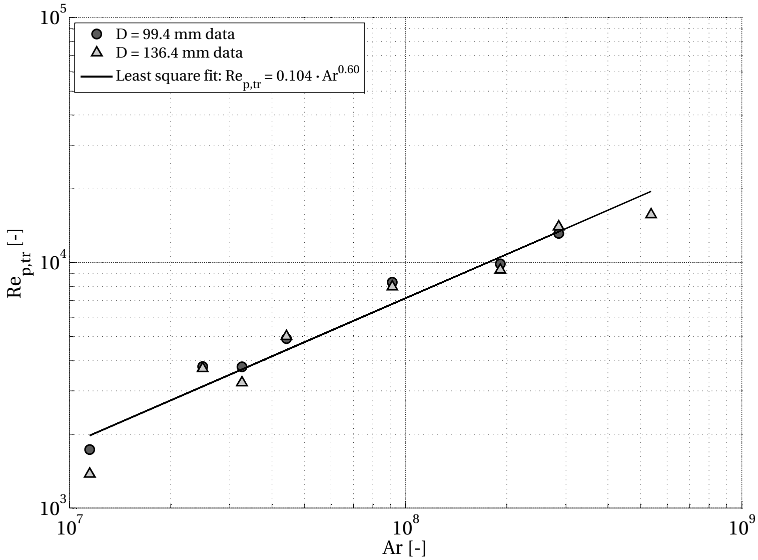

Figure 2.8: $Re_{p,tr}$ versus Ar at regime transition from plug flow to homogeneous fluidization. The data adheres to the general framework $Re_{p,tr} = a \cdot Ar^b$.

Table 2.2: Volume fraction of solids $c_{v,tr}$ and fluid velocity $v_{f,tr}$ at regime transition as measured in the fluidization experiments.

d $[mm]$	d/D	$c_{v,tr}$ $[-]$	$v_{f,tr}$ $[m/s]$
10.0	0.100, 0.073	0.38, 0.39	0.20, 0.19
12.8	0.129, 0.094	0.24, 0.17	0.34, 0.40
14.0	0.141, 0.103	0.25, 0.26	0.31, 0.32
15.7	0.158, 0.115	0.22, 0.15	0.36, 0.44
20.0	0.201, 0.147	0.12, 0.11	0.48, 0.55
24.8	0.249, 0.182	0.16, 0.19	0.46, 0.52
35.0	0.352, 0.257	n/a, 0.13	n/a, 0.62

Inclusion of added mass (i.e. using Equation 2.4 instead of Equation 2.3 for v_d) gives a minor difference, and Equation 2.3 gives the best result.

In this section we have shown that an accurate description of v_k is crucial in the prediction of the regime transition. This required using the full description of Equation 2.14, which only can be used if the actual fluid velocity v_f approaching the plug is accurately known. The theoretical description $v_k = w_t \cdot 10^{-d/D} \cdot c_v \cdot n \cdot (1-c_v)^{n-1}$ proved not to work well, so for stability analysis in the design phase fluidization tests with representative material samples are needed.

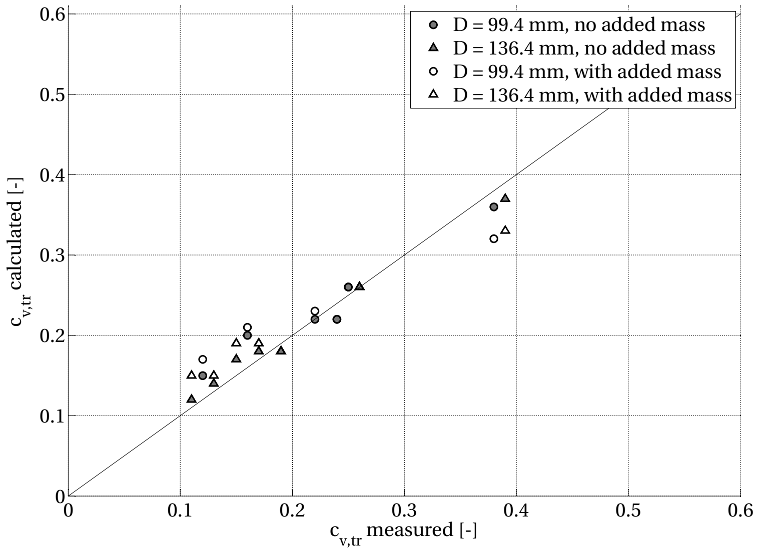

Figure 2.9: Volume fraction of solids at regime transition as calculated with $v_d = v_k$ (using $v_f = v_{f,tr}$ in Equation 2.14, and using Equations 2.3 and 2.4 for v_d) compared with the measured volume fraction of solids.

2.4.4. TRANSPORT EXPERIMENT: KINEMATIC WAVE VELOCITIES DURING TRANSPORT OF SOLIDS

In the transport experiment we investigate the flow regimes and propagation velocities of disturbances of the $d = 24.8\,mm$ glass beads in a $D = 154\,mm$ riser. The main difference with the fluidization experiment is the circulation of particles in a continuous loop.

The mass inserted in the loop is a measure of the volume fraction of solids in the riser, but since a part of the material is suspended in the return line and in the pump, the actual c_v in the riser will be smaller. We therefor use the additional information of the Δp measurement. The pressure difference over a vertical pipe comes from frictional losses and the static weight of the mixture. In the latter we are interested. For a proper estimation of c_v from a Δp measurement, one should use a U-tube setup with both a Δp sensor in the riser and return line. Furthermore, these lines should have equal diameters without any obstructions, so one can safely assume that the mixture wall friction is equal in both the riser and return line and the Δp readings are associated with the static weight only (Clift and Manning-Clift, 1981).

For our setup this unfortunately is not possible, so we will use the Δp readings of the riser corrected for the fluid contribution to wall friction. The distance between the flowline connections of the sensor is $L = 2.26\,m$, so we expect the pressure drop due to wall friction in the PVC pipe to be $\Delta p_f = f \cdot L/D \cdot 1/2 \cdot \rho_f \cdot v_f^2$ with $f \approx 0.01$ for PVC (conservative estimate). At $v_f = 1.90\,m/s$ (maximum velocity in the experiments), this would give $\Delta p_f = 0.30\,kPa$, which is of the same order as the submerged weight at small c_v. Because of the water-filled impulse tubes, the Δp sensor does not measure the pressure of the water, so the volume fraction of solids follows from:

$$c_v \approx \frac{\Delta p - \Delta p_f}{g \cdot L} \cdot \frac{1}{\rho_s - \rho_f} \tag{2.24}$$

The video recordings are analyzed for the occurring flow patterns. It was observed that the fluid velocity did not influence the observed transport regime. Up to $c_v = 0.06$ we observed random particle motion in the riser. From $c_v = 0.11$ towards $c_v = 0.22$ we observed propagating disturbances, and up to $c_v = 0.3$ the disturbances become more and more densely packed.

When we look at the relation $Re_{p,tr} = 0.104 \cdot Ar^{0.6}$ which we found for the fluidization experiments, and if we assume that this relation is also valid for the larger $D = 154\,mm$ riser, we find $Re_{p,tr} = 9.88 \cdot 10^3$. The associated fluid flow through the solids then is $v_{f,tr} = 0.45\,m/s$, which coincides with a volume fraction of solids at regime transition of about $c_{v,tr} = 0.22$ (using our data on the hindered settling velocity of the $d = 24.8\,mm$ glass beads). This number is supported by the observations in our transport experiment. The relatively clear demarcation between flow regimes that was found in the fluidization experiments however was not found in this transport experiment.

The next step in the analysis is comparing the propagation velocity of a disturbance with Equation 2.14.

In Section 2.2.3 we have shown that wall friction increases the effective slip velocity of the particles. The larger part of the measurements are taken at velocities $v_f < 1\,m/s$, so for $0 < c_v < 0.3$ we expect the slip velocity to increase up to 1.2 % at maximum (Figure 2.2, $v_f \approx \overline{v_m} = 1\,m/s$ graph at $c_v = 0.3$). From our fluidization experiments it proved that we were able to predict the particle slip velocity within 25 % accuracy, while the anticipated increase in slip velocity is much smaller. We will therefor neglect the influence of wall friction in our analysis.

The slip velocity v_{slip} can either be calculated or measured in a fluidization experiment. We use Equation 2.7. Since the characteristic velocity manifests itself relative to the fluid, we can track the front of a disturbance for a few frames (with a frame rate of $30\,fps$) in the same way as was done for the fluidization experiment.

As an example we look at Experiment 8. Figure 2.10 shows three video stills. The lines show the position of the front of a disturbance, propagating upward. The first and last frame are 39 frames apart, in which the front has propagated over $0.60\,m$. This results in an absolute velocity of $v_{front} = 0.60\,m \cdot 30/39 = 0.46\,m/s$ at a superficial fluid velocity of $v_f \approx 0.5\,m/s$.

This method has been used for all experiments, tracking a few disturbances per experiment. In these tests close up recordings were used. The front of a disturbance was tracked over a $0.30\,m$ distance, giving a velocity of $v_{front} = 0.30 \cdot 30/nof\ m/s$.

The results are shown in Figure 2.11. The measured data is presented as $v - v_f$ (i.e. velocities with respect to the superficial fluid velocity). The dynamic wave velocity v_d is modelled using Equation 2.3, without added mass. Putting v_d in the same frame of reference the fluid velocity through the batch needs to be known, which is approximated as $w_t \cdot 10^{-d/D} \cdot (1 - c_v)^n$. The kinematic wave velocity v_k is modelled with Equation 2.14,

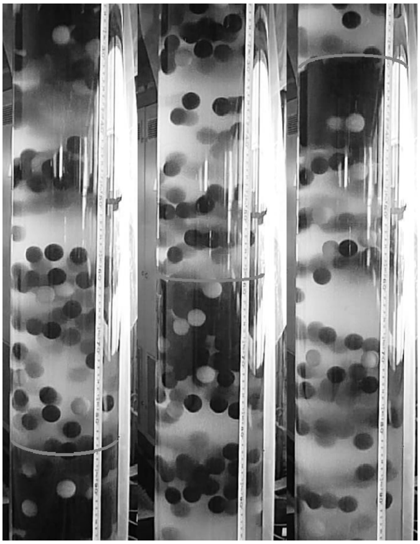

Figure 2.10: Example of the propagation of a disturbance through the riser ($\Delta t = 0.43\,s$ between frames).

and v_f is simply subtracted. The shock velocities according to Equation 2.15 are shown for $c_{v,l} = 0.1, 0.2, 0.3, 0.4$. In all graphs shown in Figure 2.11 we use $d = 24.8\,mm$ and $\rho_s = 2660\,kg/m^3$ for the glass beads, $\rho_f = 1000\,kg/m^3$, $\mu_f = 1.1 \cdot 10^{-3}\,Pa \cdot s$ for the water, in a riser with $D = 154\,mm$.

The fluidization data clearly shows that the disturbances or density waves are propagated with shock velocities $v_{s,k} < v_k$ (note that the fluidization tests were conducted in a $D = 136.4\,mm$ riser, but the difference with a $D = 154\,mm$ riser is negligible). The data is shown for the average volume fraction c_v, but note that in the case of shock velocities, the horizontal axis denotes the volume fraction of the disturbance. A fair comparison between the test data and the shock velocities requires information about the axial distribution of the volume fraction of solids, which we unfortunately do not have. As an indication, one can assume that the disturbances associated with the test data have larger volume fractions than the averages depicted in the figure, so for comparison with the shock velocities the data should be shifted to the right. On average the VHT test data follows the transport velocity v_s, which means that the observed disturbances were just advected with the flow. Towards $c_v = 0.3$ however larger wave velocities are observed, which resemble actual density waves.

While in the fluidization experiments we found kinematic wave velocities that matched Equation 2.14 well, and we were thus able to assess the regime transition from plug flow to fluidized flow, the vertical transport experiments show differently. The propagation velocity of disturbances is much smaller than both the theoretical velocities and the velocities found in the fluidization experiment. Since $v_k << v_d$, the stability criterion is

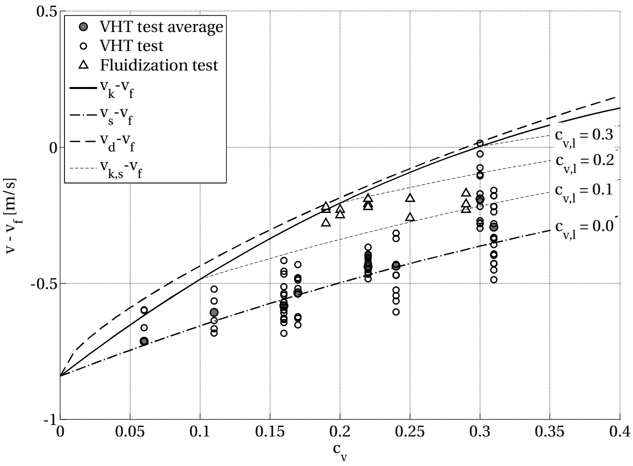

Figure 2.11: Measured propagation velocity of the front of a disturbance in the VHT tests corrected for the superficial fluid velocity. The measurements have been conducted at different fluid velocities and volume fractions of solids. Additionally, the results of the $d = 24.8\,mm$ glass beads fluidization test are shown. The theoretical lines for $v_k - v_f$, $v_{k,s} - v_f$, $v_d - v_f$ and $v_s - v_f$ show how the experiments fit the theoretical framework.

met for all c_v, so it can be concluded that vertical transport of solids shows stable behaviour, i.e. all disturbances will eventually diminish.

The question which now emerges, is whether we can generalize the conclusion from our transport experiment. In Section 2.2.3 we reasoned that wall friction only has a small effect on the slip velocities, but if present, friction would decrease the kinematic wave velocities with respect to the superficial fluid velocity, which is in line with our experiment. The measured v_k is however much smaller than would be expected from friction. This observation points at stability of our transport system, but extended experiments in a longer test setup are needed to verify this.

2.5. THE FLUIDIZATION OF IRREGULARLY SHAPED PARTICLES

2.5.1. FLUIDIZATION TESTS WITH GRAVEL

THE batch of $d \approx 14\,mm$ gravel is polydisperse, but with a narrow particle size distribution. The particle density is $\rho_s = 2700\,kg/m^3$. When fluidization starts, minor bed motions are observed, similar to the bed behaviour of the monodisperse batches of glass beads. When the fluid velocity increases, some parts of the bed remain in place, while others are highly turbulent. Due to the relatively large contact areas between particles, which depends on particle shape, the internal friction in the bed is expected to be much larger than in the case of glass beads. This results in far less homogeneous bed behaviour at relatively low fluid velocities than observed during fluidization of glass beads. When the fluid velocity further increases, the fluidized flow regime is entered and the batch is homogeneously dispersed. Here the polydispersity of the batch comes in: flat, relatively large particles quickly move upward while the smaller, more spherical particles remain in the lower section of the riser. The fluidization column separates particles according to drag forces. Furthermore, by visual observation, the volume fraction of solids is rather large at the bottom of the setup, while it is clearly smaller at the top. This behaviour was observed in both the $D = 99.4\,mm$ and $D = 136.4\,mm$ risers. Figure 2.13 shows the fluidized stage with particle separation.

The larger $d \approx 20\,mm$ gravel has a density $\rho_s = 2850\,kg/m^3$. These particles showed differences in behaviour between the $D = 99.4\,mm$ and $D = 136.4\,mm$ risers. Fluidization in the smallest riser was hard. The gravel remained in the plug flow mode and plugs were not able to accelerate. Wall friction is expected to be large for these relatively large and irregularly shaped particles at large volume fractions of solids. In some occasions, blockage of the riser was found. The plug then could be moved by increasing the pressure (by adjusting the revolutions of the pump), but the only method to disintegrate the plug was to shut off the flow and let the plug rain down. Figure 2.12 shows a blockage with gravel just above the particle bed in the $D = 99.4\,mm$ riser.

Fluidization of the $d \approx 20\,mm$ gravel in the $D = 136.4\,mm$ riser gave no problems. The gravel showed plug flow with particle rain similar to glass beads of the same size. A typical situation is depicted in Figure 2.12. Here it can be seen that besides plugs, also some minor clustering occurs.

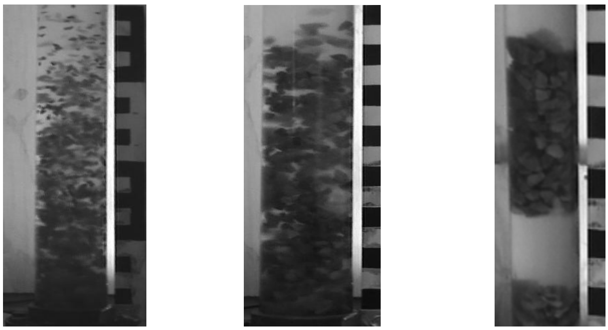

(a) $d \approx 14\,mm$ gravel in the $D = 136.4\,mm$ riser. (b) $d \approx 20\,mm$ gravel in the $D = 136.4\,mm$ riser. (c) $d \approx 20\,mm$ gravel in the $D = 99.4\,mm$ riser.

Figure 2.12: Fluidization of the $d \approx 14\,mm$ gravel and $d \approx 20\,mm$ gravel in the $D = 136.4\,mm$ riser and the formation of a blockage of $d \approx 20\,mm$ gravel in the $D = 99.4\,mm$ riser.

The main purpose of the fluidization experiments was to establish the relation between v_f and c_v in order to validate the use of our modeling equations for non-spherical particles. Figure 2.13 shows the results. We used Equation 6.37 for modeling w_t, from which C_D was derived, and we used Equation 6.28 combined with the model of Rowe (1987) for n. As can be seen, the model predictions for the fluidization in the $D = 136.4\,mm$ riser are very satisfying, but the results in the $D = 99.4\,mm$ riser are poor. This is in line with the observed behaviour during the experiments: fluidization of gravel in the smallest riser was hardly possible. Wall friction plays an important role in this case, which is not covered in the model. Up to $d/D = 20/136.4 \approx 0.15$ in the $D = 136.4\,mm$ riser we are confident with the model results, but for larger ratio's the differences become too large.

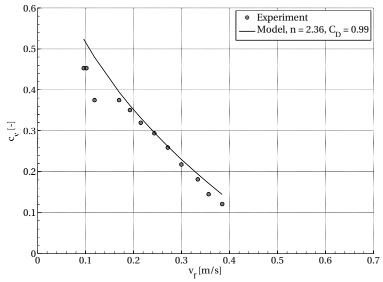

(a) Fluidization of $d \approx 14\,mm$ gravel in the $D = 136.4\,mm$ riser, $d/D = 0.10$.

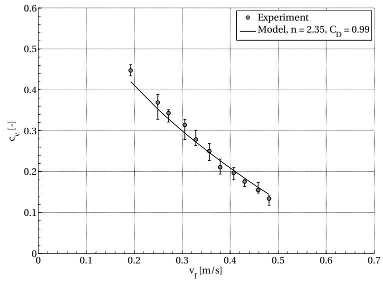

(b) Fluidization of $d \approx 20\,mm$ gravel in the $D = 136.4\,mm$ riser, $d/D = 0.15$.

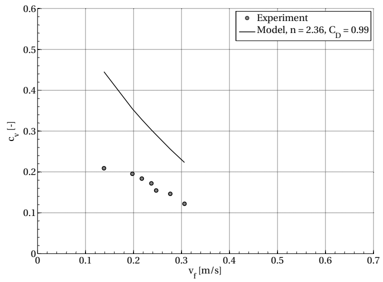

(c) Fluidization of $d \approx 14\,mm$ gravel in the $D = 99.4\,mm$ riser, $d/D = 0.14$.

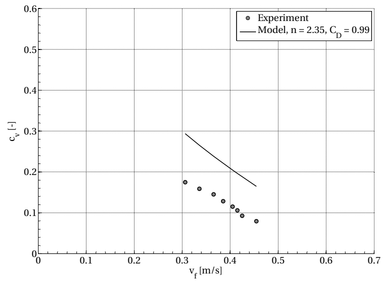

(d) Fluidization of $d \approx 20\,mm$ gravel in the $D = 99.4\,mm$ riser, $d/D = 0.20$.

Figure 2.13: Comparison between measurements and model equations for fluidization of the $d \approx 14\,mm$ gravel and $d \approx 20\,mm$ gravel in the $D = 99.4\,mm$ and $D = 136.4\,mm$ risers. Up to $d/D = 20/136.4 \approx 0.15$ in the $D = 136.4\,mm$ riser we are confident with the model results, but in the smaller riser a smaller d/D should be used.

2.5.2. FLUIDIZATION TESTS WITH FLAT PARTICLES

It was observed that gravel shows the tendency of minor cluster formation (a local agglomeration of particles) at low velocities, while the perfectly spherical glass beads only showed plugs that span the entire riser diameter. The main difference between both particle types is particle shape. In order to assess the influence of particle shape, three types of extremely flat particles have been subjected to fluidization tests. Table 2.3 summarizes their properties. The sphericity of slate has been determined by measuring the volume of twenty randomly selected particles from the tested batch. Then the average volume and the average particle thickness has been determined, based on which the sphericity can be calculated.

The first test comprised fluidization of a polydisperse, narrowly graded batch of slate

Table 2.3: Properties of the flat particles used in the fluidization tests.

Type	d [mm]	d/D	t [mm]	ρ_s [kg/m^3]	**Sphericity** ϕ
Slate	≈ 30	$\approx 0.3, 0.2$	$4-8$	2700	≈ 0.5
steel disc	12	$0.12, 0.08$	1	7000	0.43
Polymer disc	40	$0.4, 0.27$	4	1500	0.47

in the $D = 136.4\,mm$ riser according to the method used for glass beads and gravel. Upon increasing the fluid velocity, the bed proved not to expand at all. Upon increasing the pump revolutions at almost zero flow, the bed could be set into motion as a solid entity. Wall friction however was very large due to the very angular particles and the relatively soft material of the transparent riser, which resulted in a stick-slip like process with very low velocity. Ultimately, the batch of slate got stuck, which is shown in Figure 2.14. The very flat particles form a structure with low permeability: the pressure drop over the structure increases and the flow declines (which is a property of the centrifugal pump). The flow through the pores then becomes so small, that resuspension of the plug is impossible. After a while, the bottom part of the structure obtained a wedge shape due to the water forcing its way along the path of least resistance.

A second strategy now was employed, in which slate particles were inserted via the particle inlet in a pre-set fluid flow. Once suspended, particles showed very irregular behaviour by gliding and tumbling through the riser. Aligned perpendicular to the flow, the large drag force resulted in upward acceleration, while a sudden re-alignment of the particle in parallel direction resulted in a quick downward motion. During all unsteady motions, the particles frequently collided with the riser wall. On some occasions, a single particle got stuck to the wall, aligned with the flow, and it remained in place.

Another remarkable observation was particles clustering after collision with each other. Once they collided, they stuck to each other and behaved as an entity. By collecting other particles due to random collisions, the cluster rapidly grew to a large single cluster. Upon collision with the wall, the cluster got stuck and obtained a wedge shape due to parallel alignment of the outer particles with the flow. The cluster thus obtained is depicted in Figure 2.14. Eventually, this cluster grew into a plug spanning the entire diameter of the riser.

At this point it is clear that flat particles make up structures with low permeability, thus prohibiting fluidization and forcing the structure to behave as an entity. The slate particles suffered from very high wall friction, which occasionally resulted in riser blockage. It is expected that discs show the same behaviour due to their flatness, but plugs of discs are expected to induce less wall friction. The second test therefor comprised a bed of steel discs, which was fluidized starting with zero flow. The formation of two types of structures was observed. The first was the bed of particles obtaining a wedge like shape, resulting in an asymmetric cluster being forced to the wall. Due to the wedge shape of the cluster, this structure got stuck and did not move upon increasing flow. Figure 2.14 shows this phenomenon, which is very similar to the wedge like structure obtained with the slate particles. Obviously, these structures result from the particles being flat, particle circularity does not play a role.

The second structure that was observed, is a symmetric plug with a rounded upstream shape, like a bullet. The upward flow forces itself around the plug, resulting in this shape. The plug was seen to rotate freely around its axis of symmetry, indicating friction between the plug and the riser wall is almost zero. Increasing the pump's revolutions resulted in upward transport of the plug. Due to flow instabilities around the plug, eventually it was forced to the wall and it obtained a wedge shape, with water flowing past the plug in the gap between the plug and the riser wall. Figure 2.14 shows the bullet shaped plug.

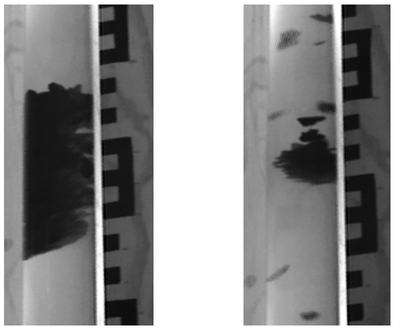

(a) Slate stuck in the $D = 136.4\,mm$ riser.
(b) A cluster of slate in the $D = 136.4\,mm$ riser.

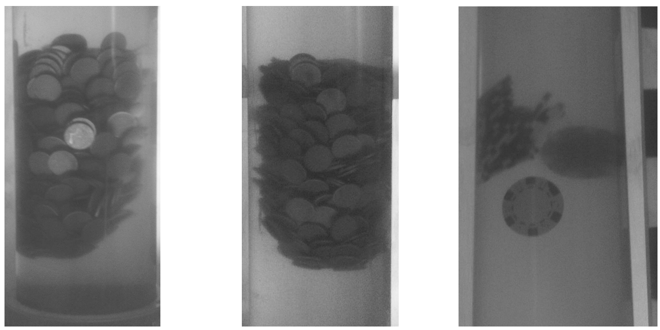

(c) A cluster of steel discs in the $D = 136.4\,mm$ riser.
(d) A plug of steel discs in the $D = 136.4\,mm$ riser.
(e) Polymer discs in the $D = 136.4\,mm$ riser.

Figure 2.14: Fluidization of slate, steel discs and polymer discs. The slate agglomerates in the riser and forms a solid plug. Starting the fluidization of a bed of steel discs with zero flow, a wedge like cluster was formed and forced to the wall, upon which it got stuck. The bullet–shaped plug was obtained during fluidization at low fluid velocity. Wall friction was almost zero, and the plug was free to move around, gradually following flow fluctuations. Upon a sudden increase of fluid velocity, the plug was forced to the wall and a wedge-like shape occurred. The polymer discs show a wall attached cluster similar to those observed for the slate.

So far, the slate and steel discs both showed wedge-shaped clusters attached to the wall. In both cases, these shapes were obtained by water forcing its way along the path of least resistance. However, the slate particles were also able to form clusters starting wit a single particle being attached to the wall in an upward flow, and by collisions between several particles. For the steel discs this phenomenon was not observed. The steel discs were able to form symmetric plugs, while this was not observed for the slate particles.

When the single slate particles were attached to the wall and got stuck, it was observed that they were aligned under a small angle in flow direction. The outer edges of the particle were supported by the wall by means of point contact in a horizontal plane, so the particle could flip and make the small angle. If this indeed is the mechanism by which wall-attached clusters can form, the same phenomenon would be expected for the polymer discs with larger diameter. Once suspended in an upward flow, the polymer discs were indeed able to get stuck to the wall in the same way the slate particles did. By collecting other discs, clusters would grow. Figure 2.14 shows a set of polymer discs attached to the wall under a small angle.

The relative particle diameter d/D clearly is the determining factor in the onset of wall-attached plugs of flat particles. When the particle diameter is sufficiently large compared to the curvature of the riser wall, the particle is able to flip around a horizontal axis perpendicular to the flow. The upward water flow then forces the bottom part of the particle to the wall, thus resulting in a three-point contact between the particle and the riser. The resulting drag force on the particle forces it to the wall, so the particle remains in place and is able to collect other particles by random collision.

2.6. CONCLUSIONS AND RECOMMENDATIONS

2.6.1. CONCLUSIONS

We have validated our model equations with fluidization experiments. We used glass beads with diameters in the range $d = 10 - 35\,mm$ with densities around $\rho_s = 2500\,kg/m^3$ and $d/D < 0.26$, comparable to real deep sea deposits in prototype scale transport systems. We have shown that for large d/D ratios, classic hindered settling theory still predicts the solid phase slip velocity within reasonable limits of $\pm 25\%$.

The kinematic wave velocity was derived from hindered settling theory. By analysis of the influence of wall friction on the solid phase slip velocity, we have shown that wall friction has a very small, but stabilizing effect on the vertical transport operation because it decreases the kinematic wave velocities.

We analyzed the propagation velocity of shock-fronts as a measure of the kinematic wave speed v_k, and compared these with the theoretical v_k. The order of magnitude of the measured shock-front velocities in the fluidization experiments is predicted well by the theoretical v_k, but especially at larger volume fractions of solids the model overestimates v_k.

In the fluidization experiments we measured the fluid velocity and volume fraction of solids at regime transition from the plug flow regime (associated with bed instabilities) to the homogeneously fluidized regime. The data adheres to the general framework $Re_{p,tr} = a \cdot Ar^b$, which indicates we have consistently identified the regime transitions. We were able to give a good prediction of the volume fraction of solids at regime transition $c_{v,tr}$ with the criterion $v_d = v_k$, using Equations 2.3 and 2.14, substituting $v_f = v_{f,tr}$ (the measured fluid velocity at the point of transition). Accurate prediction of v_k is key for stability analysis.

In the transport experiment we measured the propagation velocity of disturbances for $0 < v_f < 2\,m/s$ and $c_v < 0.3$. We observed propagation of disturbances over the entire range of c_v. The associated kinematic wave velocities proved to be much smaller than the theoretical kinematic wave velocity or shock velocities. It seems like these disturbances were just advected with the particle transport velocity. The much smaller propagation velocities of the disturbances points, on theoretical grounds, at an increased flow stability of the transport system compared to a fluidized bed. The decrease in kinematic wave velocities during transport is in line with the theoretical influence of wall friction on the transport process, but wall friction only cannot explain the extreme reduction in v_k.

Continuation of the fluidization experiments with irregularly shaped particles revealed interesting features relating to particle shape. The slip velocity of angular material like crushed rock can be modeled with hindered settling theory, provided the d/D ratio does not become too large (which is to be determined with a fluidization test). Flat particles however tend to form clusters that either move freely in the flow or attach to the riser wall. The clustering behaviour seems to relate to sphericity, while the tendency to form wall attached clusters seems to relate to the relative particle size. Cluster formation cannot be modeled with the continuum model presented in this thesis.

2.6.2. RECOMMENDATIONS

The outcome of a stability analysis is very sensitive to the choice of models for v_k and v_d, so for stability assessment of long distance vertical transport systems, it is advised to conduct laboratory tests with representative particle samples. A simple fluidization test would already give insight in the flow stability of the transport system, and thus can be used to find the upper allowable limit of the volume fraction of solids. Using a design rule of the form $Re_{p,tr} = a \cdot Ar^b$ can be a valuable addition to fluidization tests.

In our experiments we used monodisperse mixtures, but in practice the particle size distributions will be much wider. It would be interesting to investigate the influence of significant amounts of finer material (e.g. $d < 5\,mm$) in the transport system. We expect the stability conditions to improve, because the presence of finer material would effectively decrease the particle slip velocity.

In the transport experiment the propagation velocities of disturbances matched the average fluid velocity. Apparently, demarcation between density waves and normal advection of solids is very hard in a moving frame of reference. The experiment could be largely improved if it would be possible to measure the axial distribution of the volume fraction of solids. In this way, density waves and their velocities could be discerned more easily. In order to draw firm conclusions on system stability a larger scale (L/D) transport system is needed with which the long distance propagation of plugs can be studied.

The fluidization experiments with large particles have shown that particle sphericity is an important parameter. Angular material at $d/D < 0.15$ gave no problems in the fluidization experiments, while flat particles did. More research into the relation between particle shape and hydrodynamic behaviour is recommended.

3

EXPERIMENTAL STUDY OF THE AXIAL DISPERSION OF SOLIDS

In this chapter the vertical hydraulic transport of batches of solids is experimentally explored to get insight in the influence of solids on the axial dispersion process. The axial dispersion coefficient is determined by analysis of the decay of the volume fraction of solids over the coarse of transport. It is related to the Taylor dispersion coefficient. The analysis shows that the presence of solids attenuates axial dispersion such that it plays a minor role in the transport process, particularly for coarse sediments.

This chapter has been published in Ocean Engineering **92** (2014) Van Wijk et al. (2014a).

3.1. INTRODUCTION

THis chaper is concerned with the vertical hydraulic transport of individual batches of solids. Vertical transport distances in deep sea mining operations typically are hundreds to thousands of meters. With these large transport distances, irregular feeding of the riser can result in the development of batches of solids or plugs.

In the 1DVHT model, the combined action of axial stretching of the batch and turbulent mixing is modelled as a diffusion term in the advection-diffusion equation. The diffusion term represents particle dispersion, which Talmon and Van Rhee (2011) model as axial dispersion for turbulent pipe flow according to Taylor (1954). Evans and Shook (1991) adopted the same method and they conducted vertical transport experiments with sand ($d_m = 0.175\,mm$) and fine gravel ($d_m = 4.1\,mm$). They found that the axial dispersion of sand indeed could be modelled well by Taylor dispersion, but for the fine gravel their measurements were inconclusive. Since axial dispersion counteracts the development of steep gradients in the volume fraction of solids this process is beneficial for prohibiting the formation of plugs.

In this chapter the axial dispersion of suspended sediment in vertical pipe flow is experimentally investigated in order to find out whether axial dispersion plays a significant role in attenuation of plugs.

3.2. THEORY OF AXIAL DISPERSION

THe transport of suspended solids or dense granular flows can be approximated as a continuum (Jop et al., 2006), which enables the use of the advection-diffusion equation:

$$\frac{\partial c_v}{\partial t} + \frac{\partial (c_v \cdot v_s)}{\partial z} = \frac{\partial}{\partial z} \cdot \left(\epsilon_z \cdot \frac{\partial c_v}{\partial z} \right) \tag{3.1}$$

From Equation 3.1 it becomes clear immediately that axial dispersion is relevant for the cases with large gradients in the volume fraction of solids $\partial c_v / \partial z$, i.e. in the case of plug development. Continous solids input with minor variations will result in $\partial c_v / \partial z \approx 0$, and in these cases axial dispersion is of minor or even no importance.

An important hallmark in the theory of axial dispersion is Taylor (1953), who studied the dispersion of a solvent flowing through a horizontal pipe in the laminar regime. He used a parabolic velocity profile for the horizontal pipe (i.e. Poiseuille flow), from which he calculated the axial stretching of the solvent. The solvent propagates faster along the centerline than at the wall of the pipe. Molecular diffusion causes mixing of the solvent over the pipe diameter. It proved that axial dispersion could be expressed analogous to a diffusion coefficient, like $\epsilon_z = D^2/4 \cdot v_f^2/(48 \cdot \epsilon_m)$, with ϵ_m being the coefficient of molecular diffusion.

In Taylor (1954), this theory was extended to the case of transport by turbulent flow through a horizontal pipe. Again the analogy with a virtual diffusion coefficient was sought, and it showed that for turbulent flow, the molecular diffusion coefficient ϵ_m is negligible compared to the turbulent eddy viscosity. For transport of a solvent in turbulent pipe flow Taylor (1954) introduces the axial dispersion coefficient:

$$\epsilon_z = 10.1 \cdot \frac{D}{2} \cdot \sqrt{\frac{\tau_f}{\rho_f}} \tag{3.2}$$

The wall shear stress for clear fluid τ_f depends on the pipe properties and flow properties. It is given by:

$$\tau_f = \frac{f}{8} \cdot \rho_f \cdot v_f^2 \tag{3.3}$$

By dimensional analysis Eckstein et al. (1977) pointed out that solid particles migrating under shear at very low Reynolds numbers show self-diffusion coefficients of the form:

$$\epsilon \propto d^2 \cdot \left|\frac{\partial v}{\partial r}\right| \cdot f(c_v) \tag{3.4}$$

Self-diffusion primarily causes dispersion of the particles perpendicular to the direction of shear, but the velocity gradient associated with shear inherently causes axial dispersion as well. Griffiths and Stone (2012) apply this principle to horizontal hydraulic transport of colloidal-size particles through a pipeline. They assume the axial dispersion coefficient ϵ_z to be the sum of dispersion due to Brownian particle motions (molecular diffusion), ϵ_m, and a shear induced component which depends on particle properties and the volume fraction of solids:

$$\epsilon_z = \epsilon_m + d^2 \cdot \left|\frac{\partial v}{\partial r}\right| \cdot f(c_v) \tag{3.5}$$

Christov and Stone (2014) apply this shear induced axial dispersion model to an inclined flow of dense granular material. To this end, they assume that the dense granular flow can be approximated as a continuum having a constant volume fraction of solids. They further assume a no–slip condition between the bottom layer of particles and the slope, so a half parabolic velocity profile emerges and from this the shear rate could be calculated. Christov and Stone (2014) suggest to investigate the influence of variation in the volume fraction of solids and to provide experimental verification of the theory.

The vertical hydraulic transport of coarse granular material in a pipe (coarse sand and gravel, with $d/D = O(10^{-1})$, for which it can be assumed $\epsilon_m = 0$), as studied in this chapter, is in the basics much alike a dense granular flow, and a strong relation between the axial dispersion and shear rate could be expected according to Equation 3.5. There are however some complicating factors.

First, the local volume fraction of solids is all but constant during transport due to the nonlinear relation between the solids transport velocity and the volume fraction of solids and due to the dispersion of material. Finding $f(c_v)$ is not trivial.

Second, the no–slip condition does not hold for vertical transport. Visual observation with a high speed camera, of which video stills are shown in this chapter (Figures 3.4 and 3.5), show that particles close to the pipe wall propagate with velocities close to the bulk velocity. Especially for large volume fractions ($c_v \geq 0.2$) the particles proved to move en bloc. The friction between the particles and the riser wall should be larger than the interparticle friction to induce significant shear in the batch.

When the suspended solids in a turbulent pipe flow would be just tracer particles, the axial dispersion coefficient would be given by Equations 3.2 and 3.3. Suspended sediments with larger dimensions and densities are expected to influence the axial dispersion process. Evans and Shook (1991) showed that particle size influences the axial dispersion process, but they were not able to quantify the axial dispersion for fine gravel. Sumner et al. (1990) conducted vertical transport experiments in order to measure the radial distribution of the volume fraction of solids and the solids velocity in a vertical pipe for different types of sand ($d_m = 0.16\,mm$, $d_m = 0.47\,mm$ and $d_m = 0.78\,mm$), gravel ($d_m = 1.7\,mm$) and plastic beads ($d_m = 0.29\,mm$ and $d_m = 1.5\,mm$). Their measurements suggest that the velocity profile is not influenced by the volume fraction of solids or particle diameter (in the range $0.1 < c_v < 0.4$). They did however find a significant influence of particle size on the radial distribution of the volume fraction of solids. The coarser the material, the more the material gets concentrated in the core of the pipe. Since the shear rate of fluid is largest in the boundary layer, axial dispersion will be smaller when particles are mainly suspended in the core of the flow.

Suspended particles physically interact at large volume fractions, with interparticle friction suppressing relative motions and thus axial dispersion. At smaller volume fractions particles have sufficient space to move. This expected dependency on solids volume fraction is not present for dissolved matter. Sadlej et al. (2010) used numerical simulations of particle drops in a Poiseuille flow at low Reynolds numbers to show how hydrodynamic interactions influence the axial dispersion of the particle drops. The simulations show that the larger the initial volume fraction, the smaller the axial dispersion, with approximately a factor two difference in axial dispersion between the $c_v = 0.05$ case and the $c_v = 0.5$ case.

A third and important parameter that influences axial dispersion is particle inertia. Vames and Hanratty (1988), Govan et al. (1988) and Lee et al. (1989) experimentally studied the dispersion of solid particles and droplets in turbulent vertical air flows. Highly inert particles are hardly influenced by turbulent eddies, while the smallest particles without any significant inertia perfectly follow flow fluctuations. These researchers use a time constant t_p to characterize particle inertia:

$$t_p^{-1} = \frac{3 \cdot C_D \cdot \rho_f \cdot w_t}{4 \cdot d \cdot (\rho_s - \rho_f)} \tag{3.6}$$

For the bulk flow the characteristic time is given by:

$$t_f = \frac{D}{\overline{v_m}} \tag{3.7}$$

The ratio of t_p and t_f is known as the Stokes number Stk:

$$Stk = \frac{t_p}{t_f} = \frac{4 \cdot (\rho_s - \rho_f) \cdot d \cdot \overline{v_m}}{3 \cdot \rho_f \cdot D \cdot w_t \cdot C_D} \tag{3.8}$$

The influence of increasing inertia on the dispersion coefficient of solids has been simulated by Uijttewaal and Oliemans (1996). They simulated vertical pipe flow of air with suspended solids using DNS and LES techniques. The volume fractions of solids was kept sufficiently small ($c_v < 10^{-3}$) so the particle interaction could be neglected. In this way, only particle inertia had a significant effect on the axial dispersion coefficient. They observed a rapidly diminishing dispersion coefficient for increasing inertia. Their results are not quantitatively comparable to the case of sediment transport studied in this chapter, for they used particles in an airflow, the volume fraction of solids in our case will be much larger and they used the friction velocity and viscosity to define the time scale of the flow field, i.e. $t_f = \sqrt{\tau_f/\rho_f}/\nu_f$. The friction velocity is poorly defined in our experiments, since we look at solid batches with a large volume fraction of solids, so the choice for the bulk velocity is more convenient. Although not quantitatively comparable, the observed effect of decreasing dispersion with increasing particle inertia in the work of Uijttewaal and Oliemans (1996) is of importance for our research.

Summarized, Taylor dispersion for turbulent pipe flow as given in Taylor (1954) can be seen as an upper limit for the axial dispersion coefficient. When sediments are transported instead of soluble matter, the shear rate (due to a changing velocity profile of the suspension) is altered by particle size, particle inertia and the volume fraction of solids. These particle parameters are included in Equation 3.5. In this chapter we measure the axial dispersion coefficient by looking at the deformation of the $c_v(z,t)$ signal during the propagation of a batch of solids. We then present the measured axial dispersion relative to the Taylor dispersion coefficient for turbulent pipe flow.

3.3. SEDIMENT TRANSPORT MODEL

In dynamic transport conditions, with influence of both advection (the transport velocity of solids is a nonlinear function of c_v) and dispersion on the changing volume fraction of solids, it is very hard to exactly measure the shear rate or velocity profile within a batch of solids. In the experiments we therefore measure the volume fraction of solids and bulk velocity, from which we want to deduce the axial dispersion coefficient for each experiment. In order to isolate the contribution of axial dispersion to the deformation of the batch, we need to correct for the influence of advection.

The initial condition of a typical experiment resembles a pulse, which during propagation shows a decrease in peak height due to the influence of advection and axial dispersion. Correction of the measurements for the advection term is achieved by using a modified hindered settling formula (Equation 6.27). The Richardson and Zaki exponent is set $n = 1$. If the observer moves with the flow, only the maximum relative velocity w_t is of importance, and Equation 3.1 becomes the well-known Burgers' Equation:

$$\frac{\partial c_v}{\partial t} + \frac{\partial c_v \cdot w_t \cdot (1 - c_v)}{\partial z} = \frac{\partial}{\partial z} \cdot \left(\epsilon_z \cdot \frac{\partial c_v}{\partial z} \right) \tag{3.9}$$

The Burgers' equation uses $n = 1$, which results in a small underestimation of the advective contribution to the decrease in peak height (an error smaller than 1% for coarse gravel based on numerical analysis of the advection equation). The Burgers' Equation has an analytical solution (Nieuwstadt, 1998) given by:

$$c_v(l,t) = \frac{C}{2} \cdot \left(-\tanh\left(\frac{2 \cdot C \cdot w_t \cdot l}{4 \cdot \epsilon_z} \right) + \frac{l}{L_{batch}} \right) \tag{3.10}$$

In Equation 3.10, l is the local spatial coordinate in the batch. The coefficient C given by:

3

$$C = \frac{c_{v,0}}{1 + c_{v,0} \cdot \frac{w_t \cdot t}{L_{batch}}} \tag{3.11}$$

Equations 3.10 and 3.11 will be used in Section 3.5 to correct the measurements.

3.4. TEST SETUP

THE test-setup, situated in the IHC MTI laboratory in Kinderdijk, consists of a centrifugal pump with a suction diameter of $D = 100\,mm$, a riser section with an internal diameter of $D = 99.4\,mm$ and an effective length $L = 7780\,mm$ made of transparant PVC and a downcomer section, shown in Figure 3.1. The riser section is equipped with a differential pressure sensor (Rosemount with a range of $0 - 37\,kPa$), four conductivity concentration sensors (see Appendix B), a temperature sensor and an electromagnetic flow sensor (Krohne Optiflux 4000) that measures fluid velocity v_f. Furthermore, the riser section is monitored with one high speed camera at the top ($1000\,fps$) and two conventional digital cameras at the bottom and mid section (both $60\,fps$). These elements make up the outer flowloop in which the actual experiment takes place.

As can be seen in Figure 3.1, there is also an inner flowloop. This loop is used to load the setup with solids. The inner loop contains a knife gate valve, on which a layer of particles (sand, gravel or polystyrene granulate) is installed. The initial volume fraction of solids for an experiment can be varied by loading more or less material on top of the knife gate valve in the inner flowloop. Then the flow in the outer flowloop is started until a constant velocity is obtained. Once at steady state, the knife gate valve is opened and the bottom part of the outer flowloop is closed, while the inner flowloop is opened. In this way the batch of solids is forced into the outer loop and the actual measurements begin. The CCM's measure the cross sectional averaged volume fraction of solids in time at four positions in the riser. An experiment comprises the transport of a batch from the bottom CCM to the top CCM.

The experiments aim at quantification of the axial dispersion coefficient of several types of particles, relative to the Taylor dispersion coefficient of Equation 3.2. The properties of the particles are summarized in Table 3.1. Sand and gravel have been chosen because their shapes and densities very much resemble the properties of particles encountered in real deep sea mining applications. The polystyrene granulate is chosen because it has a density that is almost equal to the density of water. This results in $w_t \to 0$, hence suppressing the nonlinear term $v_s(c_v)$ in Equation 3.1.

Table 3.1: Properties of the particles used in the flowloop tests.

Type	d $[mm]$	d_{50} $[mm]$	ρ_s $[kg/m^3]$	w_t $[m/s]$
Polystyrene granulate	–	3.0	1050	0.04
Fine Sand	0.2 – 0.5	0.39	2650	0.09
Coarse sand	0.8 – 1.25	1.05	2650	0.14
Fine gravel	5.0 – 8.0	6.34	2650	0.35
Coarse gravel	8.0 – 16.0	12	2650	0.48

The cumulative particle size distributions of the fine sand, coarse sand and fine gravel

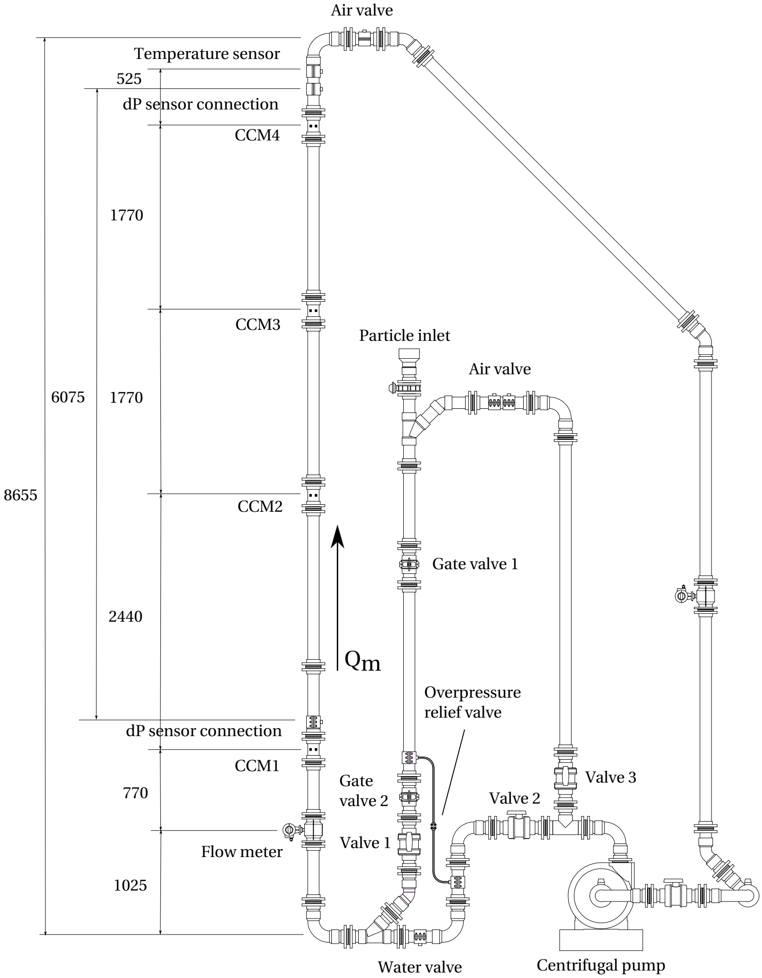

Figure 3.1: Schematic layout of the flowloop with all sensors. Dimensions in mm.

are presented in Figure 3.2. The polystyrene granulate has a somewhat cylindrical shape, with a length of 3.0 mm and a diameter of about 1.0 mm.

After launching the batch, dilution occurs due to the lower bend and the sudden change from downward acceleration towards upward transport. This however has no negative consequences for the measurement, since the output of the bottom CCM is the initial condition in the riser. The entire series of experiments is summarized in Table 3.2. The variation in initial bed height on the valve, h_0, directly relates to variation in the initial volume fraction of the batch at the bottom CCM. Each experiment consists of one or two passages of the batch through the riser, since the system is a closed circuit.

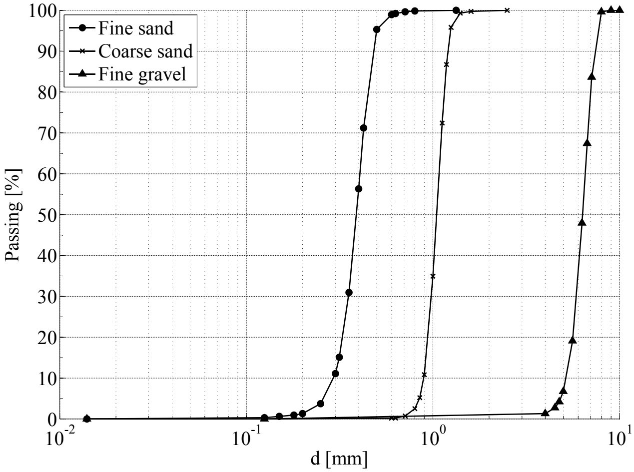

Figure 3.2: Cumulative particle size distributions of the fine sand, coarse sand and fine gravel.

Table 3.2: Overview of the series of experiments.

Experiment	**Particle**	d_{50} $[mm]$	ρ_s $[kg/m^3]$	h_0 $[m]$
1	Polystyrene granulate	3.0	1050	0.5
2	Polystyrene granulate	3.0	1050	1.0
3	Polystyrene granulate	3.0	1050	2.0
4	Fine Sand	0.39	2650	0.5
5	Fine Sand	0.39	2650	1.0
6	Fine Sand	0.39	2650	2.0
7	Coarse sand	1.05	2650	0.5
8	Coarse sand	1.05	2650	1.0
9	Coarse sand	1.05	2650	2.0
10	Fine gravel	6.34	2650	0.5
11	Fine gravel	6.34	2650	1.0
12	Fine gravel	6.34	2650	2.0
13	Coarse gravel	12	2650	0.5
14	Coarse gravel	12	2650	1.0
15	Coarse gravel	12	2650	2.0

3.5. RESULTS AND DISCUSSION

3.5.1. GENERAL METHOD OF ANALYSIS

IN the transport experiments, both advection and axial dispersion play a role. A batch of solids is tracked on its way through the riser while monitoring the deformation of the batch in time. That is, the four CCM's measure the cross-sectional averaged conductivity of the mixture in time, $k_m(t)$. This signal has to be converted to the cross sectional averaged volume fraction of solids in time, $c_v(t)$. The conversion from conductivity to volume fraction relies on the principle that the conductivity of a mixture decreases with increasing volume fraction of solids. In the orignal paper, on which this chapter is based, the Bruggeman equation as given by Nasr-El-Din et al. (1987) is used for this conversion, relating mixture conductivity to the fluid conductivity k_f:

$$\frac{k_m}{k_f} = (1 - c_v)^{3/2} \tag{3.12}$$

At the time of these experiments we had not yet investigated the relation between grain size and the CCM's performance, since we did not have any reason so far to doubt their performance. When we studied the conservation of mass of a batch, based on our measurements, we found out that the calibration of the CCM's needed more attention. In Appendix B we describe the calibration of the CCM's for different grain sizes. We found that for plastic grains, fine sand and coarse sand a linear relation between k_m/k_f and c_v gives good results:

$$\frac{k_m}{k_f} = 1 - c_v \tag{3.13}$$

For fine gravel and coarse gravel an alternative correlation is used:

$$\frac{k_m}{k_f} = 1 - c_v^{\zeta} \tag{3.14}$$

In Equation 3.14, $\zeta = 1.3$ gives a good compromise between accuracy and practical use with our data. In this chapter we have updated the figures using the new calibration. There is some significant difference in the absolute values of c_v as presented in Van Wijk et al. (2014a) and as found in this chapter. The consequences of the different calibrations for the present analysis and the conclusions we have drawn in Van Wijk et al. (2014a) are however minor, since we devised a method of analysis that uses relative values of c_v rather than absolute values.

As can be seen, the conductivity of the fluid k_f is needed to calculate c_v. In order to obtain accurate values of both k_m and k_f, the CCM's are calibrated every test by matching the CCM output for clear water (k_f) with the output of a portable conductivity probe.

The CCM recordings of a typical experiment are shown in Figure 3.3, this figure shows Experiment 9. It can be seen that the peak volume fraction rapidly decreases after each passage. This is due to the many bends and the pump, that introduce a lot of dispersion of the material. As a criterion for usable data, $c_v \geq 0.07$ is used.

In order to get a feeling on the relative importance of advection over axial dispersion for an experiment, a Peclet number is used:

$$Pe = \frac{w_t \cdot L_{batch}}{\epsilon_z} \tag{3.15}$$

The Peclet number shows the importance of advection over axial dispersion. It depends on the terminal settling velocity w_t (which is a good indication of the order of

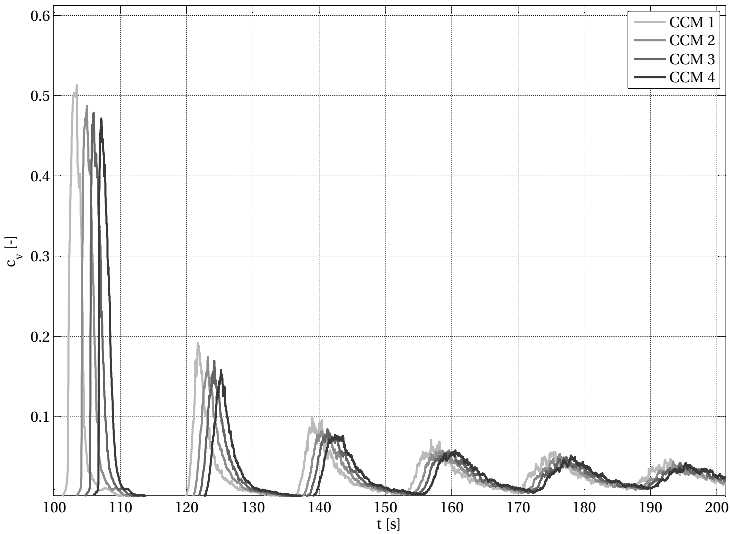

Figure 3.3: Measured volume fraction of solids during the transport of coarse sand through the riser (Experiment 9 from Table 3.2).

magnitude of the slip velocity), the batch length L_{batch} and the axial dispersion coefficient ϵ_z. For $Pe >> 1$, advection is the dominant process, while for $Pe << 1$, axial dispersion dominates.

Next to Pe, also Stk needs to be known. Both numbers require $\overline{v_m}$ to be known for each experiment. The setup is equipped with a flow meter, but this meter lags behind the actual passage of a batch. A more accurate estimation of $\overline{v_m}$ can be obtained by looking at the average batch transport velocity $\bar{v}_s$:

$$\overline{v_s} = \frac{\Delta z}{\Delta t} \tag{3.16}$$

For the average velocity from CCM1 to CCM4, the average time needed for propagation from CCM1 to CCM4 is given by:

$$\Delta t_{14} = \frac{5.98}{\overline{v_s}} \tag{3.17}$$

In Equation 3.16 $\Delta z = 5.98\,m$ is the distance between CCM1 and CCM4, and Δt is the time for propagation of the batch between the CCM's. By using a cross-correlation technique, the velocities are obtained and the results for $\overline{v_s}$, Pe and Stk as shown in Table 3.3 are obtained. The results are given for the first (denoted with 1) and second (denoted with 2) run of a batch through the outer loop.

From the measurements it is hard to derive the axial dispersion coefficient directly. It is however possible to define a parameter which is proportional to the axial dispersion

Table 3.3: Average batch velocity $\overline{v_s}$,,propagation time Δt_{14}, Peclet number Pe and Stokes number Stk of the experiments. Numbers 1 and 2 denote the first and second run of the batch through the riser.

Exp.	$\bar{v}_s 1$ $[m/s]$	$\bar{v}_s 2$ $[m/s]$	$\Delta t_{14} 1$ $[s]$	$\Delta t_{14} 2$ $[s]$	$Pe1$ $[-]$	$Pe2$ $[-]$	$Stk1$ $[-]$	$Stk2$ $[-]$
1	1.93	1.89	3.09	3.17	0.49	0.50	0.09	0.09
2	1.90	1.94	3.15	3.09	1.00	0.98	0.09	0.09
3	1.93	2.10	3.10	2.85	1.97	1.81	0.09	0.10
4	1.66	1.74	3.61	3.44	1.12	1.07	0.18	0.19
5	1.57	1.78	3.81	3.36	2.36	2.09	0.17	0.19
6	1.47	2.02	4.06	2.97	5.05	3.69	0.16	0.22
7	1.66	1.73	3.60	3.46	1.74	1.67	0.31	0.32
8	1.62	1.81	3.68	3.31	3.56	3.20	0.30	0.33
9	1.35	1.84	4.43	3.25	8.56	6.28	0.25	0.34
10	1.50	1.55	3.99	3.85	4.82	4.65	0.67	0.69
11	1.54	1.62	3.88	3.68	9.38	8.90	0.69	0.72
12	1.32	1.70	4.53	3.52	21.9	17.0	0.59	0.76
13	1.66	1.98	3.61	3.03	5.98	5.02	1.02	1.21
14	1.43	1.58	4.18	3.80	13.9	12.6	0.88	0.97
15	1.21	1.55	4.94	3.87	32.7	25.7	0.75	0.95

coefficient ϵ_z, but much easier to determine from the data. For an observer moving with the batch, without influence of the nonlinear advection of solids, it follows from the analytical solution of the diffusion equation that at the peak of the batch ($z = 0$) the volume fraction $c_v(0, t)$ is inversely proportional to the square root of the axial dispersion coefficient. This fact will be exploited when defining a parameter δ_D such that $\delta_D \propto \epsilon_z$. The peak height of the batch at arrival time $t = t_i$ is $c_{v,i}$, where i is the index of the CCM. When ϵ_z = constant during the transport of the batch from one CCM to another, it holds:

$$c_{v,1} \propto \frac{1}{\sqrt{\epsilon_z \cdot t_1}} \tag{3.18}$$

and:

$$c_{v,4} \propto \frac{1}{\sqrt{\epsilon_z \cdot t_4}} \tag{3.19}$$

so it follows:

$$\frac{1}{c_{v,1}^2} - \frac{1}{c_{v,4}^2} \propto \epsilon_z \cdot (t_1 - t_4) \tag{3.20}$$

Since $t_1 - t_4 < 0$ (the batch arrives at CCM1 first), and since for an experiment $\Delta z/\overline{v_s} \approx constant$, the above can be rewritten to:

$$\frac{1}{c_{v,4}^2} - \frac{1}{c_{v,1}^2} \propto \epsilon_z \tag{3.21}$$

and:

$$c_{v,4}^2 \cdot \left(\frac{1}{c_{v,4}^2} - \frac{1}{c_{v,1}^2} \right) \propto \epsilon_z \tag{3.22}$$

resulting in:

$$\frac{c_{v,1}^2 - c_{v,4}^2}{c_{v,1}^2} \propto \epsilon_z \tag{3.23}$$

δ_D then is given by:

$$\delta_D = \frac{c_{v,1}^2 - c_{v,4}^2}{c_{v,1}^2} \tag{3.24}$$

By using δ_D it is not possible to quantify ϵ_z exactly, but it enables the comparison of the different experiments, and it enables identification of dependencies of ϵ_z on sediment parameters. The deformation δ of a batch which follows from experiments contains information about both nonlinear advection (δ_A) and axial dispersion (δ_D). To isolate the influence of axial dispersion only, it is assumed that $\delta = \delta_A + \delta_D$, since both processes result in the peak volume fraction of the batch getting smaller. Once a saw-tooth shaped profile has developed from the nonlinear advection term, Equation 3.10 describes the deformation of the volume fraction profile in time. This solution can be used to estimate δ_A as:

$$\delta_A = \frac{c_v^2(0, t_0) + c_v^2(0, t_0 + \Delta t_{14})}{c_v^2(0, t_0)} \tag{3.25}$$

Now δ_A can be estimated by assuming the following parameters: $\epsilon_z \approx 0\, m^2/s$ ($\epsilon_z = 1 \cdot 10^{-8}\, m^2/s$ for computational reason), $L_{batch} = 3\, m$ and an initial volume fraction $c_{v,0} = \overline{c_v}$ (i.e. the average volume fraction over the period of transport from CCM1 to CCM4). The values of δ_A thus obtained are used in the next section, where the measurements are analysed. It proves that the expected decrease in peak height due to advection is almost ten times larger for the coarse gravel compared to the polystyrene granulate.

The last point that needs to be resolved before proceeding with the analysis of the experiments is finding the value of δ for the case of pure Taylor dispersion for the test setup. Consider a solute that is transported with $v_f = 2\, m/s$ and an initial volume fraction $c_{v,0} = 0.2$. The axial dispersion coefficient for this case was calculated as $\epsilon_z = 0.05\, m^2/s$. Numerical simulation of the test setup gives $\delta_{taylor,ref} = 0.5$. Since the fluid velocities are different each experiment, $\delta_{taylor,ref}$ can be scaled such that it represents the theoretical value for each experiment:

$$\delta_{Taylor} = \delta_{Taylor,ref} \cdot \frac{\overline{v_s}}{2.0} \tag{3.26}$$

The final step in the analysis is calculating the decrease in peak height due to axial dispersion δ_D with respect to the decrease in peak height due to pure Taylor dispersion δ_{Taylor} as $\frac{\delta_D}{\delta_{Taylor}}$.

3.5.2. TYPICAL RESULTS

The Peclet number shown in Table 3.3 indicates the dominance of advection over axial dispersion. In the experiments we have two extreme cases: on one hand the polystyrene granulate, on the other hand the coarse gravel. Upon launching a batch of polystyrene granulate through the riser, for which axial dispersion is dominant, the batch is expected to show dilution at both the top and the bottom of the batch. Figure 3.4 shows three screen captures of the high speed camera recordings of Experiment 3. The top of the

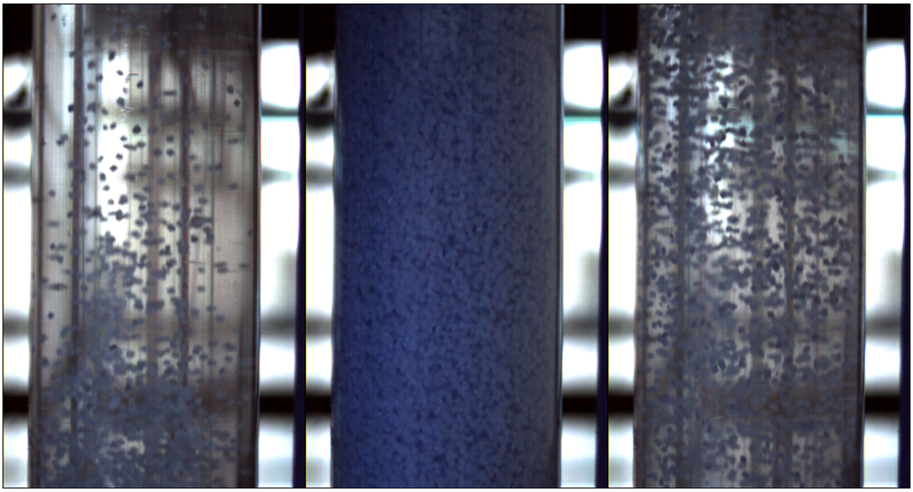

(a) Top section (b) Mid section (c) Bottom section

Figure 3.4: Screen captures of the top, mid section and bottom of a batch of polystyrene granulate passing the high speed camera at the top of the riser.

batch shows dilution, the mid section shows an increased volume fraction, while the bottom of the batch again is diluted. This picture is congruent with Figure 3.6, which shows the CCM recordings of Experiments 1, 2 and 3. The CCM recordings typically show symmetric volume fraction profiles, somewhat similar to Gaussian curves as encountered in the experiments of Taylor (1954). This again is an indication of axial dispersion being dominant for this material.

Figure 3.5 shows the high speed camera screen captures of Experiment 15. The top of the batch is very flat and thus shows a very large concentration gradient, while towards the bottom the batch gets more and more diluted. This picture is congruent with the CCM recordings of Experiments 13, 14 and 15. In these figures, large concentration gradients are found for the top of the batch (the part that passes the CCM earliest in time) and small gradients are found towards the bottom of the batch. This profile typically emerges from the nonlinear advection term in Equation 3.1.

The fine sand, coarse sand and fine gravel show the transition from a dominant axial dispersion process ($Pe < 2$ according to Table 3.3) towards a dominant nonlinear advection process ($Pe > 4$ according to Table 3.3). Figure 3.8 shows CCM recordings of Experiment 4, 7 and 11. The fine sand CCM recordings still resemble the behaviour of polystyrene granulate, but the coarse sand and fine gravel clearly show the sawtooth profile associated with the case where advection dominates the transport process.

3.5.3. RELATION BETWEEN THE AXIAL DISPERSION COEFFICIENT AND THE VOLUME FRACTION OF SOLIDS AND PARTICLE INERTIA

Figure 3.9 shows δ_D/δ_{Taylor} versus the volume fraction of solids. The data has been corrected for the nonlinear advection term. One fine sand measurement shows axial dis-

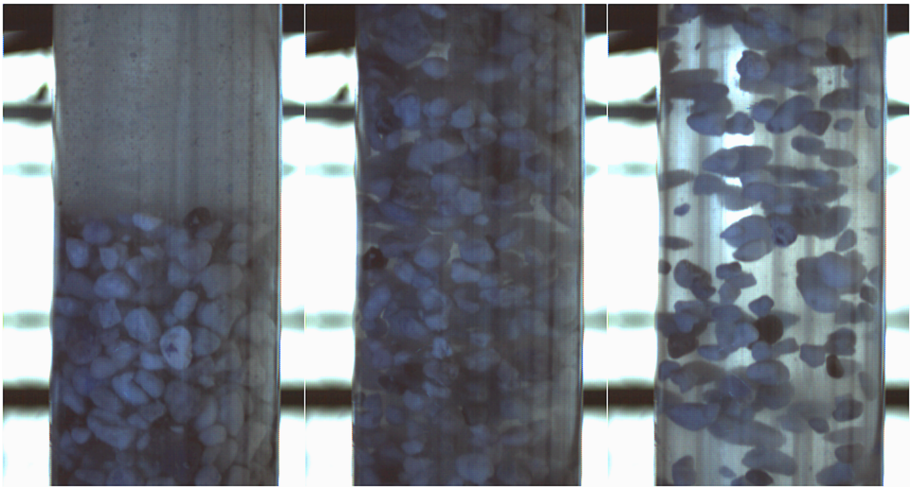

(a) Top section (b) Mid section (c) Bottom section

Figure 3.5: Screen captures of the top, mid section and bottom of the batch of coarse gravel passing the high speed camera at the top of the riser.

persion larger than Taylor dispersion, while practically all measurements show smaller dispersion. The polystyrene granulate shows axial dispersion closest to Taylor dispersion. We would expect δ_D/δ_{Taylor} getting smaller with increasing c_v. When comparing two sets of the same grain type at two different volume fractions, we see that the smallest δ_D/δ_{Taylor} corresponds with the largest c_v, but the dataset is too small to draw hard conclusions.

Figure 3.10 shows δ_D/δ_{Taylor} versus the Stokes number. Earlier work on vertical gas flows with suspended solids has shown that with increasing Stk the axial dispersion will decrease. Figure 3.10 shows large scatter in the fine sand measurements, where the two data points around $Stk = 0.2$ and $\delta_D/\delta_{Taylor} \approx 0.3$ are suspected to be outliers. Given the small inertia of fine sand and given the camera recordings and CCM recordings, we would expect the fine sand measurements to resemble the polystyrene granulate measurements. In that case, the general trend of decreasing axial dispersion with increasing Stk can be observed. Considering the possible outliers, the lower limit found in these tests is $\delta_D/\delta_{Taylor} \approx 0.4$ for fine gravel, while one measurement of coarse gravel even shows $\delta_D/\delta_{Taylor} \approx 0.15$.

3.6. CONCLUSIONS AND RECOMMENDATIONS

THE data provided in this chapter is not conclusive on the physics influencing the axial dispersion process, but its main contribution is showing that axial dispersion only has a small influence on the transport of coarse sediments. This is of importance to the hydraulic design and flow assurance computations of vertical hydraulic transport systems.

Axial dispersion decreases with increasing particle inertia (represented by the Stokes number). For neutrally buoyant particles the axial dispersion coefficient proved to be very close to the Taylor dispersion coefficient, so it is expected that Taylor dispersion demarcates the upper limit of dispersion. The gravel particles in our experiments hardly show axial dispersion. The dataset presented in this chapter shows that axial dispersion only plays a minor role in the vertical hydraulic transport of solids when $Stk > 0.3$. A lower limit of roughly 40% of the Taylor dispersion coefficient was found for fine gravel and 15% of the Taylor dispersion coefficient was found for coarse gravel during batch transport.

Comparison between two measurements at different values of c_v shows that for all grain types the larger c_v corresponds with the smaller δ_D/δ_{Taylor}. The dataset is however too small to draw very firm conclusions on the influence of c_v.

Nonlinear advection becomes the dominant process in vertical hydraulic transport for (roughly) $Pe > 4$, which would be the case for regular transport operations.

There is only little theory on axial dispersion in dense suspensions of coarse material. It would be very interesting to follow up on the recent developments in combining granular flow rheology models with the classic axial dispersion theory for fluids. The challenge is in finding the velocity profiles and associated shear rates $\partial v/\partial r$ in dense suspensions, and in finding the influence of the volume fraction of solids.

The test setup used in this chapter will be used again in Chapter 4 where the merging of different batches of solids and the risk of riser blockage will be investigated. The minor role of axial dispersion in the vertical transport process promotes the risk of riser blockage by batch merging.

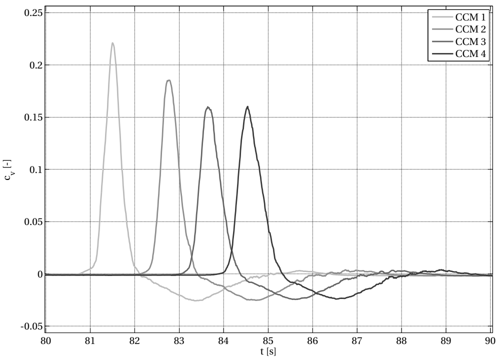

(a) Experiment 1

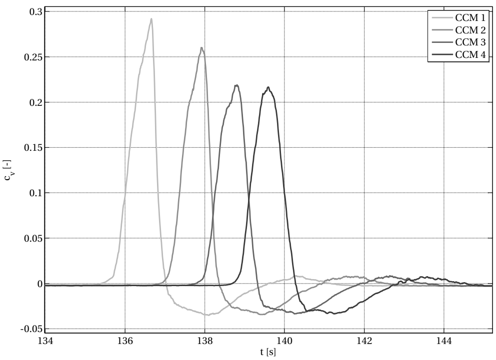

(b) Experiment 2

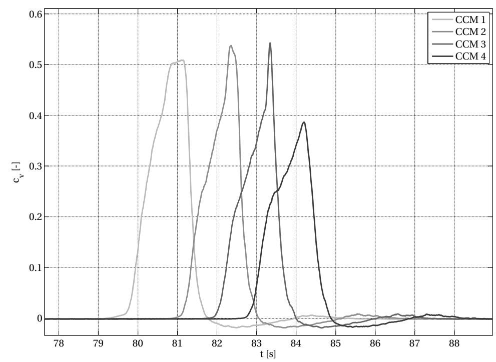

(c) Experiment 3

Figure 3.6: CCM recordings of Experiments 1, 2 and 3.

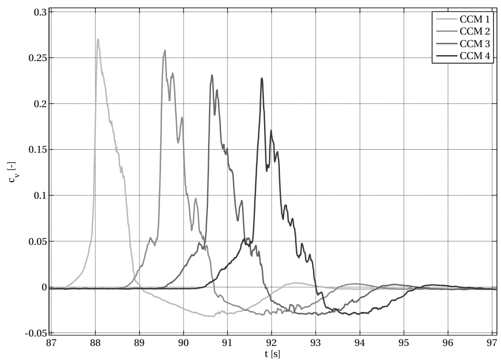

(a) Experiment 13

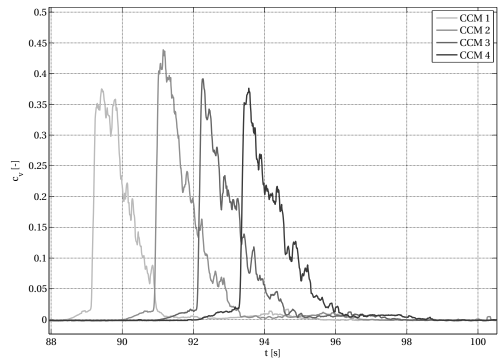

(b) Experiment 14

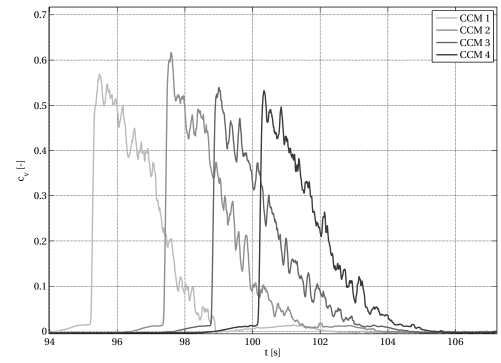

(c) Experiment 15

Figure 3.7: CCM recordings of Experiments 13, 14 and 15.

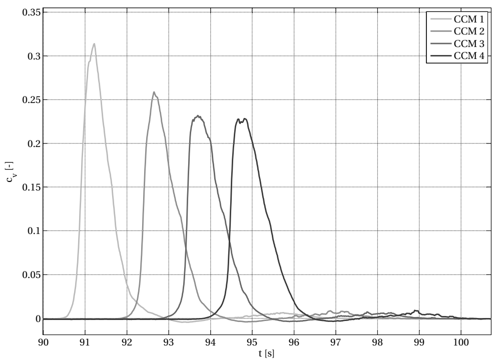

(a) Experiment 4

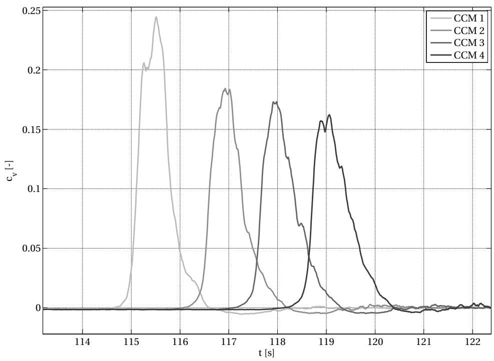

(b) Experiment 7

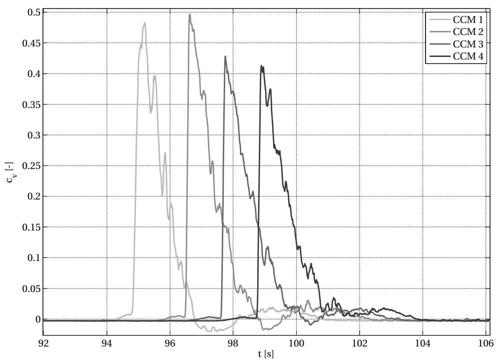

(c) Experiment 11

Figure 3.8: CCM recordings of Experiments 4, 7 and 11.

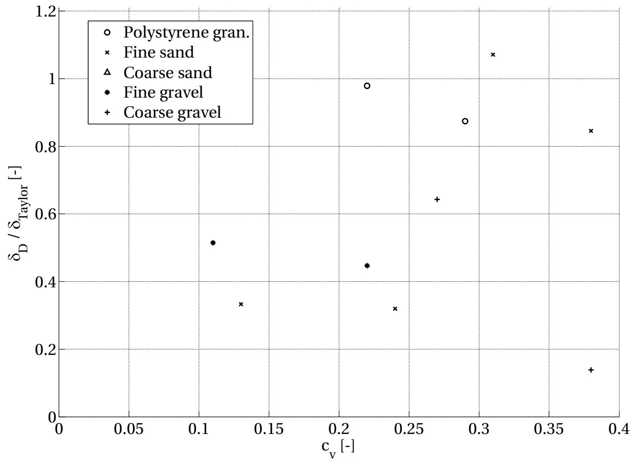

Figure 3.9: Axial dispersion parameter δ_D versus volume fraction of solids c_v.

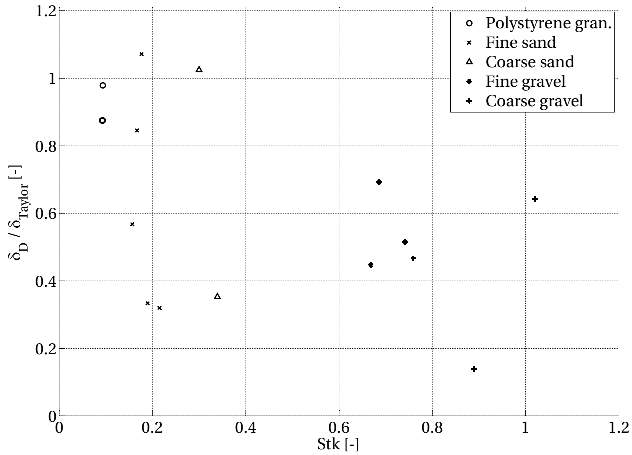

Figure 3.10: Axial dispersion parameter δ_D/δ_{Taylor} versus the Stokes number Stk.

4

EXPERIMENTAL PROOF OF THE FORMATION OF A RISER BLOCKAGE

In deep sea mining, the vertical transport of excavated material from the sea floor to a vessel at the sea surface is a key process. Stationary flow is preferred, and blockage of the riser would terminate the entire operation.

For a blockage to occur there needs to be accumulation of material, the formation of a solid plug, and the plug needs to exert sufficient friction on the riser wall. The formation of a blockage is a complex chain of events, described in detail in this chapter.

The hypothesis presented in this chapter on the formation of plugs and on the conditions for a blockage to occur is checked with the results of a unique experiment. We developed a test setup in which the conditions for riser blockage are enforced. We were able to conduct a reproducible blockage experiment, which shows that the mechanism presented in this chapter is a very accurate description of the blockage process.

To ensure safe operations and high production levels, the transport system needs to be designed for maximum flow assurance. Knowledge of the mechanism and conditions for riser blockage can be used in the design of feeding systems and loading strategies for the vertical transport system.

This chapter has been published in Ocean Engineering **101** (2015) Van Wijk et al. (2015).

4.1. INTRODUCTION

DESPITE the long history of research on vertical hydraulic transport, only few researchers have identified the risk of riser blockage during transport. Shook (1988) identified the risk of slug flow (i.e. the occurrence of intermittent plugs and clear water sections in the riser), but in his work no theory is presented for the actual formation of plugs. Van den Berg and Cooke (2004) describe existing vertical transport systems operated in terrestrial mining sites, and they make notice of possible riser blockage. In their paper a fluidization feeder system is described. The fluidization process causes separation of the individual fractions in the particle size distribution. Upon loading the riser, first the coarse material will enter, followed by more and more finer fractions. This initial condition can result in the formation of a solid plug or even blockage of the riser. Talmon and Van Rhee (2011) identified a similar risk for vertical hydraulic transport in deep sea mining. They describe how batches of fines can overtake batches of coarse material. Numerical simulation of this phenomenon as presented in their paper clearly shows that the volume fraction of solids can reach very large values, up to $c_v \approx 0.65$.

Whether a plug of solids is able to cause riser blockage largely depends on its associated wall friction. In Chapter 5 (Van Wijk et al., 2014b) a model to calculate the wall friction of layered sediment plugs and its experimental validation are discussed. Both the model and the experiments show that the wall friction developed by a layered sediment plug can be as large as several times its submerged weight. The associated friction forces are very well able to exceed the pumping capacity of the system, thus inducing blockage of the riser.

The risk of riser blockage is evident once a plug is present, but the development of these plugs is an unknown phenomenon hardly described in literature. In this chapter we therefore elaborate on the mechanism of plug development by interaction between batches with different transport velocities. We have designed an experiment to demonstrate that the mechanism described in this chapter indeed causes a solid plug to develop, and that these plugs can cause actual blockage of the riser. The results of the experiments are discussed and compared with the theory. It proves that the concept of plug development and riser blockage as presented perfectly matches the experimental results.

4.2. THEORY

4.2.1. FORMATION OF A LAYERED PLUG

THE solids encountered in deep sea mining, e.g. rock cuttings or nodules, show all possible shapes but perfectly spherical. The drag coefficient of irregularly shaped particles is larger than the coefficient of a sphere, see Sections 6.2.1 and 6.2.5. For the main point made in this chapter however, the actual modelling of individual settling velocities is less important than the fact that differently sized particles show different transport velocities. Therefore we will use Equation 6.33 to present the concept of plug formation.

Equation 3.1, with v_s and ϵ_z described with the models presented in Section 6.2.5, can be numerically solved for $c_v(z,t)$ in order to simulate the transport of sediment through a riser. Since the transport velocity v_s consists of a nonlinear term (Equation

6.28) that allows for the formation of shocks, Equation 3.1 should be solved with a numerical scheme that allows for this as well. Here we used the scheme as discussed in 6.3.2.

The evolution of the volume fraction of solids is subject to the constraint of the packing limit of solids. The packing limit is in the range $c_{v,max} \approx 0.6-0.7$, depending on the particle size distribution of the solids in the mixture since fine particles can fill the pores of a matrix of larger particles. We implemented a constant volume fraction of solids $c_{v,max} = 0.6$ as the packing limit in each cell. To enforce conservation of mass while limiting $c_v(z,t)$ to the packing limit, the fluxes in our discretized transport equation are limited with the limiter described in Section 6.3.2.

We will use the transport model to illustrate the main idea of the formation of a solid plug of sediment. Figure 4.1 shows simulations of two batches of solids being transported through a $10\,m$ PVC riser with internal diameter $D = 99.4\,mm$ and friction factor $f_t = 0.01$ at $v_f = 2\,m/s$. The top batch with a length of $0.54\,m$ consists of $d = 12\,mm$ particles with $\rho_s = 2650\,kg/m^3$ at an initial volume fraction of solids $c_v = 0.35$, the bottom batch with a length of $0.54\,m$ consists of $d = 3\,mm$ particles with $\rho_s = 1050\,kg/m^3$ at an initial volume fraction of solids $c_v = 0.25$. The top batch just starts one cell above the bottom batch, giving a space of $0.0389\,m$ (spatial step in the simulation) between the two batches. The graphs show the development of c_v (both the total and the individual batches) versus the riser length L. The results for $t = 1\,s$, $t = 2\,s$, $t = 3\,s$ and $t = 4\,s$ are shown.

The difference between the two simulations is in the axial dispersion process. The first simulation uses $\epsilon_z = 0\,m^2/s$. Upon merging at $t = 1\,s$ it is clearly seen that the local volume fraction increases. The increased volume fraction results in a higher transport velocity of this part of the merging batches, see Equations 6.28 and 6.22. The peak propagates forward while collecting more and more material. In this way a very steep gradient develops at the front of the batch, which resembles a shock wave. After four seconds the volume fraction exceeds $c_v = 0.5$ and the bottom batch is completely mixed with the top batch. The maximum value of c_v obtained in this simulation is $c_v = 0.58$.

The second simulation uses ϵ_z according to Equation 6.39 for the $d = 3\,mm$ particles it uses $\epsilon_z = 0.4\cdot\epsilon_{Taylor}$ for the $d = 12\,mm$ particles, the smallest value being the dominant one. This value is based on the measurements in Chapter 3. The axial dispersion smears out the material which enhances the passage of the first batch. The maximum volume fraction obtained in this simulation is $c_v \approx 0.43$, which is 26 % smaller than the maximum found in simulation 1.

For plug formation to occur, there should be hardly any axial dispersion. In earlier research we were not able to draw firm conclusions on the influence of the volume fraction of solids on the axial dispersion process (Van Wijk et al. (2014a), Chapter 3), but in the hyperconcentrated regime it is very likely that relative particle motions are just minor, and axial dispersion is not significant.

The solids transport velocity $v_s = f(c_v)$ is a monotonically increasing function, which means that when $c_v \rightarrow c_{v,max}$ v_s increases. In the merging zone of the two batches the volume fraction of solids is largest, so the merging zone will accelerate while catching up with the sediment on top. The top section thus gets compressed. When sufficient material is present above the merging zone, the volume fraction can actually reach the

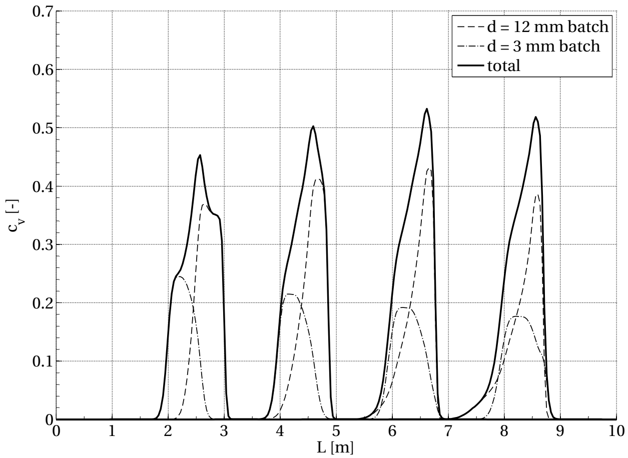

(a) $\epsilon_z = 0\,m^2/s$

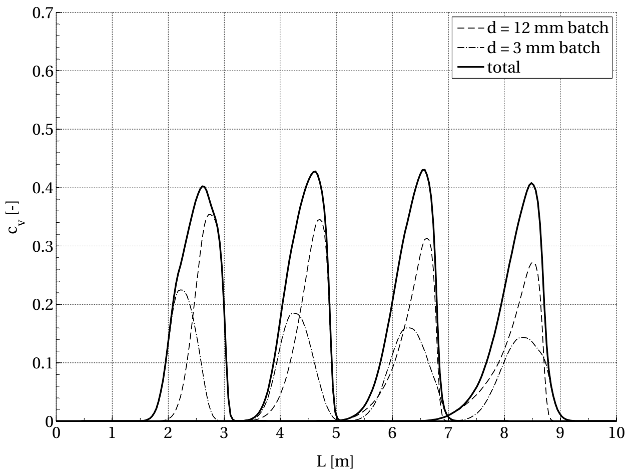

(b) $\epsilon_z = 7.07 \cdot 10^{-3}\,m^2/s$ $(0.4 \cdot \epsilon_{Taylor})$ at $v_f = 2\,m/s$.

Figure 4.1: Simulations of the vertical transport of two batches of solids at $t = 0\,s$, $t = 1\,s$, $t = 2\,s$, $t = 3\,s$ and $t = 4\,s$. Without axial dispersion, the merging zone propagates faster than its surrounding material, thus pushing upward the material and increasing the volume of fraction of solids. With axial dispersion, the material gets more dispersed, hence the increase in the volume fraction of solids is significantly smaller.

packing limit. When the overall volume fraction of solids is sufficiently small for one batch to pass the other, even in the merging zone, the accelerating merging zone will just pass the other particles.

In the case where the top section gets compressed up to the packing limit, the relative particle size determines whether the first batch is able to pass the densely packed second batch. Schaufler et al. (2013) modelled the infiltration of a suspension in densely packed granular material. The infiltration of a suspension of fine material in a stable coarser matrix is determined by the geometry of the particles involved. They use Terzaghi's filter rule (Terzaghi et al., 1996), a design rule for geotechnical filters. In its present form it uses the ratio of d_{50} of the fine fraction (subscript f) and the coarse fraction (subscript c):

$$\frac{d_{50,c}}{d_{50,f}} = 5 \tag{4.1}$$

Equation 4.1 states at which diameter ratio one fraction of solids is just able to infiltrate into a stable matrix of grains. In the case of a flowing matrix (e.g. transport at a large volume fraction of solids), deformation of the matrix might give rise to different ratio's for $d_{50,c}/d_{50,f}$. This however should be the subject of a more detailed study, to which the experiments presented in this chapter hopefully contribute. Once a plug has developed, Equation 4.1 can be used as a criterion for the infiltration of material from one layer into another, which is important in modelling the further increase of the plug volume fraction.

4.2.2. RISER BLOCKAGE

In Section 4.2.1 it was illustrated how a plug could develop from the interaction between two batches of solids, under the condition that axial dispersion is negligible (which is a reasonable assumption in highly concentrated mixtures). In this section we will take the analysis one step further by looking at the conditions under which a plug actually results in blockage of the riser.

For a plug to be able to block the riser, it has to exert significant wall friction. The wall friction of layered plugs is discussed in Chapter 5. The small particles in the bottom layer of the plug partly infiltrate into the top layer, very much like the plug that develops from the merging of two batches shown in Figure 4.1. In this way flow of water through the plug is restricted, and the submerged weight of the top layer now is not carried by the flow of water through the plug, but by the bottom layer. In this way a nonzero axial stress develops, which results in a net effective wall shear stress as given by Equation 5.12.

The average wall shear stress depends on the properties of the plug and the riser, e.g. the angle of internal friction Φ, maximum packing $c_{v,max}$, the grain density ρ_s, plug length L, riser diameter D and the friction coefficient between the riser and the grains μ_k. The wall friction coefficient μ_k (Coulomb model) takes different values for dynamic friction (i.e. sliding of the plug) and static friction (i.e. a blockage). This is an important fact: when dynamic friction is already sufficient to cause a blockage, much larger static friction needs to be overcome to resolve the blockage.

The pressure that a pumping system is able to deliver is limited. When the submerged weight of the solids and the dynamic wall friction exceed the maximum pressure of the pumping system, the system gets blocked and production stops:

$$(\rho_s - \rho_f) \cdot c_v \cdot g \cdot L + \frac{4 \cdot \overline{\tau'_w} \cdot L}{D} \geq \Sigma p_e \big|_{max} \tag{4.2}$$

4.3. EXPERIMENT

4.3.1. TEST SETUP

THE experiments described in this chapter aim at verification of the blockage hypothesis. Two succeeding batches of varying solids were introduced into a scale model riser, in order to identify and quantify the influence of relative particle size, volume fraction of solids and hindered settling on the formation and development of a concentration peak during batch merging. The test setup from Van Wijk et al. (2014b), illustrated in Figure 3.1, was used for these experiments. The hydraulic circuit consists of DN100 PVC pipe and is based at the laboratory of IHC MTI.

The hydraulic circuit contains a riser pipe with a length of 8.7 m center-to-center between the top and bottom horizontal pipes. The riser incorporates (from bottom to top) an electromagnetic flow meter, four conductivity concentration meters (CCM's), a differential pressure (dp) meter and a temperature sensor. The flow meter in the riser is separated from a 90° bend by a $5.5 \cdot D$ straight pipe section to avoid disturbance by turbulence initiated by the bend. The first CCM is separated from the flow meter by a $5 \cdot D$ clear pipe section. The first and second CCM are separated by a 2.2 m section of two clear pipes. The second, third and fourth CCM are separated by a 1.8 m clear pipe section. The riser pipe ends with a $5 \cdot D$ pipe section, followed by a 90° bend. The dp-meter is connected after the first and the fourth CCM, and measures the pressure difference over a 6.0 m section of the riser pipe. The liquid temperature is measured by a temperature sensor fitted at the top of the riser.

The test setup utilizes an inner circuit with two gate valves to prepare and release the solids as two separated batches. The solids are inserted through the particle inlet into the pipe of downward flow in the inner circuit (feeding pipe), where they settle on top of the desired (closed) gate valve. This creates a batch of solids with roughly the packed bed concentration. Ball valves 1 and 3 (Figure 3.1) separate the inner- and the outer circuit during the loading process to prevent water escaping the inner circuit. Before releasing the solids, the centrifugal pump is set to induce the desired initial liquid velocity in the outer circuit, as the batches of solids are stored in the inner circuit. This allows for an accurate reference measurement of the liquid properties. An overpressure release valve is incorporated to equalize the static pressure over the lower gate valve after loading the solids. When the solids are released by opening the gate valves, the water is redirected through the inner circuit by closing the middle ball valve (valve 2, Figure 3.1). The momentum of the initial liquid flow minimizes dilution of the batches when leaving the feeding tube.

4.3.2. EXPERIMENTAL PROGRAM

The experimental program consisted of six experiments, thereby varying the characteristic particle size and relative particle sizes between the two succeeding batches, their density and the liquid velocity. Variations in liquid velocity were required to ensure merging and overtaking would take place within the test section.

These experiments require a significant difference in slip velocity between solids to minimize the merging time span and ensure merging within the riser. The particle diameter is limited to roughly $1/10th$ of the pipe diameter, as particle-wall interactions will otherwise significantly influence the slip velocity. The use of CCM's required the solids material to be non-conductive. The characteristics of the used solids can be found in Table 4.1.

Table 4.1: Properties of the used solids.

Solids type	d_5 $[mm]$	d_{50} $[mm]$	d_{95} $[mm]$	ρ_s $[kg/m^3]$	**Shape**
Medium sand	0.264	0.390	0.497	2650	Sub-rounded
Coarse sand	0.848	1.05	1.24	2650	Sub-rounded
Polystyrene granulate	2.8	2.8	2.8	1050	Cylindric
Medium gravel 1	8.50	9.50	10.50	2650	Angular
Medium gravel 2	12.1	13.5	15.3	2650	Angular

To create a batch, the solids were inserted via a butterfly valve on top of the feeding tube in the inner circuit. The desired gate valve was closed beforehand so that the solids could settle on top of the blade. As the inner circuit consisted of clear PVC pipe, the length of the batches could be determined by filling the pipe to a predefined height. During insertion of the solids, the feeding tube was gently tapped to mitigate entrapped air between the solids and create a consistent maximum packed bed. By weighing the inserted solids before hand, the in-situ concentration could be determined by:

$$c_v = \frac{V_s}{V_m} = \frac{m_s}{\rho_s} \frac{4}{\pi \cdot D^2 \cdot L_0} \tag{4.3}$$

Where c_v = the in-situ batch concentration and L_0 = the initial batch length.
The achieved bed packings were $c_v \approx 0.60 - 0.62$ for medium gravel 1 and 2, $c_v \approx 0.58 - 0.61$ for medium sand, $c_v \approx 0.57 - 0.61$ for coarse sand and $c_v \approx 0.63 - 0.68$ for polystyrene granulate. The higher packing density of the polystyrene is presumably related to the shape of the granulate.

The front batch consisted of coarser solids followed by a second batch of fine solids. A constant initial batch length was maintained among experiments; the front coarse batch had an initial length of 1.50 m and the succeeding fine batch a length of 0.90 m, leaving a 0.75 m space between the batches. The ideal initial liquid velocity for the experiment was determined at 2.0 m/s, because then the initial batch spacing would result in overtaking of the batches halfway the riser section. Due to the construction of the inner circuit however, a start-up effect at the release of the batches was introduced, which caused dilution of a batch when passing the T-piece connecting the inner and outer circuit. The second batch had to be released with a 4 s delay relative to the first, and to mitigate dilution of the first batch within this 4 second interval, the initial liquid velocity in the outer circuit was reduced by partially closing ball valve 3 before release . This reduced the initial liquid velocity to 1.2 – 1.5 m/s while maintaining the required pressure. The lowered initial velocity is a trade-off between the timing of the merging process and keeping initial dilution as small as possible. For future use, modification of the circuit, e.g. enlarging the inner circuit, would solve the problem.

An overview of the initial conditions for the experiments is given in Table 4.2.

Table 4.2: Overview of the experiments' initial conditions, where $v_{f,i}$ denotes the reduced initial liquid velocity and v_f denotes the initial liquid velocity.

Exp.	First batch	Succeeding batch	d_{50c}/d_{50f} [−]	$v_{f,i}$ [m/s]	v_f [m/s]
1	medium gravel 1	polystyrene granulate	3.4	1.5	1.7
2	medium gravel 1	polystyrene granulate	3.4	1.3	2.0
3	medium gravel 2	polystyrene granulate	4.8	1.4	2.0
4	medium gravel 2	medium sand	35	1.4	2.0
5	medium gravel 1	medium sand	24	1.3	2.0
6	medium gravel 1	coarse sand	9	1.2	2.0

4.3.3. EXPERIMENTAL RESULTS

Experiments 1, 2 and 3 all resulted in a blockage of the riser due the merging of both batches. These experiments have very similar initial conditions (i.e. they are nearly identical experiments), pointing out that clogging of the riser is a repeatable process. Clogging of the pipe only occurred in combination with the polystyrene granulate (experiment 1, 2 and 3) and is therefore presented separately from the experiments with sand (experiment 4, 5 and 6).

The graph in Figure 4.2 shows the volume fraction of solids measured at the four CCM's over time. Each graph corresponds with the output of one of the four succeeding CCM's. The output of the CCM's is translated using a linear relation between the electric conductivity and the volume fraction of solids. This is in line with Evans and Shook (1991) for grains having $d > 200\,\mu m$. An improved calibration is proposed in Appendix B, but the current choice does not influence the conclusions drawn from the experiment.

The graph indicates that the front batch (medium gravel 2) passed the first CCM at 1.8 m with a maximum volume fraction of $c_v = 0.3$ and the succeeding batch (polystyrene granulate) with a maximum volume fraction of $c_v = 0.4$. At the moment that both batches pass the second CCM at 4.2 m, the maximum volume fraction is increased to $c_v = 0.6$. At the third CCM at 5.9 m, the volume fraction of solids reaches $c_v = 0.63$, which is roughly the packed bed volume fraction. The merged batch clogged before reaching the fourth CCM, resulting in the constant volume fraction of solids measured at CCM 3 and negligible volume fraction of solids logged by the other three CCM's. Figure 4.3 shows an image of a merged batch inside the riser, made by the top high speed camera. The image shows the front batch, the merging layer and the succeeding batch.

At the moment of clogging, a critical volume fraction of solids is reached at the merging layer after which the liquid velocity drops to $v_f = 0.0-0.1\,m/s$. In the near absence of flow, the surpassed particles settle on top of the clogged merging layer. The settled particles increase the load on the merging layer, which induces a rearrangement of the particles and increases the local volumetric concentration. The effective length of the carrying layer is thereby increased. During this specific experiment, even a second smaller clogged plug was formed from the surpassed solids during the settling process.

Figure 4.4 illustrates the measured differential pressure between $h_1 = 2.0\,m$ and $h_2 =$

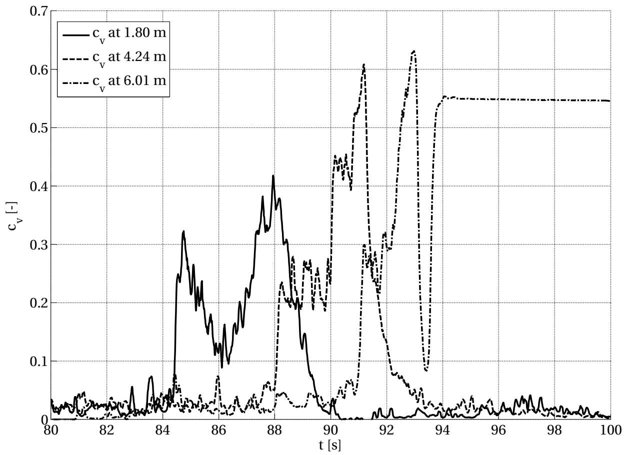

Figure 4.2: Development of the volume fraction of solids' profile during experiment 3.

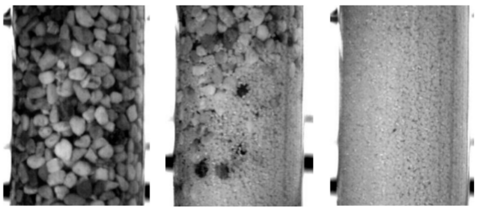

Figure 4.3: Characteristic sections of a merged batch of gravel and polystyrene.

$8.0\,m$. The horizontal striped line represents the static pressure exerted by the inserted particles.

At the instance of clogging (1), a peak pressure of roughly double the submerged weight of the solids was measured. The plug remained in place due to the continuous pressure gradient maintained by the pump (2). Stopping the centrifugal pump removed this pressure gradient (3), leading to erosion of the plug as it layer for layer slowly settled. After a certain length of the plug was eroded, the remainder of the plug slid downwards en bloc. This was a slow and unsteady process. To reset an experiment, the batch had to leave the riser at the top towards the hopper. A differential pressure equal to five times the hydrostatic weight of the solids was required to drive the firmly clogged plug upwards out of the riser (4).

We can check Equation 5.12 with the delivered pump pressure at the onset of the blockage. We will further elaborate on Experiment 3. From our data it is known that at the moment of blockage, the centrifugal pump was operating at $350\,rpm$ with clear water, no flow present. The maximum revolutions of the pump are $950\,rpm$ and the maximum pressure at these revolutions is $132\,kPa$ (pump specifications). Using the

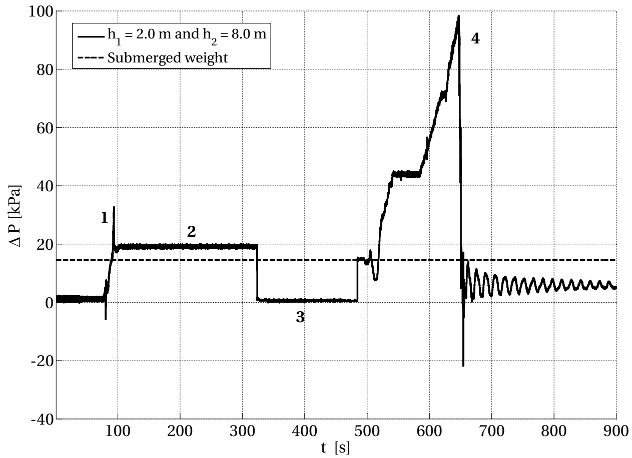

Figure 4.4: Measured differential pressure during experiment 3.

centifugal pump similarity law, we find that the delivered pressure at $350\,rpm$ is $p = (350/950)^2 \cdot 132 \approx 18\,kPa$. Since the polystyrene granulate is neutrally buoyant, it only causes the permeability of the interface to reduce significantly, which induces possible blockage. Only the gravel actually contributes to the grain stresses in the plug, and the observed plug length (of the gravel part, with and without the mixed interface) was approximately $3 \cdot D < L < 5 \cdot D$. When we substitute this length in Equation 5.12 and we use the system properties $D = 0.0994\,m$, $\rho_s = 2650\,kg/m^3$, $\rho_f = 1000\,kg/m^3$, $c_{v,max} = 0.6$, $\mu_k = 0.3$ (estimation from the tilting tube test with PVC and gravel described in Chapter 6) and $\Phi = 30^o$ (estimation based on loosely pouring the gravel on a pile several times, and measuring the angle of the pile), we can calculate the wall friction of the plug $\Delta p_{friction} = 4 \cdot \overline{\tau_w}' \cdot L/D$. For $L = 3 \cdot D$ this yields $\Delta p_{friction} = 8.5\,kPa$ and for $L = 5 \cdot D$ this yields $\Delta p_{friction} = 20.25\,kPa$. In Experiment 3, at the time of blockage all material was present between the connections of the Δp sensor, so the submerged weight of the mixture(including the plug) contributes $\Delta p = (\rho_s - \rho_f) \cdot c_v \cdot g \cdot L = (2650 - 1000) \cdot 9.81 \cdot 0.6 \cdot 1.5 = 14.6 \cdot kPa$ (assuming neutrally buoyant polystyrene granulate). This calculation should be seen as an indication of the order of magnitude of pressure losses, not as a validation of the model. In this case the submerged weight of the batch and wall friction clearly exceed $18\,kPa$, so the conditions for blockage have been fulfilled in this experiment. When $L = 5 \cdot D$ the contribution of wall friction only is already sufficient for the riser to get blocked.

Comparing the measurement data of the experiments with sand instead of polystyrene, certain distinct differences are revealed (see Figure 4.5). There is no significant volume fraction of solids' peak measured during the merging process of the medium gravel and medium sand nor with the coarse sand.

The instance the front and succeeding batch pass the first CCM, volume fractions of

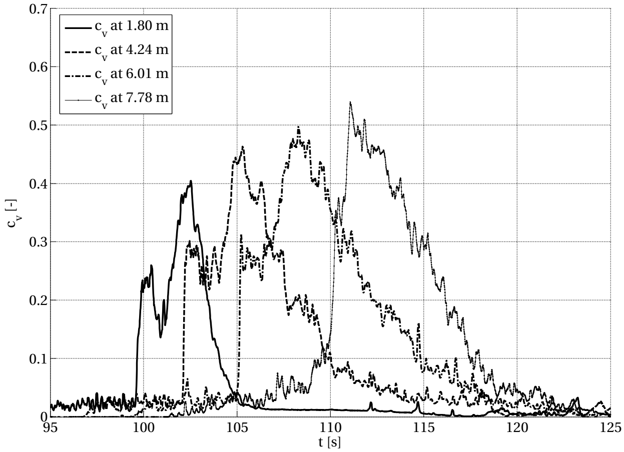

Figure 4.5: Development of the volume fraction of solids' profile during experiment 5.

solids are roughly comparable to the experiments with polystyrene (see Figure 4.2). The medium gravel passes with a maximum volume fraction of solids of $c_v = 0.25$ and the medium sand at $c_v = 0.4$. The maximum volume fraction steadily increases towards the fourth CCM to reach $c_v = 0.55$, without blocking the pipe.

Observations indicated that the sand-water mixture behaved as a heavy liquid flowing through the pores of the gravel, in absence of constant particle-particle contact, and thereby avoiding geometrical blocking. This can be verified by the differential pressure readings seen in Figure 4.6. No pressure peak was logged surpassing that of the submerged weight of the inserted solids.

Visual observations during the experiments revealed a fundamental difference between the merging of a batch of gravel and polystyrene, and the combination of gravel and sand. A batch of polystyrene granulate merging with gravel led in all three cases to clogging of the riser under transport conditions. A batch of sand merging with gravel slowed down the gravel but eventually passed through the pores without clogging the riser.

Table 4.3: Overview of the results.

Experiment	d_{50c}/d_{50f} [−]	**Blockage**
1	3.4	yes
2	3.4	yes
3	4.8	yes
4	35	no
5	24	no
6	9	no

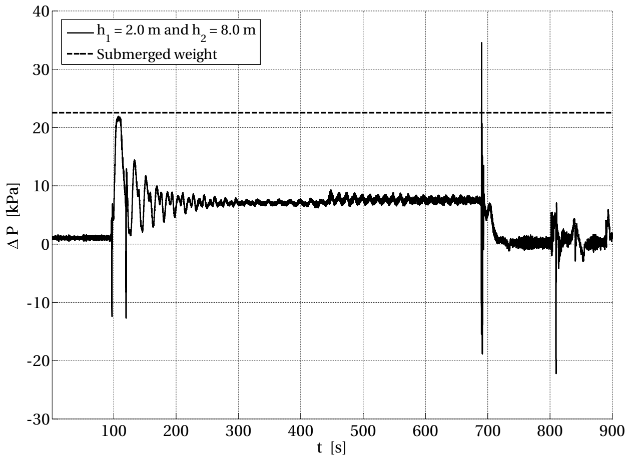

Figure 4.6: Measured differential pressure during experiment 5

The relevant particle diameter ratios presented in Table 4.3 are in line with the filter rule (Equation 4.1). Sound conclusions regarding the influence of relative grain sizes of merging batches on the clogging or passing of solids cannot be drawn yet based on the presented data, but it is considered as an interesting concept for future research.

4.4. CONCLUSIONS AND RECOMMENDATIONS

IN this chapter the concept of riser blockage during vertical hydraulic transport of solids by merging of batches of solids has been introduced. Theory shows that when advection of solids dominates the transport process over axial dispersion, which is the case for typical deep sea mining applications with large solid particles, the merging of two batches of solids induces a strong increase in the volume fraction of solids thus forming a layered plug. These layered plugs have been shown to create much wall friction when the volume fraction of solids gets close to the maximum value. The formation of a layered plug by merging batches of solids is a key process in the onset of riser blockage.

A layered plug can develop by the merging of two or more batches of solids with different transport velocities. With a dedicated set of experiments we were able to show that the formation of a layered plug inside a riser indeed could result in total blockage of the riser. The blockages could only be resolved by providing sufficient excess pump pressure, which is an important consideration for design practice. The pressure needed to overcome can be calculated with the method of Van Wijk et al. (2014b), Chapter 5, as has been verified for one of the experiments.

Not every combination of ’fast’ propagating particles (i.e. small or less dense particles) and ’slow’ propagating particles (i.e. large or dense particles) resulted in blockage of the riser. Whether a combination of solids results in blockage seems to depend on the particle diameter ratio. We used a type of the Terzaghi filter rule as a first approximation for assessment of the risk of blockage for a given combination of solids. The Terzaghi filter rule worked well in our experiments, but future research should elaborate more on this concept.

Having shown plug formation by merging batches, and having shown that these plugs could block a riser, we have prepared the way for a more elaborate series of experiments. It would be very interesting to study the merging of multiple batches (three or more). More batches could potentially result in more densely packed plugs, which can very well be worse than the plugs consisting of only two layers.

For future research it is also recommended to study the influence of the bulk velocity on the merging process. Large bulk velocities combined with sudden blockage of the riser can cause severe water hammer issues, which should be considered in the design of vertical transport systems.

5

WALL FRICTION OF LAYERED SEDIMENT PLUGS

In this chapter an investigation into wall friction of layered sediment plugs is set out. Knowledge about this specific type of plugs and their associated wall friction is necessary for the design of vertical transport systems. First a model is developed, and then an experiment is conducted to verify the model. The model input consists of soil mechanical parameters like the internal angle of friction of the sediment and the coefficient of friction between the sediment material and the riser wall, and geometrical properties such as plug length and riser diameter. By using common values for both the internal angle of friction and the kinematic friction coefficient, the model predicts the outcome of the experiments reasonably well.

This chapter has been published in Ocean Engineering **79** (2014) Van Wijk et al. (2014b).

5.1. INTRODUCTION

IN Chapter 4 we demonstrated how the merging of batches of solids can cause layered plugs, and we have shown that layered plugs can cause riser blockage. For both design of vertical transport systems and the modelling of the internal flow (with the 1DVHT model, that will be introduced in Chapter 6) it is important to know how much wall friction is caused by highly concentrated plugs. The problem of riser blockage and plug formation in general has been addressed by Shook (1988). He mentions the development of large radial stresses and their accompanied wall shear stress in highly concentrated plugs. Grain contacts are the driving mechanism for wall friction, and he refers to stresses in bins as a comparable case. Although plug friction is mentioned, an analysis of the stresses in plugs is not given.

Research into plug flow and wall friction of plugs that are transported vertically is mainly found in the field of pneumatic transport. Gas-solid flows do differ in many ways from hydraulic transport, for the density ratio of the suspended phase and the carrier phase is much larger in pneumatic transport than it is for hydraulic transport, and the particles considered in pneumatic transport are orders of magnitudes smaller than the solids encountered in hydraulic transport of ore. Nevertheless, studying literature on pneumatic transport gives some very interesting references for model development.

5

Borzone and Klinzing (1987) have studied the flow and wall friction of powder plugs in vertical air flows. They used plugs of cohesive coal powder, transported in a vertical tube with $D = 0.025\,m$. They found that the pressure drop over a plug varied linearly with its length. At small gas velocities the plug velocity seemed to be independent of plug length. By analysis of the stress state of a monodisperse plug (i.e. a plug that only contains equally sized particles) they concluded that the only state possible is zero stress over the entire plug length, from which it follows that the submerged weight of the plug is carried entirely by the vertical flow and hence there is a linear relation between pressure drop (equal to the submerged weight) and the plug length.

Niederreiter and Sommer (2004) show the development of a sensor tube, which is used to measure the wall friction between a plug and the tube wall. The tube wall measures the force that is exerted by the passing plug. To interpret the data, they calculate the stress state of a plug with arbitrary boundary conditions for the stress at the top and the bottom. Since the boundary conditions of a plug in motion are unknown a priori, so they state, it is concluded that calculation of wall friction is only possible after measurement of the particle wall stresses.

Rabinovich et al. (2012) investigated the wall friction forces on plugs of coarse particles in a vertical column. Their friction model uses the stress state in a monodisperse plug with a nonzero stress boundary condition at the bottom. The authors wish to use the model in calculations for pneumatic conveying of plugs, so at a first glance the choice for this boundary condition seems incorrect for using the model for a freely suspended monodisperse plug. After all, Borzone and Klinzing (1987) already showed the zero stress state of a similar plug, so no wall friction could be expected at all. When looking at the test setup Rabinovich et al. (2012) used for their experiment, the choice for this nonzero boundary condition becomes clear: the monodisperse plug is directly supported by a permeable piston, which indeed poses a nonzero stress condition at the bottom. The experiment consists of pulling the piston upward through the vertical pipe, and then measuring the force needed for the pull for various pipe materials. No gas is flowing through the plug during the experiment, so the measurement only yields the mechanical friction between the plug particles and the pipe wall for the special case of a plug that is pulled through the pipe by a solid piston rather than by a gas flow.

The cases of powder transport and of coarse monodisperse plugs being lifted on a piston, as discussed above, are not very representative of the wall friction between a plug of coarse sediment and the riser wall, but they are however inspiring: it demonstrates that for a plug to exert friction on a pipe wall, a nonzero stress condition at the bottom of the plug is a necessity.

In Chapter 1 the formation of a layered plug has been identified as a risk for riser blockage. In Chapter 4 this mechanism is discussed in detail. The layered plug that could develop in vertical hydraulic transport systems allows for a nonzero stress state at the interfaces between the different layers (due to differences in permeability between the layers), and thus allows for wall friction to be exerted on the riser wall.

The nonzero stress state between the layers should be explained in more detail. When a layer with permeability κ_1 is put on a layer with permeability κ_2, and when it holds $\kappa_1 > \kappa_2$, then the water flow through the bottom layer is insufficient to support the submerged weight of the top layer, so part of the submerged weight of the top layer has to be carried by the bottom layer. This results in a nonzero stress state at the interface, for the bottom layer partially carries the top layer.

5.2. DEVELOPMENT OF A PLUG FRICTION MODEL FOR A PLUG WITH TWO LAYERS

Development of the layered plug friction model starts with considering a plug with two layers, as depicted in Figure 5.1. The stress state on an incremental slice of this plug is depicted in Fig. 1(b). The total volumetric flow of solids and water through a riser is denoted Q_m. The flow of water is denoted Q_f, the flow of solids Q_s, so the continuity equation for a riser with plug flow is given by:

$$Q_m = Q_f + Q_s \tag{5.1}$$

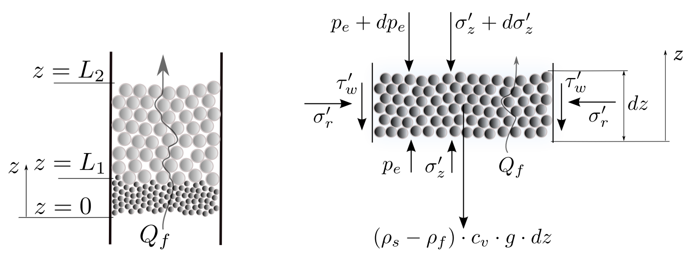

(a) Plug with two layers. (b) Slice with incremental thickness.

Figure 5.1: The plug with two layers that is chosen as the starting point for development of the model (a) and a slice of the layered plug with incremental thickness submerged in water with stresses acting on the slice (b).

For an immovable plug, it holds $Q_s = 0\,m^3/s$ so the total flow equals the flow of water Q_f, which now is a Darcy flow through the immovable plug. In the line of the literature consulted for this chapter, the plug is treated as soil. The first concept from soil mechanics that will be used here is the concept of effective stress. The concept of effective stress allows for using the submerged weight of solids in order to account for the hydrostatic pressure gradient, as depicted in Figure 5.1. The stress thus remaining is the actual stress felt by the grains, σ'_z. The second concept used from soil mechanics, as found in for instance Verruijt (2012), reads:

$$\sigma'_r = \sigma'_z \cdot \frac{1 - \sin\Phi}{1 + \sin\Phi} \tag{5.2}$$

Equation 5.2 shows the relation between radial and axial effective stresses, which is the smallest ratio between the principle stresses in soil, also known as active soil pressure. This relation between radial and axial stresses as a function of the internal angle of friction Φ can also be found in literature on fluidization, see for instance Gidaspow (1994). Typical friction angles of sand and sediment are between 30^o and 40^o, resulting in a ratio between radial and axial effective stresses of typically $0.22 - 0.34$.

5

The effective radial stresses acting on the plug can be related to the wall shear stress τ'_w according to:

$$\tau'_w = \sigma'_r \cdot \mu_k \tag{5.3}$$

The kinematic friction coefficient between a sediment grain and the riser wall is denoted μ_k in Equation 5.3. It does not include any fluid friction, it describes purely mechanical friction.

Since Darcy flow is assumed to govern the fluid flow through the immovable plug the excess pressure p_e in relation to the seeping fluid Q_f has to be clarified. The excess pressure over the plug per unit of plug length equals the excess pressure gradient over the plug, which is given by:

$$\frac{dp_e}{dz} = \frac{Q_f \cdot \mu_f}{\kappa \cdot A} \tag{5.4}$$

In the Darcy equation, κ denotes the total permeability of a layer with (more or less) similar particles, μ_f denotes the dynamic fluid viscosity. The cross sectional area of the plug is dentoted A. The permeability κ can be calculated by using the Carman-Kozeny equation, Verruijt (2012):

$$\kappa = \frac{d^2 \cdot (1 - c_v)^3}{150 \cdot c_v^2} \tag{5.5}$$

In Equation 5.5, d is the particle diameter (d_{50} in this chapter) and c_v the volume fraction of solids.

Equation 5.5 only holds for laminar flow through a porous plug, which is a good approximation when the bottom layer consists of fine material like sand. When the permeability is large, fluid inertia might become important and Forchheimer's equation might be used rather than Darcy's equation. Forchheimer's equation is given by:

$$\frac{dp_e}{dz} = \frac{Q_f \cdot \mu_f}{\kappa \cdot A} + \frac{\rho_f \cdot Q_f^2}{\kappa_I} \tag{5.6}$$

The inertial permeability κ_I is different from the permeability according to Equation 5.5. Equation 5.5 will be used throughout this chapter. By using Equations 5.2 to 5.5, the stress balance on a slice can be composed. This yields the differential equation for the effective axial stress in a layer:

$$\frac{d\sigma'_z}{dz} = -\frac{4 \cdot \mu_k}{D} \cdot \frac{1-\sin\Phi}{1+\sin\Phi} \cdot \sigma'_z - \left(\rho_s - \rho_f\right) \cdot c_v \cdot g + \frac{4 \cdot Q_f \cdot \mu_f}{\kappa \cdot \pi \cdot D^2} \tag{5.7}$$

As stated in Section 5.1, there is a nonzero stress state between the two layers of the plug, so different boundary conditions apply to the bottom and top layer. Equation 5.7 is a first order linear differential equation, for which analytical solutions are available. The axial stress in the bottom layer can be found by applying the following boundary conditions to Equation 5.7: $\sigma'_z(z=0) = 0$ and $\sigma'_z(z=L_1) \neq 0$. In the subscripts, b denotes the bottom layer. The axial stress in the bottom layer ($0 \leq z \leq L_1$) is given by:

$$\begin{aligned}
\sigma'_z &= \frac{b_b}{a_b} + c_b \cdot e^{-a_b \cdot z} \\
a_b &= \frac{4 \cdot \mu_k}{D} \cdot \frac{1-\sin\Phi}{1+\sin\Phi} \\
b_b &= -\left(\rho_s - \rho_f\right) \cdot c_v \cdot g + \frac{4 \cdot Q_f \cdot \mu_f}{\kappa_b \cdot \pi \cdot D^2} \\
c_b &= \frac{-b_b}{a_b}
\end{aligned} \tag{5.8}$$

The axial stress in the top layer can be found by applying the following boundary conditions to Equation 5.7: $\sigma'_z(z=L_1) \neq 0$ and $\sigma'_z(z=L_2) = 0$. Subscript t denotes the top layer. The axial stress in the top layer ($L_1 \leq z \leq L_2$) reads:

$$\begin{aligned}
\sigma'_z &= \frac{b_t}{a_t} + c_t \cdot e^{-a_t \cdot (z-L_1)} \\
a_t &= \frac{4 \cdot \mu_k}{D} \cdot \frac{1-\sin\Phi}{1+\sin\Phi} \\
b_t &= -\left(\rho_s - \rho_f\right) \cdot c_v \cdot g + \frac{4 \cdot Q_f \cdot \mu_f}{\kappa_t \cdot \pi \cdot D^2} \\
c_t &= \frac{-b_t}{a_t} \cdot e^{a_t \cdot (L_2 - L_1)}
\end{aligned} \tag{5.9}$$

The wall shear stress that is exerted on the plug can be found by summation of the contributions of the individual layers. The axial stress σ'_z can be converted to the wall shear stress by multiplication with $\mu_k \cdot (1-\sin\Phi)\,/\,(1+\sin\Phi)$ (i.e. using Equations 5.2 and 5.3), so the wall shear stress is known as a function of z. In order to arrive at an expression for the wall shear stress of an entire plug, Equations 5.8 and 5.9 are averaged over the layer length:

$$\overline{\tau'_w} = \frac{1}{L_2} \cdot \int_0^{L_1} \mu_k \cdot \frac{1-\sin\Phi}{1+\sin\Phi} \cdot \sigma'_{z,b} dz + \frac{1}{L_2} \cdot \int_{L_1}^{L_2} \mu_k \cdot \frac{1-\sin\Phi}{1+\sin\Phi} \cdot \sigma'_{z,t} dz \tag{5.10}$$

In Equation 5.10, the wall shear stress is positive in the negative z -direction. Elaboration of Equation 5.10 yields:

$$\begin{aligned}\overline{\tau'_w} = \quad & \frac{D}{4}\cdot\left[-\left(\rho_s-\rho_f\right)\cdot c_v\cdot g+\frac{4\cdot\mu_f\cdot Q_f}{\kappa_b\pi\cdot D^2}\right]\cdot\ldots \\ & \left[\frac{L_1}{L_2}-\frac{D}{4\cdot\mu_k}\cdot\frac{1+\sin\Phi}{1-\sin\Phi}\cdot\frac{1}{L_2}\cdot\left(1-e^{-\frac{4\cdot\mu_k}{D}\cdot\frac{1-\sin\Phi}{1+\sin\Phi}\cdot L_1}\right)\right]+\ldots \\ & \frac{D}{4}\cdot\left[-\left(\rho_s-\rho_f\right)\cdot c_v\cdot g+\frac{4\cdot\mu_f\cdot Q_f}{\kappa_t\cdot\pi\cdot D^2}\right]\cdot\ldots \\ & \left[\frac{L_2-L_1}{L_2}-\frac{D}{4\cdot\mu_k}\cdot\frac{1+\sin\Phi}{1-\sin\Phi}\cdot\frac{1}{L_2}\cdot\left(1-e^{\frac{4\cdot\mu_k}{D}\cdot\frac{1-\sin\Phi}{1+\sin\Phi}\cdot(L_2-L_1)}\right)\right]\end{aligned} \tag{5.11}$$

Equation 5.11 will be put to the test with a purpose built test setup, described in the next section. Equation 5.11 entirely depends on the plug, flow and riser parameters, so it allows for calculation of frictional losses based on the plug geometry (layer lengths L_1 and (L_2-L_1), volume fraction of solids c_v, permeability κ), particle properties (solids density ρ_s, angle of internal friction Φ), fluid properties (density ρ_f, dynamic viscosity μ_f, flow Q_f) and the riser wall material (in terms of the coefficient of friction μ_k). An example calculation is given in Figure 5.2. The calculation is done for a layered plug with total length L_2, with an infinitely thin bottom layer ($L_1 \to 0$) having an infinitely small permeability, thus blocking the flow through the plug. In this special case, Equation 5.11 can be simplified to:

$$\overline{\tau'_w}=\frac{D}{4}\cdot\left[\left(\rho_s-\rho_f\right)\cdot c_v\cdot g\right]\cdot\left[1-\frac{D}{4\cdot\mu_k}\cdot\frac{1+\sin\Phi}{1-\sin\Phi}\cdot\frac{1}{L_2}\cdot\left(1-e^{\frac{4\cdot\mu_k}{D}\cdot\frac{1-\sin\Phi}{1+\sin\Phi}\cdot L_2}\right)\right] \tag{5.12}$$

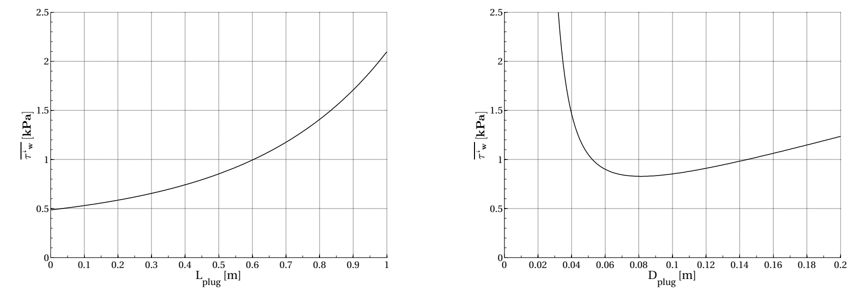

(a) Average wall shear stress versus plug length. (b) Average wall shear stress versus plug diameter.

Figure 5.2: Plug wall shear stress example calculation based on Equation 5.12. Wall shear stress as a function of the plug length (a) and wall shear stress as a function of plug diameter (b). The calculation uses $\rho_s = 2650 kg/m^3$, $\rho_f = 1000 kg/m^3$, $c_v = 0.6$, $\Phi = 35^o$ and $\mu_k = 0.3$.

5.3. THE TEST SETUP AND DESCRIPTION OF EXPERIMENTS

THe test setup is a closed hydraulic circuit (flowloop) consisting of a riser section, a downcomer section and a centrifugal pump. It is situated in the IHC MTI laboratory in Kinderdijk. Both the riser and the downcomer are built of transparent PVC so observation of the processes is possible. The internal diameter of the system is $D = 99.4\,mm$. At the bottom of the riser section, a knife gate valve is installed. The basic principle of the experiment is as follows: (1) A batch of sediment is put on the closed knife gate valve, (2) the centrifugal pump is started so pressure builds up under the valve. There is no flow present yet, and (3) the valve is opened, so there is a large pressure difference over the plug. The water starts seeping through the plug. The plug is 'launched' and sets off through the flowloop. Figure 5.3 shows the layout of the test setup including measurement equipment.

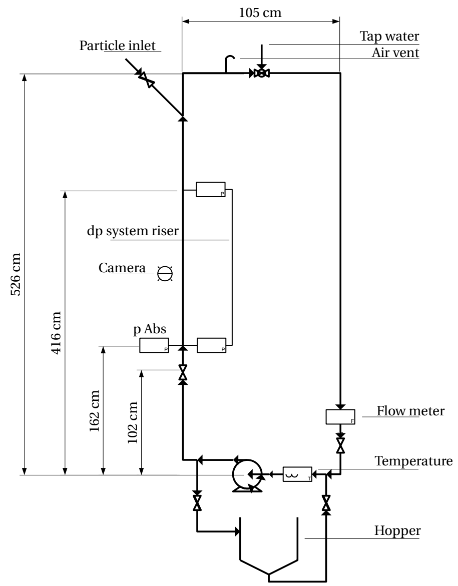

Figure 5.3: Schematic representation of the test setup. The dP measurement system starts at the same height as the absolute pressure sensor, and spans $2.54\,m$.

The test setup is equipped with a flow meter. The impulse tubes of the differential pressure sensor are connected to the riser section at $0.60\,m$ and $3.14\,m$ above the knife gate valve. The implication of this choice is that at the onset of an experiment, the differential pressure of the hydrostatic water column will be measured together with the submerged weight of a part ($0.40\,m$) of the sediment plug, which extents $1.00\,m$ above the knife gate valve. Upon opening the gate valve, the plug will get into motion driven by the pressure that has built up in front of the plug. The pressure that is forcing the plug is registered by the bottom impulse tube connection as soon as the plug passes. The plug is monitored with a high speed camera mounted just above the differential pressure section.

Two types of sediment have been used in this experiment: coarse sand and gravel. The particle properties are summarized in Table 5.1. Particle size distributions as obtained from the supplier are given in Figure 3.2 (coarse sand and fine gravel).

Table 5.1: Sediment properties. The solid's density and volume fraction of solids are assumptions. The permeability is calculated with Equation 5.5.

Grain type	d_{50} $[mm]$	ρ_s $[kg/m^3]$	κ $[m^2]$	c_v $[-]$
Coarse sand	1.05	2650	$1.2 \cdot 10^{-9}$	0.6
Gravel	6.34	2650	$5.0 \cdot 10^{-8}$	0.6

These two types of sediments have been applied in different initial layering configurations. The configurations are summarized in Table 5.2. For every experiment, the riser has been filled with sediment up to 100 cm above the knife gate valve. This means that the first differential pressure impulse tube connection can be found at $0.40\,m$ below the top of the sediment plug. The initial concentration of the plug is estimated as $c_v = 0.6$, which is the value of a normally packed bed of sediment particles. Before each test, the pump speed is chosen such that the equilibrium flow without any suspended sediment will be approximately $15\,l/s$.

Table 5.2: Overview of the experiments.

Experiment	Bottom layer grain type	Top layer grain type	Thickness bottom layer $[m]$	Thickness top layer $[m]$
1	Gravel	Sand	0.5	0.5
2	Sand	Gravel	0.25	0.75
3	Sand	Gravel	0.5	0.5
4	Sand	Gravel	0.75	0.25

5.4. RESULTS AND DISCUSSION

THe differential pressure measurement shows the total pressure needed to lift the plug at the point of incipient motion. This pressure consists of the submerged weight of the plug, the action of wall friction and acceleration of the plug. To isolate the contribution of wall friction we have to know what the contribution of the acceleration term would be. Since the distance $\Delta L_{sensors}$ between the two differential pressure sensors is known, the pressure required to accelerate the plug can be computed. To this end, the time Δt_{plug} needed for propagation from the lower to the upper differential pressure impulse tube connection is recorded. The timespan can be estimated by looking at the differential pressure measurement in time: time counting starts when the valve is opened and the pressure increases and time counting ends when the dP system shows the hydrostatic pressure again. The mass of the plug is estimated as its submerged weight. The pressure due to acceleration (assuming linear acceleration) can be calculated with:

$$\Delta p_{acc} = \frac{m_{plug}}{A} \cdot \frac{d^2 z}{dt^2} = \frac{m_{plug}}{A} \cdot \frac{2 \cdot \Delta L_{sensors}}{\Delta t_{plug}^2} \tag{5.13}$$

For a typical test with a batch of $L_{plug} = 1\,m$ it holds $m_{plug} = 7.78\,kg$, $A = 7.85 \cdot 10^{-3}\,m^2$ and $\Delta L_{sensors} = 2.54\,m + 0.60\,m$ ($2.54\,m$ between the sensors, and the bottom of the plug starts $0.60\,m$ below the bottom impulse tube connection). The first step in isolating the wall shear stress is subtracting the submerged weight of the plug from the pressure measurement. The second step is subtracting the acceleration pressure drop of Equation 5.13, and converting the resulting pressure to wall shear stress:

$$\overline{\tau'_w} = \left[\Delta p_{measured} - \left(\rho_s - \rho_f\right) \cdot c_v \cdot g \cdot L_2 - \Delta p_{acc}\right] \cdot \frac{D}{4 \cdot (L_2 - L_1)} \tag{5.14}$$

Note that this conversion corrects the measurement for the weight of the entire plug, but it then uses the top layer only to attribute the wall shear stress to. This choice will be made clear in the remainder of this section.

The first experiment comprises the launch of a plug with sand on top of gravel. Figure 5.4 shows the pressure recording of the first run of Experiment 1. Figure 5.5 (a) shows the wall shear stress of the first run of Experiment 1, Figure 5.5 (b) shows the second run and Figure 5.5 (c) shows the third run. The wall shear stresses are based on Equation 5.14. As a reference in Figure 5.4, the horizontal line indicates the submerged weight of the plug. We are interested in the wall shear stress peak just at the moment that the flow rapidly increases, for this is the moment in time that the plug starts to move and both the static weight of the submerged plug and the wall friction are overcome by the pressure difference. From Figures 5.5 it is clear that the peak pressure at the launching of the plug is just slightly larger than the submerged weight and the pressure needed for acceleration. The average wall shear stress found in these experiments is $\overline{\tau'_w} \approx 0.045\, kPa$. The pressure difference needed for acceleration of the plugs was found to be $\Delta p_{acc} \approx 7.4 \cdot 10^{-2}\, kPa$, or 8% of $\overline{\tau'_w}$ when using the conversion with Equation 5.14. This amount is small but significant.

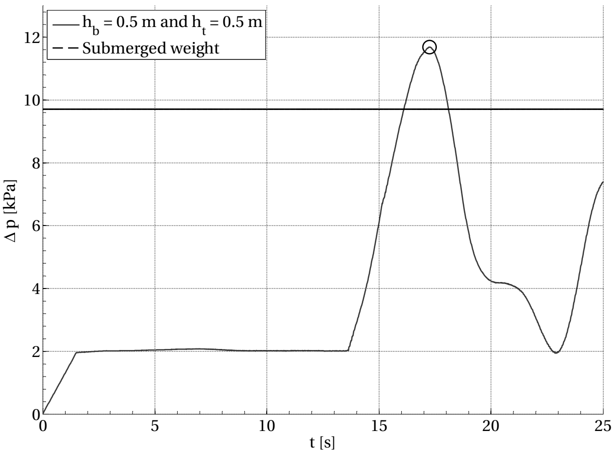

Figure 5.4: Differential pressure recording of the layered plug with sand on top of gravel, Experiment 1. The pressure needed to launch the plug (circle) is about 1.2 times the submerged weight of the plug.

Figure 5.6 shows the recording of Experiment 3. It becomes clear immediately that the peak pressure encountered in this configuration exceeds the pressure due to the submerged weight of the plug by far; the maximum peak found is almost 2.5 times the submerged weight, while in Figure 5.4 only a factor of 1.18 was found. Figure 5.7 (a) shows

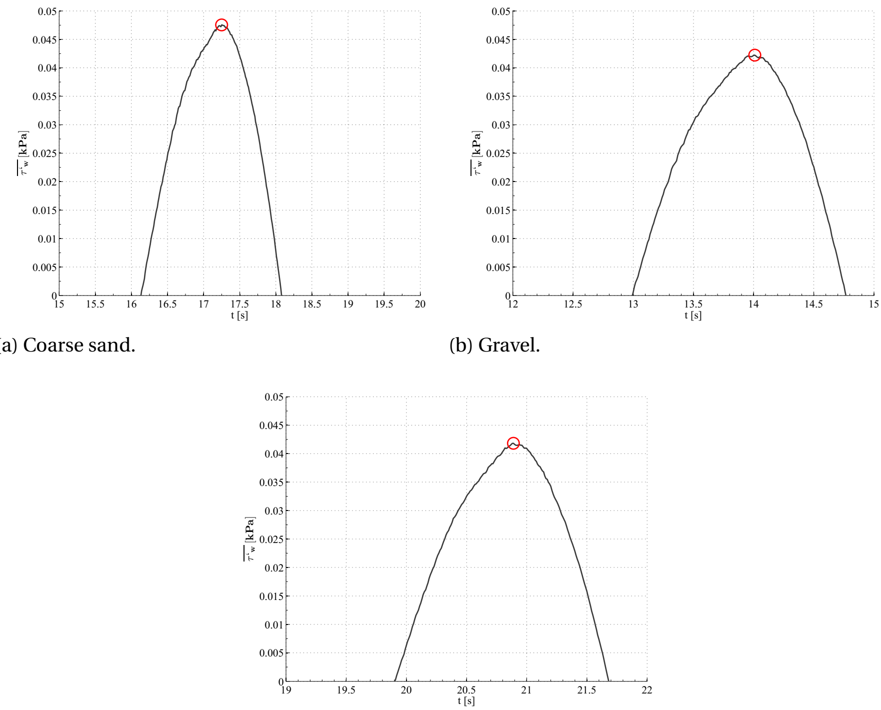

(a) Coarse sand.

(b) Gravel.

(c) Gravel.

Figure 5.5: Measured wall shear stresses (Equation 5.14) for three runs of Experiment 1: first run (a), second run (b) and third run (c). The maximum stress at the point of incipient motion is shown in the circle.

the wall shear stress of Experiment 2 according to Equation 5.14 (14). Figure 5.7 (b) shows the wall shear stress of Experiment 3 and Figure 5.7 (c) shows the results of Experiment 4 (please refer to Table 5.2). In all three experiments, the wall shear stress is significantly larger than the wall shear stresses encountered in Experiment 1. The pressure needed for acceleration of the plugs was found to be $\Delta p_{acc} \approx 3.89 \cdot 10^{-1}\, kPa$ (or equivalently 2.7% of $\overline{\tau'_w}$) for Experiment 2, $\Delta p_{acc} \approx 9.96 \cdot 10^{-3}\, kPa$ (or equivalently 0.06% of $\overline{\tau'_w}$) for Experiment 3 and $\Delta p_{acc} \approx 1.29 \cdot 10^{-7}\, kPa$ (or equivalently 0.0003% of $\overline{\tau'_w}$) for Experiment 4. The contribution of acceleration to the pressure drop is small for Experiment 2 and negligible for Experiments 3 and 4.

The results of Experiments 2 to 4 can be compared with the model prediction of Equation 5.11. To this end, an important assumption has been made. Based on visual observation it can be stated that the flow of water through the plug with gravel on top of sand is negligible, but sufficient to support the bottom layer (the layer does not settle after opening the valve, but stays in place). This assumption has two implications. The first one is, that the Darcy term of the top layer in Equation 5.11 will be approximately zero (i.e. a very small flow with a relatively large permeability). The second implication is that the submerged weight of the bottom layer is supported by the Darcy flow through

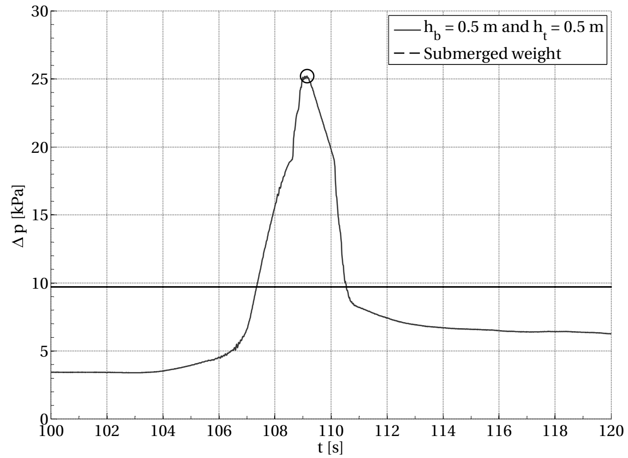

Figure 5.6: Differential pressure recording of the layered plug with gravel on top of sand, Experiment 3. The pressure needed to launch the plug (in the circle) is about 2.5 times the submerged weight of the plug.

the bottom layer. There will be a net effective axial stress due to a somewhat larger Darcy force on the bottom layer compared to the gravity force, but the net result will be very small compared to the contribution of the weight of the top layer. For the bottom layer the gravity and Darcy term effectively cancel each other out. To arrive at the model predictions using the above assumptions, the following values of the plug, fluid and sediment parameters are used: solids density $\rho_s = 2650\,kg/m^3$, angle of internal friction $\Phi = 35^o$, fluid density $\rho_f = 1000\,kg/m^3$, $c_v = 0.6$, flow $Q_f = 0\,m^3/s$ and $\mu_k = 0.3$. The riser diameter used is $D = 0.1\,m$. As a consequence of the assumptions stated above, the thickness of the top layer is used as the length of the plug in Equations 5.13 and 5.14. The resulting wall shear stresses are compared with the model predictions in Table 5.3.

As can be seen in Table 5.3, the orders of magnitude are predicted reasonably well, especially for Experiment 4 with the largest coarse material top layer. The model also gives a reasonable estimate for Experiment 3, but the wall shear stress as measured in Experiment 2 is underestimated. It has to be noted in this respect that the choice of Φ and μ_k is based on experience with common numbers for sediments, but these parameters can be tuned per experiment to exactly fit the measurement. This however would impose only the appearance of correctness rather than showing that based on reasonable numbers, the model gives a satisfying output.

Table 5.3: Measurements and model predictions of the wall shear stress of layered plugs with gravel on top of sand (Experiments 2 to 4).

Thickness bottom layer $[m]$	**Thickness top layer** $[m]$	**Measurement** τ_w $[kPa]$	**Prediction** τ_w $[kPa]$
0.25	0.75	1.44	1.28
0.5	0.5	0.77	0.85
0.75	0.25	1.28	0.62

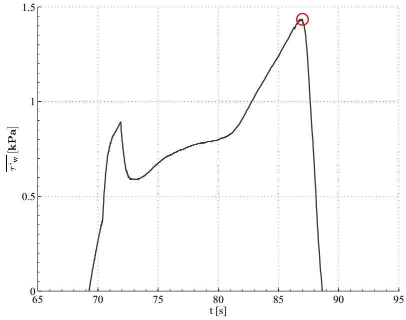

(a) Coarse sand.

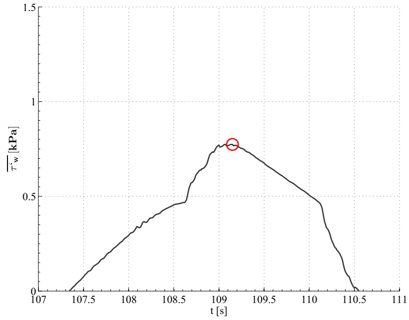

(b) Gravel.

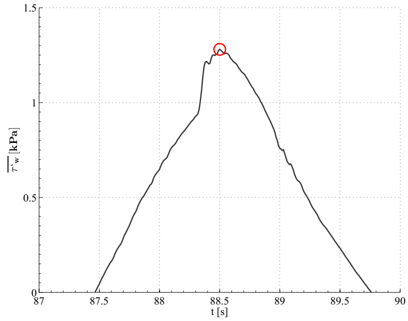

(c) Gravel.

Figure 5.7: Measured wall shear stresses (Equation 5.14) for Experiment 2 (a), Experiment 3 (b) and Experiment 4(c). The maximum stress at the point of incipient motion is shown in the circle.

5

5.5. EVALUATION

THE experiments have shown that the model predicts the wall friction of sediment plugs reasonably well when choosing realistic values for the soil mechanical parameters, but the set of data is all but complete. The water flow through the plug for instance is unclear, because the small amounts of seeping water were hardly registered by the flow meter. For relatively large top layers it seems a reasonable assumption to neglect the contribution of the bottom layer to the wall shear stress, but given the underestimation of the stress for Experiment 2 (with a large bottom layer), it might be argued that neglecting the bottom layer is indeed always valid. Model predictions including the contribution of the bottom layer suggest the need for accurate flow measurement and simultaneous recording of plug motion, flow and pressure.

For future research it is recommended to improve the test setup by inserting a more sensitive flow meter. Furthermore it is recommended to situate the connection of the bottom impulse tube of the differential pressure sensor just below the valve instead of just above the valve. By doing so, even more accurate pressure recordings over the entire plug can be taken. Synchronized high speed camera recordings would make a test complete.

A future series of experiments should firstly include more experiments, because the data set thus obtained is rather limited. Second, one can think of variation in soil mechanical parameters like solids density, different permeability ratios of the different layers, different angles of internal friction and different types of riser material. As a third option it would be good to include even more layers.

In this chapter it has been shown that layered sediment plugs that can develop from the merging of individual batches (see Chapter 4) are expected to exert much wall friction, which is a necessary condition for riser blockage.

Shortly after publication of our paper (Van Wijk et al., 2014b), a plug friction model for pneumatic conveying in pipes with orientations between 0^o and 90^o was published by Shaul and Kalman (2014). Their work contains the derivation of a plug friction model, in which the boundary conditions are varied depending on the pipeline orientation, and it contains experimental validation of the model. An important aspect of their model for vertical plugs is the application of an external force to the plug (as a boundary condition) which comes from the insert which is present in their experimental device, similar to the device of Rabinovich et al. (2012). Without explicitly assuming this external force, their friction model would yield zero friction. In our work we have identified the different permeability of the layers in the plug as the source of a net axial stress.

5.6. CONCLUSIONS

IN this chapter an experiment has been set up in order to test if a layered plug with a relatively impermeable bottom layer, a configuration expected to occur due to batch overtaking processes in long vertical risers, would yield significant wall friction compared to an ordinary monodisperse plug that hardly shows any friction.

An analytical model of the wall shear stress averaged over the plug length has been developed based on a stress analysis of a layered plug with a nonzero boundary condition at the interface between two layers, a case that is expected to match the situation of a layered plug with relatively impermeable bottom layer. According to this model, significant wall friction would occur, exceeding the pressure due to the submerged weight of the plug by far.

The experiment that was described in this chapter showed that the layered plug with a relatively impermeable bottom layer indeed shows much more wall friction than a plug with the reversed layering. In the case of coarse sediments (gravel) on top of sand, pressure peaks at the launch of a plug were measured as much as four times the submerged weight per unit area of riser, while in the case of sand on top of gravel the pressure peaks only exceeded the submerged weight by 20% at maximum. When corrected for the pressure needed for acceleration, the case of gravel on top of sand yields wall friction in the order of $1\,kPa$, while for the case with sand on top of gravel a wall shear stress of $0.045\,kPa$ was measured. Three configurations with relatively impermeable bottom layers have been tested in the experiment, all configurations having two layers adding up to a plug with a length of $1\,m$. The analytical model was able to predict the correct order of magnitude of the wall friction, but there remains uncertainty in the choice of the soil mechanical parameters Φ and μ_k. These parameters can be chosen such that the model perfectly fits every single experiment, but by choosing realistic and common values for sediments, we have demonstrated that the model gives a satisfying output. Especially for the case with a large top layer of coarse material (i.e. large wall friction) the model replicates the outcome of the experiments reasonably well.

6

1DVHT: A ONE-DIMENSIONAL MODEL FOR VERTICAL HYDRAULIC TRANSPORT

In order to model the long distance vertical hydraulic transport of large particles, all scales from the smallest eddy to the riser length should be taken into account, either by computation or by modeling. The mixture flow in the riser is computed by solving the conservation of mass and momentum equations. The transport of solids is computed by solving the advection-diffusion equation for the individual fractions using a drift-flux method. The set of equations is closed with empirical models for wall friction, axial dispersion and particle slip velocities.

6.1. MODEL OVERVIEW

THE 1DVHT model computes the propagation of a mixture of solids and water in space and time through a vertical pipeline. The input is given by the geometry of the transport system, a set of differential pressure sources (representing booster stations) which induce the mixture flow and by the volume fraction of solids of K fractions and their properties at the inlet of the riser. A PID controller is implemented to control the flow by adjusting the booster station pressure between zero and the predefined maximum pump pressure. The model can be used for simulation of transient processes, for instance the start-up of the transport process, (emergency) shutdowns, pump failure and riser blockage.

The output of the model is the distribution of the volume fraction of solids of each fraction $c_{v,k}(z,t)$, the total volume fraction of solids (or equivalently $\rho_m(z,t)$), the mixture bulk velocity $\overline{v_m}(t)$, the transport velocities of the individual fractions $v_{s,k}(z,t)$, the fluid velocity $v_f(z,t)$, the wall friction of the mixture $\tau_m(z,t)$ (and its associated fluid and solid contributions $\tau_f(z,t)$ and $\tau_s(z,t)$) and the delivered differential pump pressure $p_e(z,t)$.

6.2. MODEL EQUATIONS

6.2.1. THE MIXTURE

6

THE fluid phase consists of seawater with a density ρ_f and dynamic viscosity μ_f, both are functions of water temperature and salinity (Sharqawy et al., 2009). The temperature of the ocean is a function of the water depth. The surface temperatures strongly vary from location to location and with changing seasons, but the water temperature at depths $> 1000\,m$ is much more constant, around $3^oC < T < 5^oC$ (NOAA, 2015). An exception to this is the water temperature around active hydrothermal vents. Figure 6.1 shows an example of the temperature and salinity profiles as measured in the Clarion Clipperton Zone (a potential site for mining manganese nodules).

In the 1DVHT model, a constant water temperature and salinity are assumed, from which the density and viscosity are derived using Sharqawy et al. (2009). For a riser with $L = 5000\,m$ and $D = 0.4\,m$, transporting a mixture (water and solids) with $\overline{v_m} = 4\,m/s$ and $\rho_m = 1250\,kg/m^3$, the irreversible losses can be estimated using $\Delta p = f_t \cdot L/D \cdot 1/2 \cdot \rho_m \cdot \overline{v_m}^2$ (equivalent liquid model). If we take the friction factor very conservative, say $f_t = 0.02$ which is about twice the value for water-steel friction, we get an irreversible loss of $\Delta p = 2.5\,MPa$. The energy associated with this loss is absorbed by the mixture as heat. We assume the mixture has the same specific heat as sea water, e.g. $c_p \approx 4\,kJ/kgK$ (Sharqawy et al., 2009). The mixture has a mass of $m = \rho_m \cdot \pi/4 \cdot D^2 \cdot L = 7.85 \cdot 10^5\,kg$. The transport time is $t = L/v_m = 1250\,s$. The energy added by wall friction then increases the temperature of the mixture by $\Delta T = \pi/4 \cdot D^2 \cdot \overline{v_m} \cdot \Delta p \cdot t/(c_p \cdot m) = 0.5^oC$. The effect of this temperature increase on the water density is negligible, so assuming a constant water density is valid.

The density of the solid fraction is denoted ρ_s. In literature one often finds the solid particles being idealized to a sphere. Obviously real shapes of the solids in this study can be very different. There are several ways to account for the geometry of non spherical particles (Sumner, 2000). The first approach is the equivalent surface diameter $d_s =$

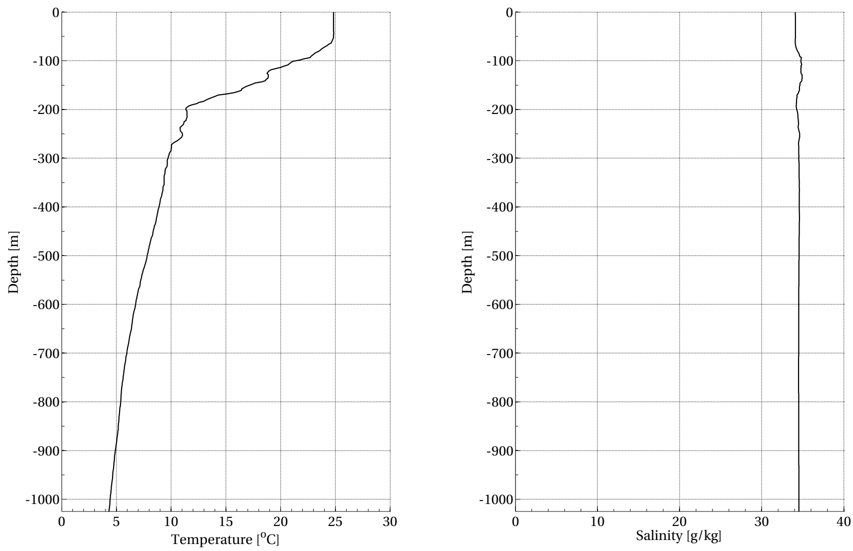

(a) Seawater temperature profile.

(b) Seawater salinity profile.

Figure 6.1: Temperature and salinity profiles taken at 13^o latitude and -153^o longitude in the Clarion Clipperton Zone (NOAA, 2015).

$\sqrt{4 \cdot A_s/\pi}$, i.e. the diameter of a sphere having the same surface area A_s as the particle. Finding A_s might be troublesome. One can find the diameter of a sphere having the same volume as the particle in a similar way. The equivalent volume diameter d_v is given by $d_v = \sqrt[3]{6 \cdot V_p/\pi}$.

A general system for classification of particle shapes can be found in the field of sedimentology (Norbury, 2010). This classification uses angularity and sphericity. The angularity is found by visual observation, i.e. sediments are well rounded while blast rock or cuttings are very angular. The sphericity ϕ is calculated as $\phi = \pi \cdot d_v^2 / A_s$. Typical values for the sphericity are given by Kunii and Levenspiel (1991), see Table 6.1.

Next to particle shape, particle size plays an important role in hydraulic transport. A sample of solids taken from the field contains particles with different sizes. The particle size distribution (PSD) of a sample gives the weight distribution of the different size classes in the sample. Figure 6.2 shows a particle size distribution with weight fractions w_k and the cumulative particle size distribution. A PSD obtained by sieving typically consists of $K = 10$ fractions. The median particle diameter is d_{50}, which is the diameter of the fraction for which half of the weight is smaller and half of the weight is larger in size. The mean diameter d_m is defined by:

Table 6.1: Sphericity of different particles according to Kunii and Levenspiel (1991).

Particle shape	**Sphericity** [−]
Sphere	1.0
Cube	0.81
Disk, $h = d/3$	0.76
Disk, $h = d/6$	0.60
Disk, $h = d/10$	0.47
Broken solids	0.67
Crushed, jagged glass	0.65
Round sand	0.86
Sharp sand	0.66

$$d_m = \frac{\sum_{k=1}^{K} d_k \cdot w_k}{\sum_{k=1}^{K} w_k} \tag{6.1}$$

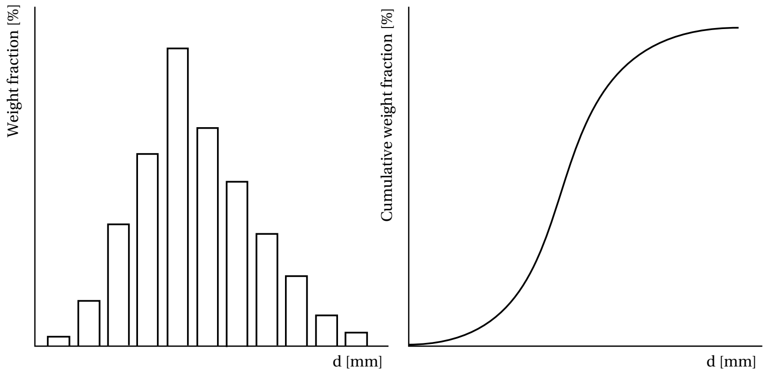

Figure 6.2: Particle size distribution with discrete fractions (left) and the cumulative particle size distribution (right).

The transport of suspended solids or dense granular flows can be approximated as a continuum (Jop et al., 2006). The mixture consists of a carrier liquid (e.g. seawater) and solids. The volume fraction of solids is denoted c_v, the volume fraction of the carrier liquid is $1 - c_v$. The solids phase consists of K size classes, with each class having a mean particle diameter d_k, density $\rho_{s,k}$ and relative volume fraction $c_{v,k}$. The total volume fraction of solids is given by:

$$c_v = \sum_{k=1}^{K} c_{v,k} \tag{6.2}$$

The mixture density follows from:

$$\rho_m = \left(1 - \sum_{k=1}^{K} c_{v,k}\right) \cdot \rho_f + \sum_{k=1}^{K} c_{v,k} \cdot \rho_{s,k} \tag{6.3}$$

Particles enountered in the field always leave pore space when packed together. Equally sized spheres for instance have a theoretical maximum volume fraction of $c_v \approx 0.74$, for irregularly shaped sediments with a narrow particle size distribution the maximum volume fraction of solids is closer to $c_v \approx 0.6$.

Empty pore spaces can be filled with smaller particles, thus increasing the volume fraction of solids. The maximum packing of polydisperse mixtures with two or more fractions has been investigated by several researchers. Note that upon increasing c_v, the behaviour of the mixture gradually changes from fluid-like to soil-like. In the aggregates industry, the well-gradedness is calculated with the Fuller curve, which is a theoretical particle size distribution which results in a high maximum packing (Fuller and Thompson, 1906). For sand-clay mixtures, Winterwerp and Van Kesteren (2004) report that the maximum packing corresponds well with the Fuller grain size distribution. The inverse problem is determining the theoretical maximum packing from a given particle size distribution, as investigated by Furnas (1931). His model has been generalized by Liu and Ha (2002).

The question whether particles with a given size are able to penetrate in the pores of a matrix of larger particles has got much attention in the field of geo-engineering. In Terzaghi et al. (1996), criteria can be found, which take the form $d_{coarse}/d_{fine} = constant$.

While a wide particle size distribution allows for larger volume fractions by filling the pores of the coarse matrix with finer material, the fact that the solids are contained within the walls of a pipeline or riser decreases the maximum volume fraction of solids. In the center of the riser the maximum volume fraction can be obtained but at the perimeter the volume fraction is smaller due to geometrical constraints (Chang and Acrivos, 1987; Talmon, 2008). According to Chang and Acrivos (1987), the volume fraction of solids in the outer perimeter (i.e. the region within one particle diameter from the wall) is calculated with:

$$\frac{c_{v,b}}{c_v} = \frac{d^2}{4} \cdot \left(\frac{3}{4} - \frac{d^2}{16}\right) \tag{6.4}$$

In Equation 6.4, c_v is the volume fraction of solids in the center and $c_{v,b}$ is the volume fraction of solids within a distance of one particle diameter from the wall. A small experiment at the MTI Holland laboratory, in which the maximum packing of glass spheres in two different tubes has been investigated, resulted in the data as shown in Figure 6.3. Equation 6.4 underestimates the maximum volume fraction of solids slightly, which can be attributed to the fact that Equation 6.4 only takes into account the two dimensional plane, i.e. one layer of particles, while a second layer placed upon the first layer partially overlaps the first layer, so the volume fraction in a random plane is larger.

The maximum allowable volume fraction of solids is an input parameter for the model. Based on the measurements in Figure 6.3, a reasonable figure is $c_{v,max} = 0.6$.

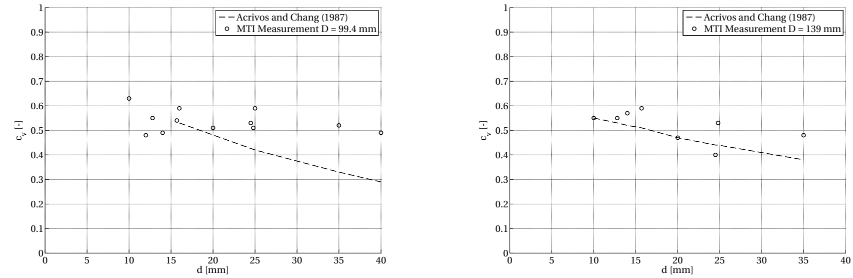

(a) $D = 99.4\,mm$ pipe. (b) $D = 139\,mm$ pipe.

Figure 6.3: Maximum volume fraction of solids in two different pipe sections. Due to geometrical constraints, the maximum volume fraction of solids in a pipe is smaller than the theoretical value for the maximum packing.

6.2.2. Conservation equations and transport of solids

The mixture is treated as a single fluid with density ρ_m, velocity v_m and pressure field p. The flow is incompressible, but density changes over time: $\rho_m = \rho_m(t)$ depending on the presence of particles. Following Prosperetti and Tryggvason (2009); Hiltunen et al. (2009), the continuity equation of the mixture for the z-direction (vertical direction, positive upward) is given by:

$$\frac{\partial \rho_m}{\partial t} + \frac{\partial \left(\rho_m \cdot v_m\right)}{\partial z} = 0 \tag{6.5}$$

Conservation of momentum in z-direction is given by:

$$\frac{\partial \left(\rho_m \cdot v_m\right)}{\partial t} + \frac{\partial \left(\rho_m \cdot v_m^2\right)}{\partial z} = \frac{\partial p}{\partial z} - \frac{4 \cdot \tau_m}{D} - \rho_m \cdot g + \sum \frac{\partial p_e}{\partial z} - \ldots \tag{6.6}$$
$$\frac{\partial}{\partial z}\left[(1-c_v)\cdot \rho_f \cdot \left(v_m - v_f\right)^2 + \sum_{k=1}^{K} c_{v,k} \cdot \rho_{s,k} \cdot \left(v_m - v_{s,k}\right)^2\right]$$

Equations 6.5 and 6.6 need closure relations for τ_m and $v_{s,k}$. All viscous stresses are governed in one friction term τ_m. The term $\sum \partial p_e / \partial z$ denotes the total amount of external pressure gradient, i.e. the action of centrifugal pump booster stations. Because there is a considerable velocity difference between the solid fractions and the carrier fluid, Manninen and Taivassalo (1996) suggest that the forces due to this slip velocity have to be included in the momentum equation, which is the last term on the right hand side of Equation 6.6.

Solving Equations 6.5 and 6.6 results in the velocity and pressure field in the riser. Since a one dimensional continuum approach is adopted, transport of the suspended solid fractions can be described with the advection-diffusion equation:

$$\frac{\partial c_v}{\partial t} + \frac{(\partial c_v \cdot v_s)}{\partial z} = \frac{\partial}{\partial z} \cdot \left(\epsilon_z \cdot \frac{\partial c_v}{\partial z}\right) \tag{6.7}$$

The advection term describes the transport of particles due to the actual particle velocities, the diffusive part describes the transport by means of axial dispersion. Axial dispersion models the effects of a non uniform radial velocity profile and turbulent mixing. Equation 6.7 needs closure relations for both the solid's transport velocity v_s and axial dispersion coefficient ϵ_z.

The mixture velocity v_m differs from the mixture bulk velocity $\overline{v_m}$ due to the mass averaging used for v_m, see Section 6.2.5. For practical applications we are interested in the mixture bulk velocity (e.g. for control of the VTS and for use in empirical modelling of wall friction). The bulk velocity $\overline{v_m}$ is defined as:

$$\overline{v_m} = c_v \cdot v_s + (1 - c_v) \cdot v_f \tag{6.8}$$

6.2.3. CENTRIFUGAL PUMP BOOSTER STATIONS

The driving force of the vertical transport operation is the pressure difference induced by a series of pump booster stations along the riser, i.e. the $\partial p_e / \partial z$ term in Equation 6.6. For centrifugal pumps, the actual pressure the pump is able to deliver depends on the flowrate through the pump, and the point of operation in steady state conditions is dictated by the total hydraulic resistance that needs to be overcome (Wilson et al., 2006). Furthermore, the delivered pressure of a centrifugal pump also depends on the mixture in the pump. An increasing mixture density increases the pump's delivered pressure, while the presence of solids slightly attenuates the delivered pressure and the pump's efficiency (McElvain, 1974).

A pump is modelled as a pressure source that can be placed anywhere along the riser. The strength of this pressure source is independent of the flowrate in the system, but it does include the effect of mixture density. When pumping water only, the pump delivers a pressure $p_{e,f}$.

The pump and drive dynamics are included by a typical pressure - drive speed ($p_{e,f}$ versus n_p) curve. The pump and drive need a few seconds to speed up from zero to maximum speed, typically $2-4\,s$. From the affinity law $p_{e,f,2}/p_{e,f,1} = (n_{p,2}/n_{p,1})^2$ it follows $p_{e,f} \propto n_p^2$ or $p_{e,f} \propto t^2$ when assuming $n_p \propto t$ (linear acceleration of the system). A typical graph for acceleration of the pump in $4\,s$ is given in Figure 6.4. The curve is limited to the maximum pressure $p_{e,f,max}$, which results in:

$$p_{e,f} = \frac{1}{t_e^2} \cdot p_{e,f,max} \cdot t^2 \quad 0 \le t \le t_e\, s \tag{6.9}$$

The pump pressure needed in the system depends on the preferred operational velocity. From the hydraulic design of the transport system, the preferred bulk velocity v_{set} is known. In the model a PID controller (Franklin et al., 2002) is implemented that adjusts the delivered pump pressure p_e in order to achieve the velocity $\overline{v_m} = v_{set}$:

$$p_e = \min(1, \max(0, Y)) \cdot \frac{\rho_m}{\rho_f} \cdot p_{e,f} \tag{6.10}$$

The pump pressure $p_{e,f}$ follows from the pump dynamics graph, the numerical implementation is discussed in Section 6.3.

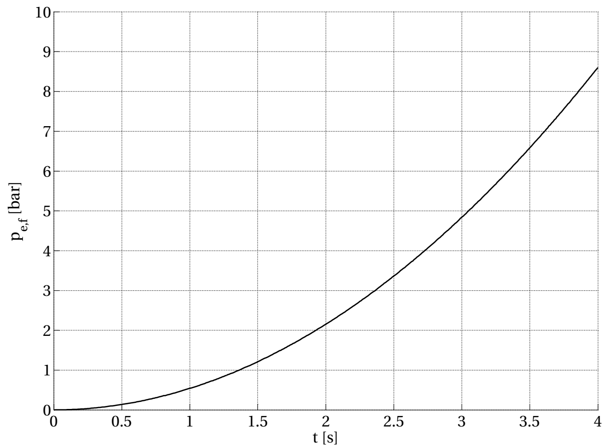

Figure 6.4: Development of the delivered pump pressure for startup of the pump in $t_e = 4\,s$. In this example the pump delivers a maximum pressure of $p_{e,f,max} = 8.6\,bar$ at maximum revolutions, which is reached after $4\,s$.

The control variable Y is defined as $Y = K_P \cdot e + K_I \cdot \int e\,dt + K_D \cdot d/dt(e)$, and the error e is defined as $e = v_{set} - \overline{v_m}$. The controller limits the pump pressure pressure to $0 \leq p_e \leq \rho_m/\rho_f \cdot p_{e,f}$, which mimics the increase or decrease in drive RPM. The model uses the same controller for all pumps.

6.2.4. WALL SHEAR STRESS

The wall shear stress τ_m, which describes the friction between the mixture and the pipeline, is assumed to consist of a carrier fluid component and a solids component Ferre and Shook (1998):

$$\tau_m = \tau_f + \tau_s \tag{6.11}$$

For fully developed turbulent pipeflow of water, the pressure loss due to friction Δp_f is proportional to v_f^2. The Darcy-Weisbach equation (White, 2003) correlates the bulk flow properties to the frictional loss:

$$\Delta p_f = f \cdot \frac{L}{D} \cdot \frac{1}{2} \cdot \rho_f \cdot v_f^2 \tag{6.12}$$

The pressure drop Δp_f can be rewritten to the wall shear stress of the fluid τ_f:

$$\tau_f = \frac{f}{8} \cdot \rho_f \cdot v_f^2 \tag{6.13}$$

The friction factor f for water can be obtained with the Moody diagram. In this diagram the friction factor is related to the Reynolds number Re for pipes with wall roughness ϵ_{pipe}. The Moody diagram is accurate to $\pm 15\%$. In the 1DVHT model the pipeline wall rougness is set to $2 \cdot 10^{-5}\,m$, which is typical for HDPE liner material. For the turbulent friction factor f_t, the explicit approximation to the Moody diagram of Haaland will be used (White, 2003), which approximates the Moody chart to 2% accuracy:

$$\frac{1}{\sqrt{f_t}} \approx -1.8 \cdot log\left(\frac{6.9}{Re} + \left(\frac{\epsilon_{pipe}/D}{3.7}\right)^{1.11}\right) \tag{6.14}$$

For the pressure loss in laminar flow, Equation 6.12 can be used with an alternative friction factor $f_l = \frac{64}{Re}$.

The Reynolds number Re is a dimensionless ratio between inertia forces and viscous forces:

$$Re = \frac{\rho_f \cdot v_f \cdot D}{\mu_f} \tag{6.15}$$

Modelling wall friction in non-stationary turbulent flows basically follows the framework of equation 6.12, but now with alternative velocity dependent friction factors. Zielke (1966) discusses different cases with laminar flow. Ribas and Deschamps (2004) report on numerical analysis of unsteady turbulent pipe flows, for which they find an increase in the friction factor up to a factor 1.8 compared to steady flow.

Whether to account for instationary turbulent flows depends on the velocity fluctuations. Ramaprian and Tu (1983) use the Strouhal number $St = \omega \cdot D/\sqrt{\tau_f/\rho_f}$, with ω being the frequency of oscillation of the flow in the pipe and τ_f being the fluid wall shear stress for steady flow. They distinct five regimes, and for each regime they give a suggestion for modelling wall friction. For Regime 1 ($St < 0.1$) and Regime 2 ($0.1 < St < 1$) the flow can be treated as quasi-steady, which means that the friction factor for steady flow can be used.

In the case of vertical hydraulic transport ($0 < v_f < 5\,m/s$, $0.2 < D < 1.0\,m$, $f \approx 0.01$), typical oscillation frequencies should not exceed $0.02\,Hz$ for the quasi-steady approach to hold. Ship heave motions are the main source of oscillation, and a combined hydrodynamic and internal flow analysis by Hannot and van Wijk (2014) shows that quasi-steady modelling applies.

While the description of τ_f is rather straightforward, the description of τ_s is less. The main idea for continuum modelling of grain shear stresses was posed by Bagnold (1954) and elaborated for the general case of cohesionless solids in a fluid in Bagnold (1956). He introduced a dimensionless number Ba, to distinguish between the viscous regime ($Ba < 40$) and turbulent or grain inertia regime ($Ba > 450$):

$$Ba = \frac{\lambda^{0.5} \cdot \rho_f \cdot d^2}{\mu_f} \cdot \left|\frac{\partial v}{\partial r}\right| \tag{6.16}$$

The ratio λ between grain diameter and mean radial separation distance of the particles is given by:

$$\lambda = \left[\left(\frac{c_{v,max}}{c_v}\right)^{1/3} - 1\right]^{-1} \tag{6.17}$$

For $Ba > 450$, i.e. the grain inertia regime, Bagnold gives the solid's shear stress τ_s as:

6

$$\tau_s = K_i \cdot \rho_s \cdot (\lambda \cdot d)^2 \cdot \left|\frac{\partial v}{\partial r}\right|^2 \tag{6.18}$$

The solids shear stress of Equation 6.18 includes both the interactions between the grains themselves and the interactions between the grains and the surroundings (e.g. the pipeline wall). Equation 6.18 has been the starting point for Shook and Bartosik (1994), Ferre and Shook (1998) and Bartosik (2010) in finding alternative expressions for τ_s for application in hydraulic transport. The model of Ferre and Shook (1998), which is implemented in the 1DVHT model, reads:

$$\tau_s = 0.0214 \cdot \left(\frac{\rho_s \cdot \overline{v_m} \cdot d}{\mu_f}\right)^{-0.36} \cdot \left(\frac{d}{D}\right)^{0.99} \cdot \lambda^{1.31} \cdot \rho_s \cdot \overline{v_m}^2 \tag{6.19}$$

Note the Reynolds number in Equation 6.19 uses particle properties ρ_s and d in combination with the mixture bulk velocity $\overline{v_m}$. Equation 6.19 has been compared with the data of Xia et al. (2004a) in Section 2.2.3 (Figure 2.1), showing good agreement. The implementation of Equation 6.19 in the 1DVHT model uses the volume averaged solids density and solids diameter.

Due to the action of various external forces, long risers exhibit swaying motions. Xia et al. (2004b) experimentally studied the effect of swaying motions on frictional losses by forcing a 10 m steel riser laterally at frequencies of 0.2, 0.4 and 0.6 Hz with excursions of 0.15, 0.25 and 0.4 m. The particle properties are comparable to those used in Xia et al. (2004a), the volume fraction of solids has been kept constant at $c_v = 0.1$. The experiments show $1 \leq i_t / i_{t,static} \leq 1.65$. For the three cases the relative effect seems to be independent of the frequency of motion. For typical operating velocities $\overline{v_m} > 2.5\, m/s$ the relative effect is smaller than 15%.

When the volume fraction of solids approaches its maximum, the mixture starts behaving more and more like a solid plug. In the 1DVHT model, τ_s for solid plugs is given by the model of Chapter 5:

$$\tau_s = \frac{D}{4} \cdot \left[\left(\rho_s - \rho_f\right) \cdot c_v \cdot g\right] \cdot \left[1 - \frac{D}{4 \cdot \mu_k} \cdot \frac{1+\sin\Phi}{1-\sin\Phi} \cdot \frac{1}{L} \cdot \left(1 - e^{\frac{4 \cdot \mu_k}{D} \cdot \frac{1-\sin\Phi}{1+\sin\Phi} \cdot L}\right)\right] \tag{6.20}$$

The numerical implementation of Equation 6.20 is not straightforward, since the actual constitution of the plug needs to be known. This would require a subgrid model of the plug. Instead, we use this equation with a conservative approach. We define the plug length as the length of the region where it holds $c_v \geq c_{v,max}$. The solids density varies over this plug, since it consists of particles with (potentially) different densities. We use a volume averaged solids density, i.e. by averaging the density of each particle type with its relative volume fraction. Next to that, we need to know the coefficient of friction (both static and dynamic) between the solids and the riser wall, and we need to know the angle of internal friction of the different particle types. The individual quantities could be found by standard tests or by consulting reference tables. In the implementation of the plug friction model, we use a single friction coefficient, assuming that the fractions are mixed homogeneously along the riser's perimeter. The angle of internal friction is harder to assess. Ideally, this parameter should be investigated for different mixtures of the materials at hand, but in the 1DVHT model a single angle of internal friction is used. We conducted a sensitivity analysis on Equation 6.20 to assess the sensitivity of τ_s for variation of the individual parameters L, μ_k and Φ (densities and diameter are very well measurable with high certainty, but assessment of the soil mechanical parameters or effective plug length is harder). To this end we defined a standard plug with $L = 0.5\,m, D = 0.1\,m, \mu_k = 0.3, \Phi = 30^o, \rho_s = 2650\,kg/m^3$ and $c_{v,max} = 0.6$. Then we varied the parameters by $\pm 10\,\%$ and looked at the variation in τ_s. This showed that a change of $10\,\%$ in μ_k or L results in roughly $10\,\%$ variation in τ_s. Variation of Φ with $10\,\%$ results in variation of τ_s with roughly $2\,\%$.

It is hard to give an exact demarcation between a dense suspension and a solid plug, since the change from dense suspension rheology to actual soil mechanics is only a matter of minor variation in the volume fraction of solids. The choice for a treshold value in the proximity of the closest packing is rather arbitrary, but it is a reasonable approach. Therefore in the model the solids contribution to wall friction is computed as:

$$\tau_s = \begin{cases} \text{Equation 6.19}, & \text{if } 0 \le c_v < c_{v,max} \\ \text{Equation 6.20}, & \text{if } c_v = c_{v,max} \end{cases} \tag{6.21}$$

According to Equation 6.19, in the limit $c_v \to c_{v,max}$ it holds $\tau_s \to +\infty$. The implementation of Equation 6.21 now limitis τ_s to the value obtained with Equation 6.20.

6

6.2.5. SOLIDS TRANSPORT VELOCITY

The velocity of particles in the carrier fluid, v_s, is smaller than the fluid velocity v_f due to the action of gravity. This implies the existence of a slip velocity v_{slip} between the solid phase and the fluid phase:

$$v_{slip} = v_f - v_s \tag{6.22}$$

We use hindered settling theory to model the slip velocity, following the method outlined in Goeree and Van Rhee (2013). The vertical transport velocity $v_{s,k}$ of fraction k is given by the cross sectional averaged fluid velocity (in an empty riser) v_f corrected for the hindered settling velocity of that fraction:

$$v_{s,k} = v_f - w_{h,k} \tag{6.23}$$

For K fractions, using mass averaging, continuity yields:

$$v_m = \sum_{k=1}^{K} c_{v,k} \cdot \frac{\rho_{s,k}}{\rho_m} \cdot v_{s,k} + \left(1 - \sum_{k=1}^{K} c_{v,k}\right) \cdot \frac{\rho_f}{\rho_m} \cdot v_f \tag{6.24}$$

Substitution of Equation 6.23 in Equation 6.24 and elaborating for v_f results in an expression for v_f in terms of the mixture velocity and the hindered settling velocity of fraction k:

$$v_f = v_m + \sum_{k=1}^{K} c_{v,k} \cdot \frac{\rho_{s,k}}{\rho_m} \cdot w_{h,k} \tag{6.25}$$

The solid's transport velocity is obtained by substitution of Equation 6.25 in Equation 6.23:

$$v_{s,k} = v_m + \sum_{k=1}^{K} c_{v,k} \cdot \frac{\rho_{s,k}}{\rho_m} \cdot w_{h,k} - w_{h,k} \tag{6.26}$$

The slip velocity of solid plugs is simply given by hindered settling theory in the upper limit of c_v.

Solid particles lose energy upon collision with the riser wall. Wall friction thus has an influence on the transport velocity of the solid fraction, which can be modelled as an additional slip velocity as shortly discussed in Chapter 2. In the 1DVHT model this influence is neglected.

The hindered settling velocity $w_{h,k}$ consists of two parts. The first part is the terminal settling velocity of a particle w_t, i.e. the velocity a particle finally obtains during settling in an infinite fluid domain. The second part is a correction term taking into account the influence of the surrounding particles on the settling velocity of a single particle. For settling of mono-disperse mixtures (i.e. mixtures containing equally sized particles) in still water Richardson and Zaki (1954) give:

$$w_h = w_t \cdot (1 - c_v)^n \tag{6.27}$$

6

The fluidization experiments of Richardson and Zaki (1954) resulted in a slightly different expression for the particle velocity as a function of the volume fraction of solids due to the presence of a velocity gradient:

$$w_h = 10^{-d/D} \cdot w_t \cdot (1 - c_v)^n \tag{6.28}$$

Equation 6.28 contains the influence of particle size with respect to the pipe diameter, which is the main difference between the cases of sedimentation and fluidisation.

Mirza and Richardson (1979) showed that Equation 6.27 also holds for sedimentation of polydisperse suspensions, i.e. suspensions containing particles of different sizes. When using Equations 6.27 and 6.28 in the framework of Equation 6.26, v_f is defined as the superfical fluid velocity (i.e. an empty riser). Equations 6.27 and 6.28 therefore need to be divided by $(1 - c_v)$ to make the slip velocity relative to the actual fluid velocity, which is implemented by setting the exponent $n \leftarrow (n-1)$.

The exponent n is a function of the particle Reynolds number Re_p. The original equations for n as given by Richardson and Zaki (1954) read $n = 4.65$ for $Re_p \le 0.2$, $n = 4.35 \cdot Re_p^{-0.03}$ for $0.2 < Re_p \le 1$, $n = 4.45 \cdot Re_p^{-0.1}$ for $1 < Re_p \le 200$ and $n = 2.36$ for $Re_p > 200$. The particle Reynolds number Re_p is given by:

$$Re_p = \frac{w_t \cdot \rho_f \cdot d}{\mu_f} \tag{6.29}$$

The exponent n can be expressed as:

$$n = \frac{a + b \cdot Re_p^{\alpha}}{1 + c \cdot Re_p^{\alpha}} \tag{6.30}$$

Different sets for the parameters in Equation 6.30 are available, see Table 6.2 (Garside and Al Dibouni, 1977; Rowe, 1987; Di Felice, 1999). The set of Rowe (1987) is a representation of the original parameters of Richardson and Zaki (1954) which will be used in the 1DVHT model.

Table 6.2: Different values for the parameters in Equation 6.30

Author	Garside et al. (1977)	Rowe (1987)	Di Felice (1999)
Re_p	$0.001 < Re_p < 3 \cdot 10^4$	$0.2 < Re_p < 1 \cdot 10^3$	$0.01 < Re_p < 1 \cdot 10^3$
c_v	$0.04 < c_v < 0.55$	$0.04 < c_v < 0.55$	$0 < c_v < 0.05$
a	5.1	4.7	6.5
b	0.27	0.41	0.3
c	0.1	0.175	0.1
α	0.9	0.75	0.74

Alternatives for the hindered settling theory of Richardson and Zaki (1954) can be found in the work of Winterwerp (1999), Lockett and Bassoon (1979) and Berres et al. (2005). These are primiraly modifications of Equation 6.27 rather than completely new models. The model of Berres et al. (2005) is the most elaborate. Its applications are discussed in Basson et al. (2009) and Dorell and Hogg (2010).

The last topic to discuss with respect to advection is the terminal settling velocity of a single particle, w_t. The equation of motion of a sphere with velocity w submerged in a fluid, subjected to the forces of gravity, buoyancy and drag, is given by:

6

$$\left(\frac{\pi}{6} \cdot d^3 \cdot \rho_s + m_a\right) \cdot \frac{dw}{dt} = \frac{\pi}{6} \cdot d^3 \cdot (\rho_s - \rho_f) \cdot g - \frac{1}{2} \cdot C_D \cdot w^2 \cdot \frac{\pi}{4} \cdot d^2 \cdot \rho_f \tag{6.31}$$

The added mass m_a of a sphere is given by half the mass of the water it displaces, so $m_a = 1/2 \cdot \pi/6 \cdot d^3 \cdot \rho_f$. For non spherical particles computation of m_a is more complex.

Equation 6.31 gives much insight in the particle momentum response time t_p, for this is the time required for a particle to reach 63 % of its terminal velocity. As an example, a forward Euler time integration has been used to solve Equation 6.31 for a sphere with $d = 50\,mm$ and $\rho_s = 2650\,kg/m^3$ settling in still water with $\rho_f = 1025\,kg/m^3$. With inclusion of added mass, it takes the sphere 0.18 s to reach $w = 0.63 \cdot w_t$, and it takes the sphere 0.57 s to reach $w = 0.98 \cdot w_t$, with $w_t \approx 1.27\,m/s$. In 0.18 s the sphere has settled over a distance of 0.08 m, which is about $1.6 \cdot d$. In modelling hydraulic transport, one often assumes that particles instantaneously acquire their terminal velocity. The definition of instantaneously depends on the length scale one is looking at: using $\overline{v_m} = 5.0\,m/s$, during the response time of $t_p = 0.18\,s$ the particle has been transported over a distance $s = 0.18 \cdot 5.0 = 0.90\,m$. On the scale of a riser with $L = 5000\,m$, this indeed can be seen as instantaneously.

When $dw/dt = 0$, there is an equilibrium of forces and Equation 6.31 can be solved for w_t:

$$w_t = \sqrt{\frac{4 \cdot g \cdot (\rho_s - \rho_f) \cdot d}{3 \cdot \rho_f \cdot C_D}} \tag{6.32}$$

Years of research have resulted in accurate expressions for C_D for perfect spheres over the entire Re_p regime. An extensive comparison is given by Cheng (2009), from which it proves that the expression by Brown and Lawler (2003) (for $Re_p < 2 \cdot 10^5$) is a good approximation:

$$C_D = \frac{24}{Re_p} \cdot \left(1 + 0.15 \cdot Re_p^{0.681}\right) + \frac{0.407}{1 + 8710 \cdot Re_p^{-1}} \tag{6.33}$$

The settling velocity of sand and gravel can be found with empirical relations (Van Rijn, 1984). The Stokes equation for the laminar regime holds for $d \leq 0.1\ mm$:

$$w_t = \frac{\left(\rho_s/\rho_f - 1\right) \cdot g \cdot d^2}{18 \cdot \nu_f} \tag{6.34}$$

For sand in the range $1 \leq d \leq 0.1\ mm$, Zanke's equation can be used:

$$w_t = \frac{10 \cdot \nu_f}{d} \cdot \left(\sqrt{1 + \frac{0.01 \cdot \left(\rho_s/\rho_f - 1\right) \cdot g \cdot d^3}{\nu_f^2}} - 1\right) \tag{6.35}$$

For particles with $d > 1\ mm$ Van Rijn proposes:

$$w_t = 1.1 \cdot \sqrt{\left(\rho_s/\rho_f - 1\right) \cdot g \cdot d} \tag{6.36}$$

6

Equation 6.36 can be compared with Equation 6.32, from which it can be derived that for $\sqrt{4/3/C_D} = 1.1$ Equation 6.32 is equal to Van Rijn's Equation 6.36. This yields $C_D \approx 0.91$.

The transition from Equation 6.34 to Equation 6.35 shows a discontinuity, which is not favoured from both a physical and computational point of view. Ferguson and Church (2004) propose an alternative to Equations 6.34 to 6.36. They give a continuous expression for w_t:

$$w_t = \frac{\rho_s - \rho_f}{\rho_f} \cdot g \cdot d^2 \cdot \left(a \cdot \nu_f + \left[b \cdot 0.75 \cdot \frac{\rho_s - \rho_f}{\rho_f} \cdot g \cdot d^3\right]^{0.5}\right)^{-1} \tag{6.37}$$

The choice of parameters a and b in Equation 6.37 depends on the grain shape. For sand, Ferguson and Church (2004) give $a = 18$, $b = 1.0$, while for very angular material they give $a = 24$, $b = 1.2$. For spheres $a = 18$, $b = 0.4$ can be used. Figure 6.5 shows the comparison between Equations 6.34 to 6.36 and Equation 6.37. Based on this comparison, in the 1DVHT model we use Equation 6.37.

Another option for calculating w_t for non-spherical particles is looking for a representative particle diameter d in combination with an appropriate expression for C_D. Advanced models for C_D, using different shape factors (e.g. sphericity, length wise sphericity, cross wise sphericity) are presented inTran-Cong et al. (2004) and Hölzer and Sommerfeld (2008). An alternative analysis is provided by Loth (2008), while an extension of the work of Hölzer and Sommerfeld (2008) is presented in Zastawny et al. (2012) . The authors present new equations and fit parameters for the drag coefficient, lift coefficient and two torque coefficients of four types of non-spherical particles. Equations having this degree of sophistication are primarily used in numerical simulations in which an

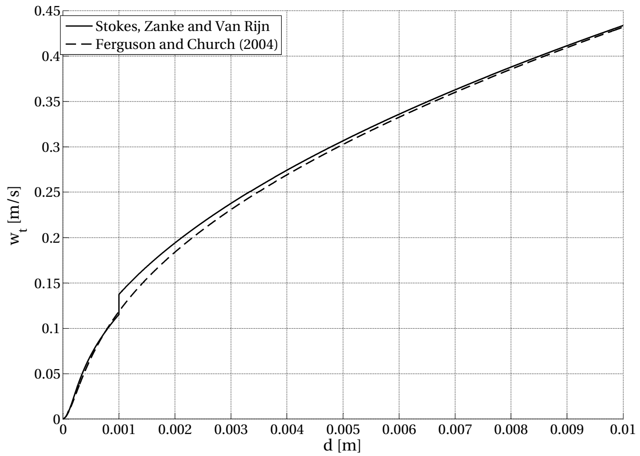

Figure 6.5: Comparision between Equations 6.34 to 6.36 and Equation 6.37. The model of Ferguson and Church (2004) using $a = 18$, $b = 1.1$ proves to be a very good alternative.

6

arbitrarliy shaped particle is positioned in a three dimensional (fully resolved) flowfield. For the purpose of this study, these equations are less useful.

Hölzer and Sommerfeld (2008) collected $C_D = f(Re_p)$ data from different sources. In Figure 6.6 curve fits to the three main datasets are presented.

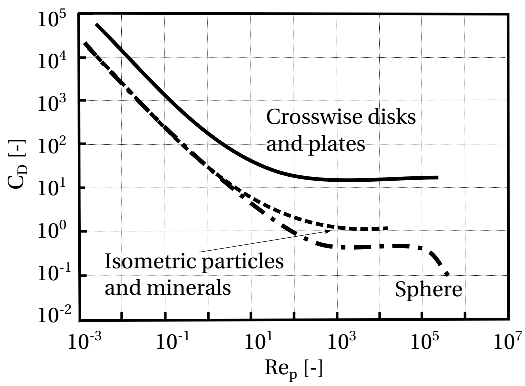

Figure 6.6: Drag coefficients for different particle shapes based on experimental data presented in Hölzer and Sommerfeld (2008).

In Figure 6.6 it can be seen that for $Re_p > 10^5$ the drag coefficient of a sphere suddenly collapses. This collapse is due to turbulence around the particle. Vertical hydraulic transport normally occurs at large flow Reynolds numbers. Macroscopic turbulence can have a significant influence on the turbulent wake of a single particle (Torobin and Gauvin, 1961). Neve (1986) has performed experiments that illustrate the shift in drag coefficient due to macroscopic turbulence. The larger the turbulence intensity, the larger the shift. Torobin and Gauvin (1961) found that the point of sudden collapse of drag coefficients could be shifted towards $Re_p \approx 10^3$, at which for a sphere they found $C_D \approx 0.1$. This effect, which is not taken into account in the 1DVHT model, motivated Sellgren (1982) to advise operating velocities in a vertical transport system of about $\overline{v_m} \approx 5 \cdot w_t$.

6.2.6. Axial dispersion coefficient

The effect of a non-uniform radial velocity profile in the riser and the effect of turbulence on the transport of solids is modelled by including axial dispersion in the advection-diffusion equation. The measurements described in Chapter 3 point out that the axial dispersion coefficient ϵ_z as used in Equation 6.7 relates to the Stokes number of a particle. In the 1DVHT model the dependency on the Stokes number is included as:

$$\epsilon_z = \epsilon_{Taylor} \cdot f(Stk) \tag{6.38}$$

The dispersion coefficient according to Taylor (1954) is given by:

$$\epsilon_{Taylor} \approx 5 \cdot D \cdot \sqrt{\frac{\tau_f}{\rho_f}} \tag{6.39}$$

6

The function $f(Stk)$ describes how the Taylor dispersion coefficient is affected by increasing Stokes numbers of the particles. It is based on the measurements described in Chapter 3. Figure 6.7 shows a linear fit through the data. From this relation, the function $f(Stk)$ is derived:

$$f(Stk) = \begin{cases} 1 - \frac{2}{3} \cdot Stk, & \text{if } 0 \leq Stk \leq 1.5 \\ 0, & \text{if } Stk > 1.5 \end{cases} \tag{6.40}$$

Clearly, the data set is too small to be conclusive on the real function $f(Stk)$. The function does however cover the basic physics: In the limit of small Stk, Taylor dispersion holds, and there is sufficient ground to assume an inverse relation between ϵ_z and Stk (Chapter 3). At this point there is no reason to make $f(Stk)$ more complex than a linear relation.

The Stokes number Stk is calculated by:

$$Stk = \frac{4 \cdot (\rho_s - \rho_f) \cdot d \cdot |\overline{v_m}|}{3 \cdot \rho_f \cdot D \cdot w_t \cdot C_D} \tag{6.41}$$

In the 1DVHT model, C_D is calculated from Equations 6.32 and 6.37.

6.3. Computational method

6.3.1. Solving the conservation equations

The computational domain is a riser with length L and diameter D. The simulated timespan is t_{sim}. A finite volume approach is used, which results in a finite difference discretization in the case of a one-dimensional model with constant cross sectional area.

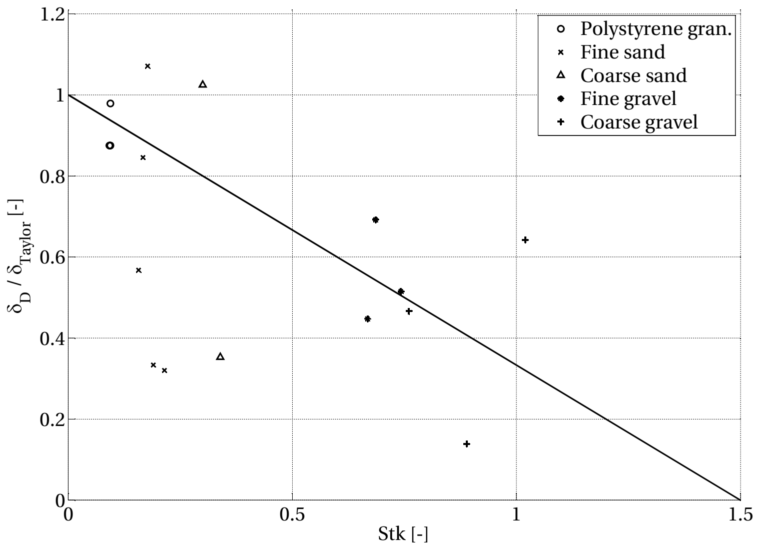

Figure 6.7: Implementation of the influence of particle inertia on the axial dispersion coefficient as based on experimental results (Chapter 3). The linear fit is the function $f(Stk)$.

The riser length is divided in m nodes, which gives a spatial step $\Delta z = L/(m-1)$. The timestep Δt is chosen such that it adheres to the stability criteria imposed by the advection-diffusion equation and time integration scheme. This results in a number of $t_{sim}/\Delta t$ discrete time steps. The particle size distribution is discretized in K fractions.

A fractional step method is used to solve the system of equations on a co-located grid (Hirsch, 2007; Mott et al., 2005). The scheme is second order accurate in space, second order accurate in time for the momentum equation and first order accurate in time for the velocity update step and the advection-diffusion equation. A typical timestep in the simulation proceeds as follows:

1. update ρ_m
2. update p_e
3. identify plugs and computation of plug lengths
4. calculate τ_m
5. calculate intermediate momentum $(\rho_m \cdot v)^*$
6. solve pressure poisson equation
7. calculate mixture velocity v_m

8. calculate ϵ_z
9. calculate v_s, v_f and $\overline{v_m}$
10. update the maximum packing limiter
11. calculate $c_{v,k}$ for all K fractions

The timestep is denoted j, the spatial step is denoted i.

Updating ρ_m is done by computation of Equation 6.3. Updating the pump pressure p_e requires more steps. First, the delivered pump pressure at the current timestep in the simulation ($p^j_{e,f}$) is compared with the pump dynamics graph. The dynamics graph has its own timeframe, which we will denote $\jmath$, using the same timestep Δt. Any change in pump pressure for time $j+1$ (as determined by the pump controller, Equation 6.9) is limited by the pump dynamics graph: $p^{j+1}_{e,f} = p^{\jmath\pm1}_{e,f}$.

The identification of plugs and the definition of their length is shown in Figure 6.8. In this figure, the effect of the maximum packing limiter is illustrated.

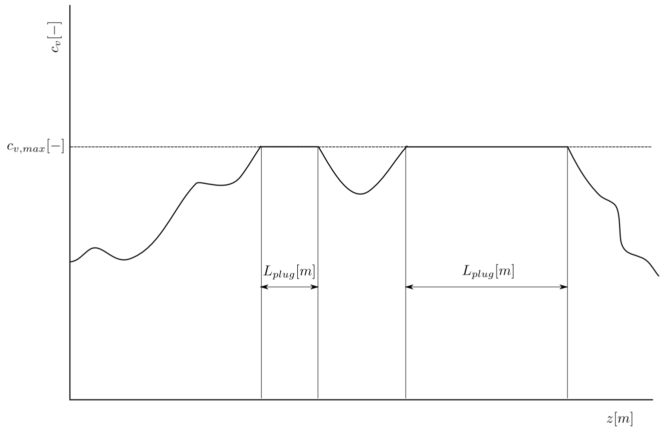

Figure 6.8: The volume fraction of solids varies over the riser length. The volume fraction of solids is limited to $c_{v,max}$ by the action of the maximum packing limiter. The region where it holds $c_v = c_{v,max}$ demarcates a plug.

The intermediate momentum $\left(\rho_m \cdot v\right)^*$ is computed using the Adams-Bashfort 2 time integration scheme (Hirsch, 2007):

$$\left(\rho_m \cdot v\right)^{*,j+1} = v^j_m \cdot \rho^j_m + \frac{\Delta t}{2} \cdot \left(3 \cdot M^j - M^{j-1}\right) \tag{6.42}$$

The forcing term M in Equation 6.42 is found by writing the mixture momentum equation, Equation 6.6, explicitly for $\partial p / \partial z$.

The second step is making the flow field obey $\frac{\partial v_m}{\partial z} + \frac{\partial \rho_m}{\partial t} = 0$ by solving the following equation for p:

$$\frac{\partial^2 p}{\partial z^2} = \frac{1}{dt} \cdot \frac{\partial (\rho_m \cdot v)^*}{\partial z} + \frac{\partial \rho_m}{\partial t} \tag{6.43}$$

Equation 6.43 is solved by using a successive overrelaxation method (Hirsch, 2007), the iterative loop runs until the maximum relative error is smaller than 10^{-4}. The two phase flow is incompressible with varying mixture density, hence inclusion of the term $\frac{\partial \rho_m}{\partial t}$.

Using Mott et al. (2005), the cell centered mixture velocity for the next time step v_m^{j+1} follows from:

$$v_m^{j+1} = \frac{\left(\rho_m \cdot v\right)_{i-1}^{*,j+1} + 2\left(\rho_m \cdot v\right)_{i}^{*,j+1} + \left(\rho_m \cdot v\right)_{i+1}^{*,j+1}}{4 \cdot \rho_m^j} - \frac{\Delta t}{2 \cdot \rho_m^j \cdot \Delta z} \cdot \left(p_{i+1}^{j+1} - p_{i-1}^{j+1}\right) \tag{6.44}$$

This procedure prohibits decoupling of the pressure and velocity field and it is able to handle large pressure gradients inside the domain very well. This is a prerequisite because the centrifugal pump booster stations introduce very large gradients.

6.3.2. SOLVING THE TRANSPORT EQUATION

Having updated the pressure field and the mixture velocity, transport of solids is computed by solving the advection-diffusion equation for each fraction, Equation 6.7. The bi-directional Lax-Wendroff finite difference scheme with flux limiters Ψ of Leveque (1990) is used, which allows for both positive and negative velocities (i.e. both upward transport and downward transport of solids). With this scheme, the advective flux (the fraction subscript k is omitted) $F = v_s \cdot c_v$ reads:

$$\begin{aligned} F_i^j = \frac{1}{2} \cdot c_{v,i}^j \cdot \left(v_{s,i}^j + v_{s,i+1}^j\right) - \frac{1}{2} \cdot c_{v,i}^j \cdot \left(|v_{s,i+1}^j| - |v_{s,i}^j|\right) + \dots \\ \dots + \frac{1}{2} \cdot \Psi_i \cdot \left(sgn\left(v_{s,i}^j\right) - v_{s,i}^j \cdot \frac{\Delta t}{\Delta z}\right) \cdot c_{v,i}^j \cdot \left(v_{s,i+1}^j - v_{s,i}^j\right) \end{aligned} \tag{6.45}$$

The discrete advection-diffusion equation uses two limiters. To suppress wiggles, the flux limiter Ψ of Van Leer (1974) is used. The volume fraction of solids is limited to $c_v = c_{v,max}$ while enforcing conservation of mass by the maximum packing limiter χ. It works on all advective fluxes. The rationale behind the packing limiter is that if a cell is full, the inward fluxes (to the cell) are turned off, while outward flux is still possible. The packing limiter for flux F_i^j works as:

$$\chi_{i+1} \cdot F_i^j \tag{6.46}$$

There are several options for the limiter function χ. Kuzmin and Gorb (2012) describe a limiter function which regulates the inward flux by comparing the actual packing with the maximum allowable packing in order to determine the maximum inward flux at the given Δz and Δt. The inward flux is then limited to this maximum allowable inward flux. A second option, which is implemented in the 1DVHT model, is a binary-type limiter which switches the inward fluxes off when the maximum packing is reached:

$$\chi_i = \begin{cases} 1, & \text{if } 0 < c_{v,i} < c_{v,max} \\ 0, & \text{if } c_{v,i} = c_{v,max} \end{cases} \tag{6.47}$$

The 1DVHT model is compared with the data of a sedimentation experiment in Appendix A. In this test, the sedimentation of sand with seven fractions is simulated. First, the sedimentation experiment is simulated with the advection-diffusion equation only. The results agree very well with the experiment. Secondly, for verification, the same simulation is performed with the full 1DVHT model. The results again agree very well.

6.4. Conclusions and recommendations

6.4.1. Conclusions

The vertical transport process can be modeled as one dimensional. The general flow dynamics of the VTS are governed by solving the conservation equations for the mixture only, assuming the mixture is homogeneous. A multi fraction simulation is of interest when interaction between the different fractions plays an important role, for instance with heterogeneous inflow (and subsequent risk of plug formation) or when the outflow conditions need to be known (for design of processing equipment).

In order to use a continuum approach, particles need to have spherical to mildly angular shapes. Any irregular hydrodynamic behaviour induced by particle shape (e.g. the tumbling behaviour of flat particles and their clustering) cannot be modeled.

The centrifugal pump and drive dynamics are included by an analytical description of the startup of the system. The most important parameter with respect to the transport process is the startup time of the pumps, for which the analytical approach is sufficient.

The occurence of density waves cannot be studied with the 1DVHT model.

Bagnold-like models for wall friction work well for homogeneous mixtures up to $c_v = 0.25$ compared with experimental data available in literature (surrogate manganese nodules in a vertical pipe), but when the volume fraction of solids reaches its maximum, these models start failing by largely overestimating wall friction.

6.4.2. Recommendations

The terminal settling velocity of the particles is modeled with an empirical equation, and the particles are assumed to arrive at their terminal settling velocity instantaneously. When typical transit times are of the same order of magnitude as the particle timescale, which is the case for relatively short transport lines or small spatial domains, particle dynamics become important and should be included explicitly in the model.

Including particle inertia in the model enables the study of density waves and assessment of flow stability. Before this can be implemented, a better understanding of the flow stability mechanism is needed (see also Chapter 2).

In the model, all pumps are controlled simultaneously. The model can be extended by implementing more advanced control algorithms.

7

CASE STUDY: THE VERTICAL HYDRAULIC TRANSPORT OF MANGANESE NODULES

In this chapter the hydraulic design and an internal flow analysis for a vertical hydraulic transport system for mining manganese nodules are presented. Four cases are discussed. A simulation of random inflow of solids gives information about general operation of the transport system. Simulation of pump failure and simulation of a total power blackout show the system behaviour during an emergency, and these simulations give an indication of important design considerations. The last simulation comprises the plug formation processes by batch interaction.

Parts of this chapter have been presented at the Seventeenth International Conference on Transport and Sedimentation of Solid Particles (2015), Van Wijk and Smit (2015).

7.1. INTRODUCTION

IN January 2014, a consortium of industrial partners, universities and knowledge institutes joined forces in the Blue Mining project (BlueMining, 2014), partially funded by the European Commission. The goal of the Blue Mining project is to advance the technology development of deep sea mining.

The consortium agreed on a reference case for the mining of manganese nodules in the German license area of the Clarion-Clipperton Zone, around which a part of the technology development will be centered.

The manganese nodule case will be elaborated in the next sections. It is not the intention to obtain the ultimate VTS design, but the goal is to demonstrate how the knowledge presented in this thesis can be used for design of a VTS and the simulation of the internal flow.

7.2. CASE DESCRIPTION

ONE of the areas of interest for manganese nodule mining is the Clarion Clipperton Zone (CCZ). The seawater temperature at a depth of several kilometers is relatively constant. Data on the water temperatures in the CCZ as retrieved from the NOAA database (NOAA, 2015) indicate that the intake water temperature at 5000 m below sea level is about $5^{o}C$, see Figure 6.1. The specifications of the case are given in Table 7.1.

Table 7.1: Case description: manganese nodules at 5000 m water depth.

Parameter	Description	Value
H	Water depth	5000 m
ρ_f	Density water	1025 kg/m^3
μ_f	dynamic viscosity water	$1.7 \cdot 10^{-3}$ Pas
ρ_s	Density solids	2500 kg/m^3
$\overline{s}$	Average dry solids production	111 kg/s
s_{max}	Maximum dry solids production	150 kg/s

The particle size distribution of the deposit is given in Figure 7.1.

7.3. DESIGN OF THE VERTICAL TRANSPORT SYSTEM

7.3.1. MAIN DIMENSIONS

THE VTS design method comprises optimization of the riser internal diameter, centrifugal pump size, average mixture density and booster station spacing. The method has an iterative character. The choice of parameters is bound to the constraint of minimum d/D ratio (which we take 1/3), the constraint of minimum bulk velocity in the riser, the constraint of minimum allowable pressures in the VTS and optimization of the Specific Energy Consumption. The power consumption is a function of the riser diameter since it determines the irreversible hydraulic losses. Moreover the centrifugal pump efficiencies together with the effect of solids on the pump performance are included in the calculation of the power consumption.

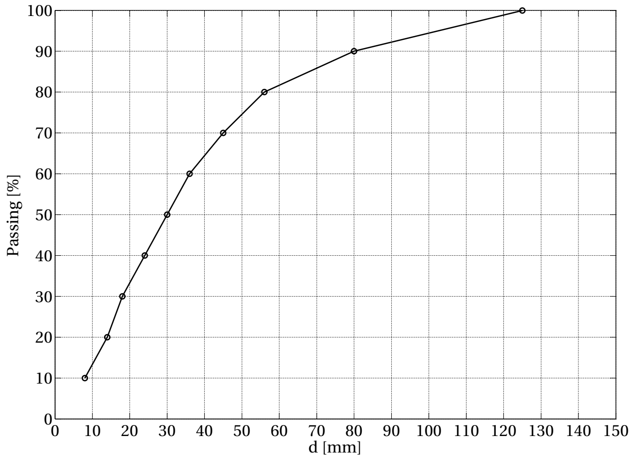

Figure 7.1: Particle size distribution of a typical manganese nodule sample from the CCZ.

The maximum particle diameter encountered in the batch is $d_{100} = 125\,mm$. From our laboratory experiments (Chapter 2) we know that a mono disperse mixture with $d/D = 1/3$ could just be fluidized. In the manganese nodule operation, with a wide particle size distribution, the largest particle will only be present once in a while, so here $d/D = 1/3$ is expected to work well. This gives $D = 3 \cdot 125 = 375\,mm$. In the oil and gas industry risers come in standard dimensions. We chose $D = 14" \approx 356\,mm$.

The minimum bulk velocity is chosen as twice the terminal settling velocity of a spherical particle with diameter d_{90}. The drag coefficient for design purposes is modeled according to Brown and Lawler (2003), i.e. the system should still be able to operate in the case of a perfectly spherical manganese nodule. With $d_{90} = 80\,mm$, the settling velocity in 5^oC seawater is $w_t = 1.80\,m/s$ so the minimum bulk velocity reads $\overline{v_{m,min}} = 3.6\,m/s$.

The design mixture density is $\rho_m = 1200\,kg/m^3$, or $c_v = 0.12$. To meet the average production requirement of $\overline{s} = 111\,kg/s$, the design bulk velocity is $\overline{v_m} = 4\,m/s$.

The VTS requires a relatively large pressure compared to the flow rate in the system, which forces centrifugal pumps to work outside the Best Efficiency Point. Choosing the suction diameter of the centrifugal pumps smaller than the riser diameter improves the point of operation, thus increasing the overall system's efficiency. This exercise can be conducted when pump performance data is available.

Wall friction is modeled with Equations 6.13 and 6.19. At $\overline{v_m} = 4\,m/s$, the total pressure needed to overcome the static weight (based on $\rho_m = 1200\,kg/m^3$) and wall friction is $\sum p_e = 103.6\,bar$. The VTS has 12 centrifugal pumps, divided over 6 booster stations, so each pump should (at least) deliver $p_{e,f} = 103.6/12 \cdot (1025/1200) = 7.37\,bar$ water pressure to maintain the design flow, not considering a possible efficiency reduction due to the solids in the mixture.

At $\overline{v_{m,min}} = 3.6\,m/s$, the required pressure is $\sum p_e = 99.85\,bar$, which yields a minimum pump pressure of $p_{e,f} = 7.11\,bar$.

Redundancy in drive and pump capacity will be necessary for safe operation. If we design for failure of one booster station (i.e. two centrifugal pumps), the minimum required pump pressure to maintain $\overline{v_{m,min}} = 3.6\,m/s$ is $p_{e,f} = 99.85/10 \cdot (1025/1200) = 8.53\,bar$.

Booster station spacing is important for assuring a minimum amount of over and under pressures in the riser, with the aim of minimizing the overall weight of the riser structure itself. The minimum allowable pressure follows from the structural design of the VTS and it is prescribed by design norms. We use $-5\,bar < p < 35\,bar$ as a first estimate. The structural design and its considerations are outside the scope of the present study, but taking into account the pressure development in the system in steady state conditions gives the design as depicted in Figure 7.2. The system specifications are shown in Table 7.2.

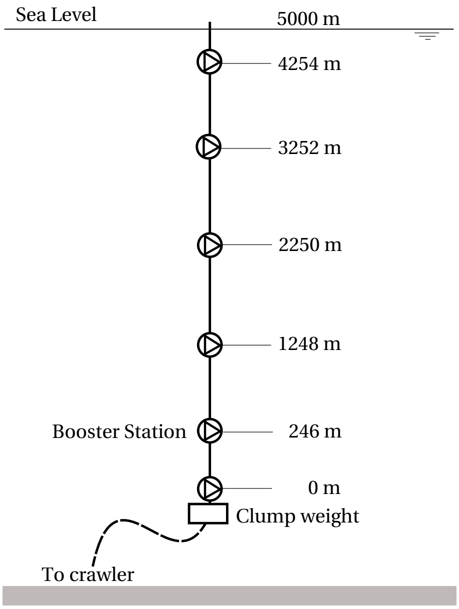

Figure 7.2: Schematic view of the VTS as designed for mining manganese nodules in the CCZ.

7.3.2. PUMP CONTROL TUNING

Now the main dimensions and system parameters have been determined, the pump control needs more attention. The centrifugal pumps can be modeled with or without inertia, see Equation 6.9. In order to find the suitable control parameters K_P, K_I and K_D of the PID controller, a simple test model is made. This model only includes limited physics, but it is sufficient to study the macroscopic system behaviour in relation to the control parameters.

This simple test model consists of a riser which gradually fills with mixture such that

Table 7.2: Specifications of the VTS.

Parameter	Specification
Internal diameter D	$356\,mm$
Pump pressure $p_{e,f}$ (min., nom., safe)	$7.1\,bar$, $7.4\,bar$, $8.6\,bar$
Bulk velocity $\overline{v_m}$	$4\,m/s$
Minimum velocity $\overline{v_{m,min}}$	$3.6\,m/s$
Slurry density ρ_m	$1200\,kg/m^3$
Volume fraction of solids c_v	0.12

after 1250 s the average density in the riser is $\overline{\rho_m} = 1200\,kg/m^3$, e.g. $\overline{\rho_m}(t = 0\,s) = \rho_f$ and $\overline{\rho_m}(t = 1250\,s) = 1200\,kg/m^2$. The flow is induced by a single pressure source of $p_{e,f} = 103.2\,bar$ (twelve pumps of 8.6 bar each), and they have a startup time $t_e = 4\,s$. The pumps are subjected to a mixture density $\rho_m = 1200\,kg/m^3$ which resembles the mixture density at the inlet. The pump including controller is implemented according to Equation 6.10. The forces on the mixture, besides the booster stations, are gravity and wall friction (modeled with the equivalent liquid model implemented as Equation 6.12 with a single friction factor $f = 0.015$). The resulting differential equation is:

$$\left(\overline{\rho_m}(t)\cdot L\right)\cdot\frac{\partial\overline{v_m}}{\partial t} = \frac{\rho_m}{\rho_f}\cdot p_{e,f} - \left(\overline{\rho_m}(t)-\rho_f\right)\cdot g\cdot L - f\cdot\frac{L}{D}\cdot\frac{1}{2}\cdot\rho_m\cdot\overline{v_m}^2 \qquad (7.1)$$

Equation 7.1 is solved with Euler forward time integration. The controller variables K_P, K_I and K_D are found by manual tuning looking for a short time to the setpoint velocity, limited overshoot and no oscillation before reaching the setpoint velocity. The setpoint velocity is $v_{set} = 4\,m/s$. The control settings thus found are $K_P = 1$, $K_I = 0.07$ and $K_D = 1$. These control parameters will be implemented in the 1DVHT model. Figure 7.3 shows the results with P control, PI control and PID control.

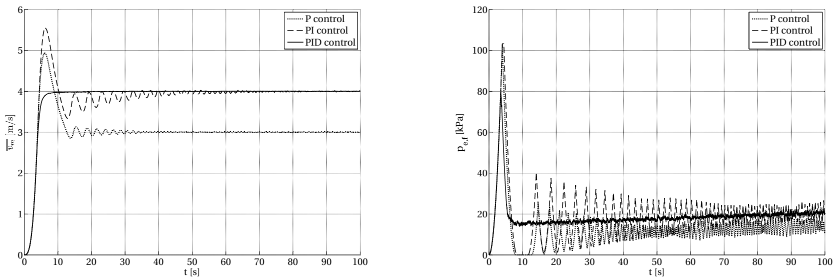

(a) Bulk velocity. (b) Total delivered pump pressure.

Figure 7.3: Simulation of startup of the VTS with pump inertia using Equation 7.1. The riser is gradually filled until after 1250 s the average density in the riser is $\overline{\rho_m} = 1200\,kg/m^3$. The pumps have a startup time of $t_e = 4\,s$ and they are subjected to a mixture density $\rho_m = 1200\,kg/m^3$ as well.

The control parameters are tested by comparison of the 1DVHT model and the test model for the startup of the VTS of Table 7.2. The simulated timespan is $20\,s$ and the setpoint velocity is $v_{set} = 4\,m/s$. No mixture is loaded or present in the riser. The friction factor is set fixed to $f = 0.015$. Figure 7.4 shows the results, which are similar for the 1DVHT model and the test model.

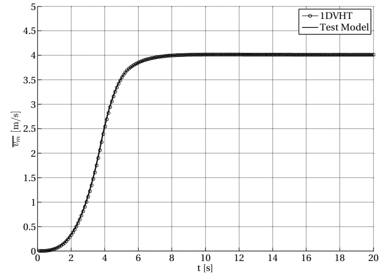

(a) Bulk velocity.

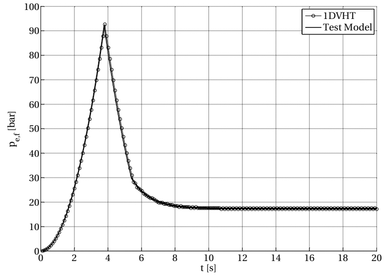

(b) Total delivered pump pressure.

Figure 7.4: Simulation of startup of the VTS with water only using the test model of Equation 7.1 and the 1DVHT model. The setpoint velocity is $v_{set} = 4\,m/s$, the friction factor is $f = 0.015$ and the control parameters are $K_P = 1$, $K_I = 0.07$ and $K_D = 1$.

7.4. INTERNAL FLOW CALCULATIONS

THE 1DVHT model will now be used to simulate four transport scenarios. These scenarios are based on the questions that regularly raise in discussion with engineers involved in designing a vertical transport system. First the operation of the VTS with random inflow of solids is simulated. Then the transport of a homogeneous mixture with a failing booster station is analyzed, followed by the simulation of a $6\,s$ power blackout and the loading scenario with consecutive batches of solids.

7.4.1. NORMAL CONDITIONS: RANDOM SOLIDS INPUT

In the case of random inflow, the maximum pump pressure is set to $p_{e,f} = 8.6\,bar$ and the pumps have a startup time of $t_e = 4\,s$. The volume fraction of solids at the inlet varies between $0 < c_v < 0.24$, with $\overline{c_v} = 0.12$. The transit time of the mixture is $5000\,m/4\,m/s = 1250\,s$. The simulation runs for $2000\,s$ to capture the full transport process. Figure 7.5 shows the volume fraction of solids at the inlet of the riser and the spatial distribution of material after $2000\,s$. The riser acts as a natural buffer which decreases the amplitude of the fluctuations over the course of transport, which is beneficial for the post processing of the mixture.

7.4.2. TRANSPORT OF A HOMOGENEOUS MIXTURE AND THE FAILURE OF A BOOSTER STATION

In this simulation we study the effect of failure of the first booster station (at $0\,m$ in Figure 7.2). After $1250\,s$, when the riser is entirely filled with mixture with $c_v = 0.12$, the

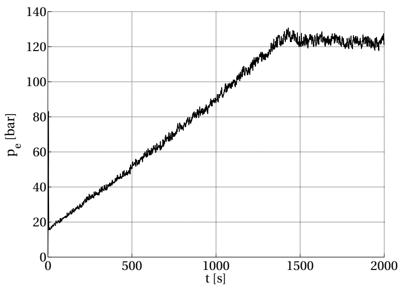

(a) Total delivered pump pressure.

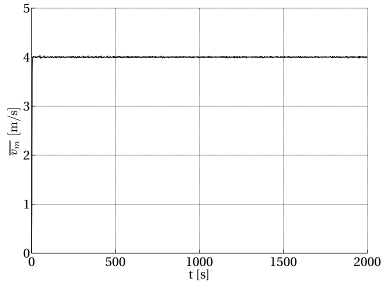

(b) Bulk velocity.

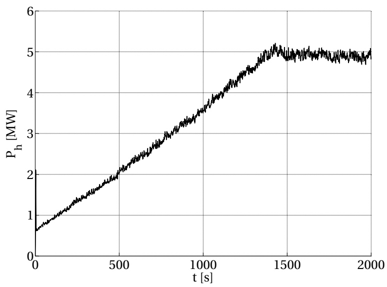

(c) Total hydraulic power.

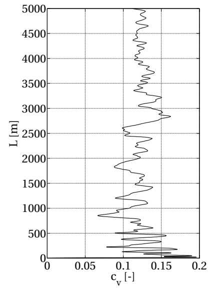

(d) Spatial distribution of the solids at $t = 2000\,s$.

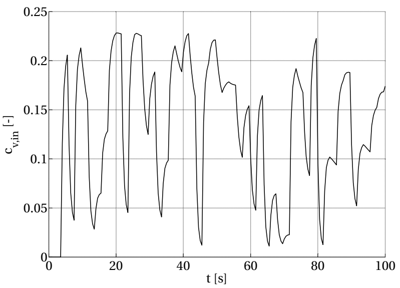

(e) Volume fraction of solids at the inlet of the riser.

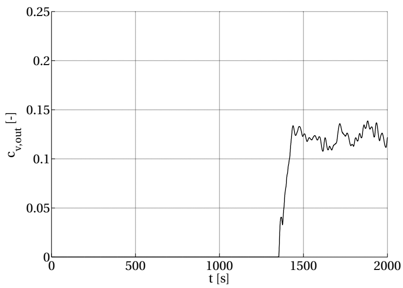

(f) Volume fraction of solids at the outlet of the riser.

Figure 7.5: Simulation of the vertical hydraulic transport with random inflow of solids. The riser acts as a buffer that suppresses the amplitude of the fluctuations at the outlet, which is beneficial for post processing operations.

two pumps in the bottom booster station stop working. The total simulated timespan is 4000 s so the recuperation of the system can be studied. The scenario has been simulated with pump pressures of 7.4 bar and 8.6 bar, as shown in Figure 7.6.

After failure of the first booster station, the system with $p_{e,f} = 8.6\,bar$ is able to maintain a bulk velocity of $\overline{v_m} = 3.7\,m/s$, which results in a stable production even after failure. The system with $p_{e,f} = 7.4\,bar$ however drops to $\overline{v_m} = 0.5\,m/s$. At this bulk velocity, the coarsest fraction takes a transport velocity of $v_s \approx -0.001\,m/s$ and the finest fraction has a velocity $v_s \approx 0.25\,m/s$. The coarse material will thus remain in the riser, and the production is limited to the material with $v_s > 0\,m/s$. This is reflected in the $c_{v,out}$ graph in Figure 7.6: only a minor amount of solids is actually leaving the riser, and at a much smaller rate than in the $p_{e,f} = 8.6\,bar/pump$ case. The hydraulic power at this velocity is small: not power but the maximum pump pressure is the limiting factor.

7.4.3. SIMULATION OF A TEMPORARY POWER BLACKOUT

The third scenario comprises a six seconds power blackout of the entire transport system. The VTS is loaded with a constant volume fraction of solids $c_v = 0.12$ and the set-point bulk velocity is $\overline{v_m} = 4\,m/s$. The simulated timespan is $2000\,s$. After $1250\,s$ the riser is entirely filled, and the booster stations stop working for $6\,s$.

The results are shown in Figure 7.7. Six seconds of no forcing is sufficient for the mixture to come to a halt and flow back through the system. It reaches a maximum downward velocity of about $5\,m/s$ when the booster stations start working again. The recuperation to upward flow takes $13\,s$, and after about $100\,s$ the flow is stable again. The pressure shows minor wrinkles, which is an artifact of the discrete pump pressure implementation.

Without any safety means the mixture will flow back through the VTS and the SMT to the seafloor, and there is a serious risk of riser blockage when the mixture is forced backward through the booster stations. Material can accumulate in a pump's suction side, an effect not included in the 1DVHT model. This scenario requires attention when doing detailed engineering of the VTS.

Without accumulation, the relatively quick recuperation of the flow results in only a minor (and negligible) effect of the blackout on the VTS production.

7.4.4. LOADING OF THE VTS WITH CONSECUTIVE BATCHES

In the last simulation the risk of riser blockage due to the loading of consecutive batches is investigated. The batches are loaded with a volume fraction of solids $c_v = 0.12$. First the coarsest material is inserted, followed by the finer fractions.

This input scenario is only possible when there is a feeder system (mixing tank with buffer capacity) which induces segregation of the initially homogeneous mixture. To make an estimation of a realistic loading time, we have to estimate the available capacity of the feeder system. A mixing tank volume of $10\,m^3$ seems a realistic first estimate. If the volume fraction of solids in the mixing tank is $c_v = 0.4$, there is $4\,m^3$ of solids. With a bulk velocity of $\overline{v_m} = 4\,m/s$ and volume fraction of solids $c_v = 0.12$ in the transport system, it takes the feeder system $84\,s$ to empty. Given the PSD of the manganese nodules, the inflow time for each fraction is $8.4\,s$. After $84\,s$ of loading there is a $2\,s$ pause, then the batches are followed by homogeneous mixture.

Figure 7.8 shows the results of the simulation. The train of batches with $c_v = 0.12$ slowly develops in a plug with $c_v \approx 0.34$ which leaves the riser. This increase in c_v poses no direct risk of riser blockage to the system, but it does have an impact on the cen-

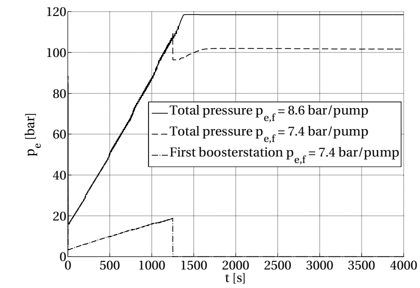

(a) Total delivered pump pressure.

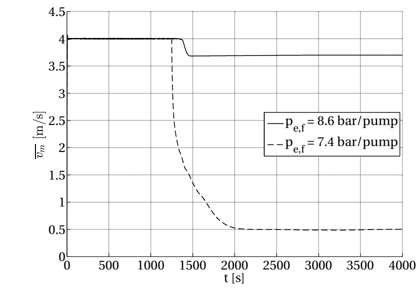

(b) Bulk velocity.

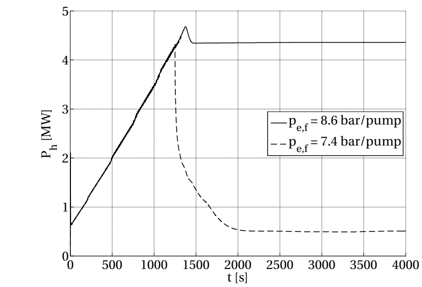

(c) Total hydraulic power.

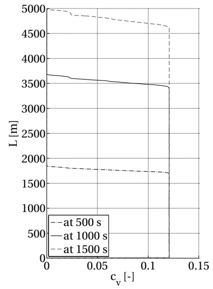

(d) Spatial distribution of the solids for $p_{e,f} = 7.4\, bar/pump$.

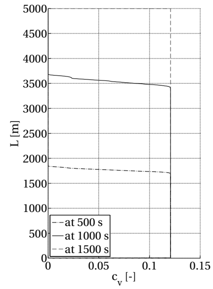

(e) Spatial distribution of the solids for $p_{e,f} = 8.6\, bar/pump$.

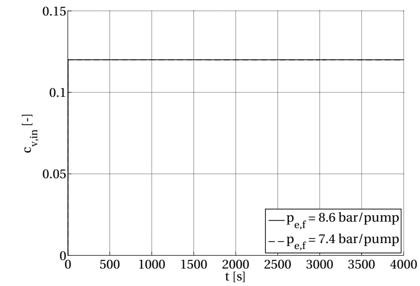

(f) Volume fraction of solids at the inlet of the riser.

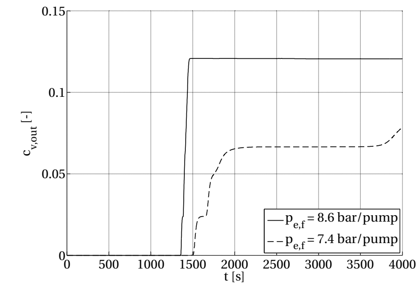

(g) Volume fraction of solids at the outlet of the riser.

Figure 7.6: Simulation of the failure of the bottom booster station. In the $p_{e,f} = 7.4\, bar/pump$ case the bulk velocity drops to $\overline{v_m} = 0.5\, m/s$ and the production falls, while in the $p_{e,f} = 8.6\, bar/pump$ case the velocity remains sufficiently large to maintain production.

trifugal pump booster stations and the post-processing equipment. Large fluctuations in c_v result in large forces on the pumps which causes increased wear. Especially the

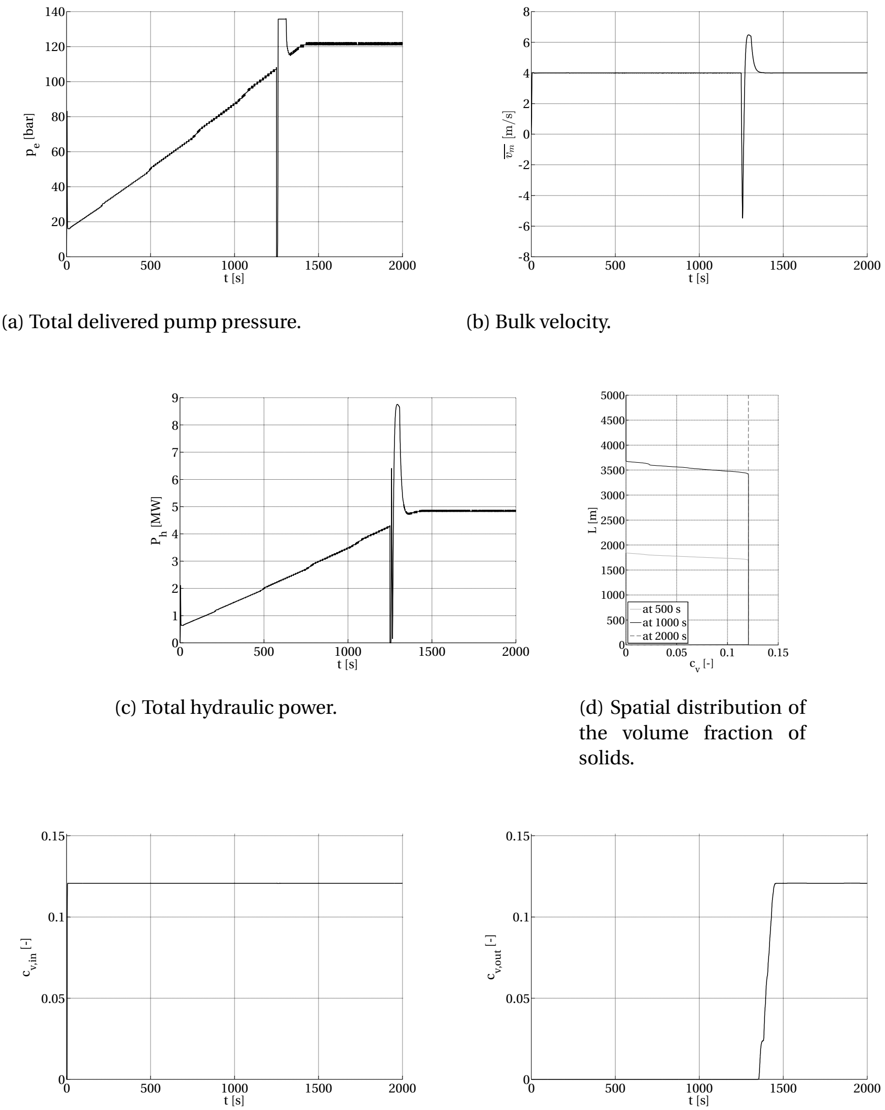

(a) Total delivered pump pressure.

(b) Bulk velocity.

(c) Total hydraulic power.

(d) Spatial distribution of the volume fraction of solids.

(e) Volume fraction of solids at the inlet.

(f) Volume fraction of solids at the outlet.

Figure 7.7: Total delivered pump pressure, mixture bulk velocity, total hydraulic power and volume fraction of solids for boosters with $p_{e,f} = 8.6\,bar$ suffering from a $6\,s$ power blackout after $1250\,s$ of operation. The blackout results in a large return flow of mixture, but it has no significant effect on the production of the system.

last booster station experiences a large sudden increase in force due to the batch with $c_v \approx 0.34$. Furthermore, large fluctuations in outflow require increased buffer capacity on deck.

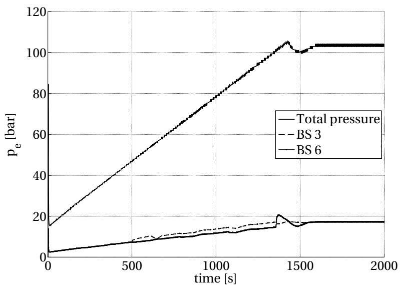

(a) Total delivered pump pressure.

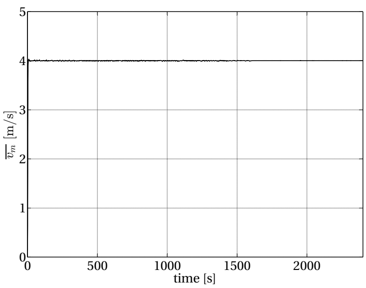

(b) Bulk velocity.

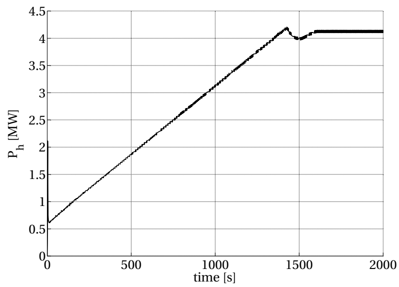

(c) Total hydraulic power.

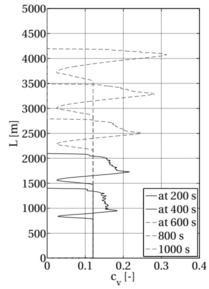

(d) Spatial distribution of the volume fraction of solids.

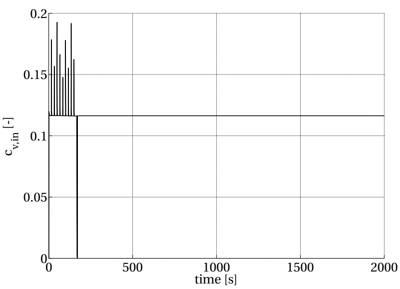

(e) Volume fraction of solids at the inlet.

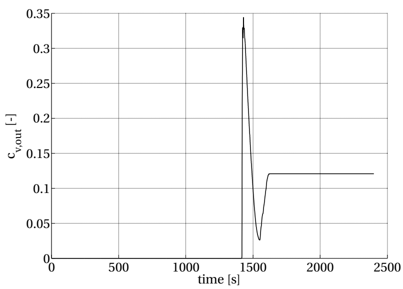

(f) Volume fraction of solids at the outlet.

Figure 7.8: Total delivered pump pressure, mixture bulk velocity, total hydraulic power and volume fraction of solids for boosters with $p_{e,f} = 8.6\,bar$. The VTS is loaded with consecutive batches of solids, with the coarsest fraction first, followed by finer material. A small plug develops but there is no risk of riser blockage in this case.

7.5. CONCLUSIONS AND RECOMMENDATIONS

IN this chapter the 1DVHT model has been applied to a case study for mining manganese nodules in the CCZ. First the design of the VTS has been presented, then four scenarios have been simulated.

Due to the large static weight of the mixture in the 5000 m riser, about 83% of the available pressure is used for the static weight, and the remaining 17% is used to overcome friction and obtain the setpoint velocity. When there is a failure of one of the pumps resulting in a pressure decrease of more than 17%, the operation comes to a standstill and return flow of mixture is a large risk.

In the detailed design of a VTS, the two main points of attention are sufficient redundancy in pump capacity (as demonstrated with the simulation of a failing booster station) and the design of an emergency dump valve or return line in case of return flow of mixture.

Fluctuations in the volume fraction of solids at the inlet of the VTS are largely damped out during the transport process, which is favorable for the post processing of the ore.

The risk of plug formation and riser blockage has been demonstrated in this thesis, but for the case of mining manganese nodules as presented in this chapter no direct risk of riser blockage has been found. Loading of consecutive batches with $c_v = 0.12$ during a realistic timespan of 84 s results in the formation of a plug with $c_v = 0.34$, which results in large forces on the booster stations and which requires larger buffer capacity on deck.

8

CONCLUSIONS AND RECOMMENDATIONS

In this chapter the overall conclusions and recommendations of this research project are presented.

8.1. CONCLUSIONS

SLIP VELOCITIES, DENSITY WAVES, CLUSTER FORMATION

Hindered settling theory can be used to model particle slip velocities for particles with $d/D = O(10^{-1})$. For angular material the limitation on d/D is more strict than for spherical particles.

Flat particles tend to form clusters. The risk of riser blockage due to cluster formation is strongly related to particle shape. The more angular and flat the material, the larger the risk of cluster formation.

The density waves as observed in the fluidization experiments could not be reproduced for transport conditions. Transport processes seem to be more stable than fluidization processes, which is partly attributable to the effect of wall friction of the solids.

AXIAL DISPERSION

Axial dispersion has a small influence on the vertical transport process.

Axial dispersion relates to particle inertia. The larger the particle inertia, the smaller the axial dispersion which makes the process less significant for the transport of highly inert particles like large manganese nodules.

The small axial dispersion increases the risk of riser blockage by batch interaction.

PLUG FORMATION BY MERGING BATCHES

The interaction between batches of solids with different transport velocities can result in blockage of the riser. To this end, the particles should show hardly any axial dispersion (i.e. the particles should have large Stokes numbers) and the ratio of mean particle diameters of the batches should not be too large. Based on numerical simulations with the 1DVHT model, the chances of blockage due to batch interaction seem very small.

WALL FRICTION OF SOLID PLUGS

8

Layered sediment plugs show wall friction largely exceeding their submerged weight, provided that the upstream side of the plug has negligible permeability.

MODELLING VERTICAL HYDRAULIC TRANSPORT

The vertical transport process can be modeled as a one dimensional process, provided the solid phase has spherical to mildly angular shapes.

MEASURING THE VOLUME FRACTION OF SOLIDS

The conductivity concentration meters as used in this research project are sensitive to the particle diameter. This sensitivity can be compensated for by proper calibration.

8.2. RECOMMENDATIONS

SLIP VELOCITIES, DENSITY WAVES, CLUSTER FORMATION

When using the 1DVHT model for a specific project, it is recommended to get a representative sample of the material and run a fluidization experiment. In this way the slip velocities can be determined accurately.

The experiments described in this thesis are conducted in test setups with vertical lengths of several meters. Especially with respect to the occurence of density waves and the verification of the 1DVHT model from a macroscopic perspective, it is recommended to conduct experiments in a test setup which is an order of magnitude longer.

AXIAL DISPERSION

For detailed studies of plugs or slugs, more research is needed into the relation between axial dispersion and the volume fraction of solids, especially for dense mixtures.

PLUG FORMATION BY MERGING BATCHES

The influence of the particle diameter ratio of the different batches on the risk of riser blockage has been related to the Terzaghi filter rule. In this thesis we were only able to test a limited set of particles. For future research it is recommended to study the influence of the diameter ratio in more detail and to assess the influence of particle shape as well.

WALL FRICTION OF SOLID PLUGS

In this thesis the wall friction of layered sediment plugs has been studied. The impermeable bottom layer of layered plugs has been identified as the main source of a nonzero axial stress condition in the plug, which induces wall friction. The nonzero stress condition is the key factor in wall friction of plugs, and other ways to have a nonzero axial stress is when a plug (not neccesarily layered) is forced through a bend. This should be studied in more detail since the pipework of centrifugal pump booster stations contain sharp bends.

MODELLING VERTICAL HYDRAULIC TRANSPORT

The occurence of density waves cannot be studied with the present 1DVHT model. For the study of density waves it is recommended to use a numerical model on a smaller length scale which includes particle inertia.

For computations of small spatial domains, where the particle transit times and response times are of the same order of magnitude, particle dynamics should be included as well.

MEASURING THE VOLUME FRACTION OF SOLIDS

The conductivity of fluids is a strong function of temperature. The conductivity concentration meters used in this research project only give an accurate indication of the volume fraction of solids when the sensor readings are compensated for the temperature effects in the fluid or mixture. It is recommended to improve the sensors by introducing a reference probe for clear water.

The conductivity concentration meters should always be calibrated with a fluidization test before using them for quantitative analysis.

BIBLIOGRAPHY

Acuna, C., Leiva, M., and Kuan, S. H. (2014). Online bed height and solids concentration sensor for thickeners based on conductivity and neural networks. *Tailings 2014. Second International Seminar on Tailings Management.20-22 August, Antofagasta, Chile*, pages 1–10.

Archie, G. E. (1942). The electrical resistivity log as an aid in determining some reservoir characteristics. *Trans. AIME*, 146(1):54–62.

Bagnold, R. A. (1954). Experiments on a gravity-free dispersion of large solid spheres in a newtonian fluid under shear. *Proceedings of the Royal Society of London. Series A, Mathematical and Physical Sciences*, 225(1160):49–63.

Bagnold, R. A. (1956). The flow of cohesionless grains in fluids. *Philosophical Transactions of the Royal Society of London. Series A, Mathematical and Physical Sciences*, 249(964):235–297.

Banisi, S., Finch, J. A., and LaPlante, A. R. (1993). Electrical conductivity of dispersions: a review. *Minerals Engineering*, 6(4):369–385.

Bartosik, A. (2010). Influence of coarse–dispersive solid phase on the 'particles–wall' shear stress in turbulent slurry flow with high solid concentration. *The Archive of Mechanical Engineering*, LVII(1).

Basson, D. K., Berres, S., and Bürger, R. (2009). On models of polydisperse sedimentation with particle-size-specific hindered-settling factors. *Applied Mathematical Modelling*, 33:1815–1835.

Batchelor, G. K. (1988). A new theory of the instability of a uniform fluidized bed. *J. Fluid Mech.*, 193:75–110.

Bath, A. R. (1989). Deep sea mining technology: recent developments and future projects. *Offshore Technology Conference, May 1-4, Houston, Texas USA*, pages 333–340.

Berres, S., Bürger, R., and Tory, E. M. (2005). Applications of polydisperse sedimentation models. *Chemical Engineering Journal*, 111:105–117.

BlueMining (2014). Blue mining project website. Internet: http://www.bluemining.eu.

Borzone, L. A. and Klinzing, G. E. (1987). Dense–phase transport: Vertical plug flow. *Powder Technology*, 53:273–283.

Brebner, A. and Wilson, K. C. (1964). Theoretical considerations of vertical pumping of mine products. Technical Report 33, Queen's University Kingston, Ontario.

Brown, P. P. and Lawler, D. F. (2003). Sphere drag and settling velocity revisited. *Journal of Environmental Engineering-ASCE*, 3:222–231.

Chang, E. y. and Acrivos, A. (1987). Conduction of heat from a planar wall with uniform surface temperature to a monodispersed suspension of spheres. *J. Appl. Phys.*, 62(3):771–776.

Cheng, N. (2009). Comparison of formulas for drag coefficient and settling velocity of spherical particles. *Powder Technology*, 189:395–398.

Choi, H. J. (2008). Numerical simulations of vertical hydro–hoist of sms deposits. Master's thesis, Delft University of Technology.

Choy, T. C. (1999). *Effective medium theory, principles and applications*, volume 102 of *International Series of Monographs on Physics*. Oxford Science Publications.

Christov, I. C. and Stone, H. A. (2014). Shear dispersion in dense granular flows. *Granular Matter*, 16:509–515.

Chung, J. S. (2009). Deep-ocean mining technology iii: Developments. *ISOPE Ocean Mining Symposium, Chennai, India.*

Clauss, G. (1971). Foerderung mineralischer rohstoffe aus der tiefsee. *Foerdern und Heben*, 21(11):681–689.

Clift, R. and Manning-Clift, D. H. (1981). Continuous measurement of the density of flowing slurries. *Int.J. Multiphase Flow*, 7(5):555–561.

Cloete, F. L. D., Miller, A. J., and Streat, M. (1967). Dense phase flow of solids-water mixtures through vertical pipes. *Trans. Instn. Chem. Engrs.*, 45:392–400.

Condolios, E., Couratin, P., and Chapus, E. E. (1963). Pumping ores up vertical shafts. *Canadian Mining and Metallurgical Bulletin*, pages 187–198.

Di Felice, R. (1995). Hydrodynamics of liquid fluidisation. *Chemical Engineering Science*, 50(8):1213–1245.

Di Felice, R. (1999). The sedimentation velocity of dilute suspensions of nearly monosized spheres. *Int.J. Multiphase Flow*, 25:559–574.

Dorell, R. and Hogg, A. J. (2010). Sedimentation of bidisperse suspensions. *Int.J. Multiphase Flow*, 36:481–490.

Drew, L. W. (2009). The promise and peril of seafloor mining. *Oceanus Magazine (www.whoi.edu/oceanus)*, 47(3).

Eckstein, E. C., Bailey, D. G., and Shapiro, A. H. (1977). Self-diffusion of particles in shear flow of a suspension. *Journal of Fluid Mechanics*, 79(1):191–208.

Engelmann, H. E. (1978). Vertical hydraulic lifting of large–size particles. a contribution to marine mining. *Offshore Technology Conference, May 8-11, Houston, Texas USA.*

Evans, J. and Shook, C. A. (1991). Dispersion and slip effects in hydraulic hoisting of solids. *The Canadian Journal of Chemical Engineering*, 69:1166–1173.

Falconer, R. K. H. (1989). Chatham rise phosphates: a deposit whose time has come (and gone). *Marine Mining*, 8:55–67.

Ferguson, R. I. and Church, M. (2004). A simple universal equation for grain settling velocity. *Journal of Sedimentary Research*, 74(6):933–937.

Ferre, A. L. and Shook, C. A. (1998). Coarse particle wall–friction in vertical slurry flows. *Particulate Science Technology*, 16:125–133.

Flipse, J. E. (1969). An engineering approach to ocean mining. *Offshore Technology Conference, May 18-21, Houston, Texas USA.*

Foscolo, P. U. and Gibilaro, L. G. (1984). A fully predictive criterion for the transition between particulate and aggregate fluidization. *Chemical Engineering Science*, 29(12):1667–1675.

Foscolo, P. U. and Gibilaro, L. G. (1987). Fluid dynamic stability of fluidised suspensions: the particle bed model. *Chemical Engineering Science*, 42(6):1489–1500.

Franklin, G., Powell, J. D., and Emami-Naeini, A. (2002). *Feedback Control of Dynamic Systems.* Prentice Hall, fourth edition.

Fuller, W. B. and Thompson, S. E. (1906). The laws of proportioning concrete. *Transactions of the American Society of Civil Engineers*, 57(2):67–143.

Furnas, C. C. (1931). Grading aggregates i: Mathematical relations for beds of broken solids of maximum density. *Industrial and Engineering Chemistry*, 23(9):1025–1058.

Garside, J. and Al Dibouni, M. R. (1977). Velocity-voidage relationships for fluidization and sedimentation in solid liquid systems. *second Eng. Chem. Process Des. Dev.*, 16:206.

Gibilaro, L. G. (2001). *Fluidization-dynamics.* Butterworth Heinemann, Oxford.

Gibilaro, L. G., Di Felice, R., and Foscolo, P. U. (1990). Added mass effects in fluidized beds: application of the geurst-wallis analysis of inertial coupling in two-phase flow. *Chemical Engineering Science*, 45(6):1561–1565.

Gidaspow, D. (1994). *Mutliphase Flow and Fluidization.* Academic Press.

Glasserman, P., Videla, D., and Boehm, U. (1994). Liquid fluidization of particles in packed beds. *Powder Technology*, 79:237–245.

Goeree, J. C. and Van Rhee, C. (2013). Numerical simulation of hydrodynamical behaviour of sediment water mixtures. *WODCON XX: The Art of Dredging, Brussels, Belgium*, pages 1–14.

Govan, A. H., Hewitt, G. F., and Ngan, C. F. (1988). Particle motion in a turbulent pipe flow. *Int. J. Multiphase Flow*, 15(3):471–481.

Griffiths, I. M. and Stone, H. A. (2012). Axial dispersion via shear-enhanced diffusion in colloidal suspensions. *EPL*, 97(58005).

Hannot, S. D. A. and van Wijk, J. M. (2014). Heave induced internal flow fluctuations in vertical transport systems for deep ocean mining. *OMAE 2014 33rd International Conference on Ocean, Offshore and Arctic Engineering, San Fransisco, California, USA*.

Heller, V. (2011). Scale effects in physical hydraulic engineering models. *Journal of Hydraulic Research*, 49(3):293–306.

Hem, J. D. (1985). Study and interpretation of the chemical characteristics of natural water. *Department of the Interior, US Geological survey, Water-Supply Paper*, (2254):66–67.

Hiltunen, K., Jasberg, A., Kallio, S., Karema, H., Kataja, M., Koponen, A., Manninen, M., and Taivassalo, V. (2009). *Mutliphase Flow Dynamics Theory and Numerics*, volume 722 of *VTT Publications*. Technical Research Centre of Finland VTT.

Hirsch, C. (2007). *Numerical Computation of Internal and External Flows*, volume 1. Butterworth–Heinemann, second edition.

Holdich, R. G. and Sinclair, I. (1992). Measurement of slurry solids content by electrical conductivity. *Powder Technology*, 72:77–87.

Hölzer, A. and Sommerfeld, M. (2008). New simple correlation formula for the drag coefficient of non–spherical particles. *Powder Technology*, 184:361–365.

Johri, J. and Glasser, B. J. (2002). Connections between density waves in fluidized beds and compressible flows. *AIChE Journal*, 48(8):1645–1664.

Jop, P., Forterre, Y., and Pouliquen, O. (2006). A constitutive law for dense granular flows. *Nature*, 441:727–730.

Kunii, D. and Levenspiel, O. (1991). *Fluidization Engineering*. Butterworth–Heinemann, second edition.

Kuzmin, D. and Gorb, Y. (2012). A flux-corrected transport algorithm for handling the close-packing limit in dense suspensions. *Journal of Computational and Applied Mathematics*, 236:4944–4951.

Lee, M. M., Hanratty, T. J., and Adrian, R. J. (1989). An axial viewing photographic technique to study turbulence characteristics of particles. *Int. J. Multiphase Flow*, 15(5):787–802.

Leveque, R. (1990). *Numerical Methods for Conservation Laws*. Lectures in Mathematics, ETH Zurich. Birkhauser-Verlag.

Li, P., Jian, L., Tian, L., and Han, W. (2005). Simulation for the motion of polymetallic nodules in hydraulic hoist for deep sea mining. *ISOPE Ocean Mining Symposium, 9-13 October, Changsha, Hunan, China*, pages 110–114.

Liu, S. and Ha, Z. (2002). Prediction of random packing limit for multimodal particle mixtures. *Powder Technology*, 126:283–296.

Liu, S., Wang, G., Li, L., and Wang, Xu, Y. (2003). Virtual reality research of ocean polymetallic nodule mining based on comra's mining system. *ISOPE Ocean Mining Symposium, 15-19 September, Tsukuba, Japan*, pages 104–111.

Lockett, M. J. and Bassoon, K. S. (1979). Sedimentation of binary particle mixtures. *Powder Technology*, 24:1–7.

Loth, E. (2008). Drag of non-spherical solid particles of regular and irregular shape. *Powder Technology*, 182:342–353.

MacTaggart, R. S., Nasr-El-Din, H. A., and Masliyah, J. H. (1993). A conductivity probe for measuring local solids concentration in a slurry mixing tank. *Sep. Technol.*, 3:151–160.

Manninen, M. and Taivassalo, V. (1996). *On the Mixture Model for Multiphase Flow*, volume 288 of *VTT Publications*. Technical Research Centre of Finland VTT.

McElvain, R. E. (1974). High pressure pumping. *Skilling's Mining Review*, 36(4):1–8.

Mero, J. L. (1965). *The Mineral Resources of The Sea*, volume 1 of *Elsevier Oceanography Series*. Elsevier.

Mirza, S. and Richardson, J. F. (1979). Sedimentation of particles of two or more sizes. *Chemical Engineering Science*, 34:447–454.

Mott, D. R., Oran, E. S., and Kaplan, C. R. (2005). *A Robust Solver for Incompressible Flow on Cartesian Grids with Colocated Variables*. Naval Research Laboratory.

Murray, J. and Renard, A. F. (1876). Report on deep-sea deposits based on the specimens collected during the voyage of the h.m.s. challenger in the years 1872-1876. The H.M.S. Challenger Library http://19thcenturyscience.org/HMSC.

Nasr-El-Din, H., Shook, C. A., and Colwell, J. (1987). A conductivity probe for measuring local concentrations in slurry systems. *Int.J. Multiphase Flow*, 13(3):365–378.

Nederveen, H. v. (1968). A theoretical base for the pumping power and pressure drop calculations of a fluid, solid mixture in a vertical riser. *IHC Holland Marine Mining Division internal report*.

Neve, R. S. (1986). The importance of turbulence macroscale in determining the drag coefficient of spheres. *Int. Journal of Heat and Fluid Flow*, 7(1):28–36.

Newitt, D. M., Richardson, J. F., and Gliddon, B. J. (1961). Hydraulic conveying of solids in vertical pipes. *Trans. Instn. Chem. Engrs.*, 39:93–100.

Nicolas, M., Chomaz, J., and Guazzelli, E. (1994). Absolute and convective instabilities of fluidized beds. *Phys. Fluids*, 6(12):3936–3944.

Niederreiter, G. and Sommer, K. (2004). Modelling and experimental validation of pressure drop for pneumatic plug conveying. *Granular Matter*, 6:179–183.

Nieuwstadt, F. T. M. (1998). *Turbulentie (in Dutch)*. Epsilon Uitgaven.

NOAA (2015). National oceanographic data center world ocean database. Internet: http://www.nodc.noaa.gov/cgi-bin/OC5/SELECT/dbsearch.pl.

Norbury, D. (2010). *Soil and Rock Description in Engineering Practice*. Whittles publishing.

Pearson, J. S. (1975). *Ocean Floor Mining*, volume 2 of *Ocean Technology Review*. Noyes Data Corporation.

Prosperetti, A. and Tryggvason, G. (2009). *Computational Methods for Multiphase Flows*. Cambridge University Press.

Rabinovich, E., Freund, N., Kalman, H., and Klinzing, G. (2012). Friction forces on plugs of coarse particles moving upwards in a vertical column. *Powder Technology*, 219:143–150.

Rabinovich, E. and Kalman, H. (2011). Flow regime diagram for vertical pneumatic conveying and fluidized bed systems. *Powder Technology*, 207:119–133.

Ramaprian, B. R. and Tu, S. W. (1983). Fully developed periodic turbulent pipe flow. part 2. the detailed structure of the flow. *Journal of Fluid Mechanics*, 137:59–81.

Ribas, F. A. and Deschamps, C. J. (2004). Friction factor under transient flow condition. *International Compressor Engineering Conference, July 12-15, Purdue University, USA*.

Richardson, D. J. and Holdich, R. G. (2001). A novel and low cost probe for monitoring dispersed solids concentrations in liquids. *Trans. Instn. Chem. Engrs.*, 79:569–574.

Richardson, J. F. and Zaki, W. N. (1954). Sedimentation and fluidisation: part i. *Trans. Instn. Chem. Engrs.*, 32.

Rona, P. A. (2008). The changing vision of marine minerals. *Ore Geology Reviews*, 33:618–666.

Rowe, P. N. (1987). A convenient empirical equation for estimation of the richardson and zaki exponent. *Chemical Engineering Science*, 42(11):2795–2796.

Sadlej, K., Wajnryb, E., and Ekiel-Jezewska, M. L. (2010). Hydrodynamic interactions suppress deformation of suspension drops in poiseuille flow. *The Journal of Chemical Physics*, 133.

Schaufler, A., Becker, C., and Steeb, H. (2013). Infiltration processes in cohesionless soils. *Z. Angew. Math. Mech.*, 93(2):138–149.

Sellgren, A. (1982). The choice of operating velocity in vertical solid–water pipeline systems. In *Hydrotransport 8*, pages 211–226. BHRA Group.

Sharqawy, M. H., Lienhard, J. H., and Zubair, S. M. (2009). Thermophysical properties of seawater: a review of existing correlations and data. *Desalination and Water Treatment*, 16:354–380.

Shaul, S. and Kalman, H. (2014). Friction forces of particulate plugs moving in vertical and horizontal pipes. *Powder Technology*, 256:310–323.

Shook, C. A. (1988). Segregation and plug formation in hydraulic hoisting of solids. In *Hydrotransport 11*, pages 359–379. BHRA Group.

Shook, C. A. and Bartosik, A. S. (1994). Particle–wall stresses in vertical slurry flows. *Powder Technology*, 81:117–124.

Sorensen, J. A. and Glass, G. E. (1987). Ion and temperature dependence of electrical conductance for natural waters. *Analytical Chemistry*, 59(13):1594–1597.

Strauss, M., McNamara, S., Hermann, H. J., Niederreiter, G., and Sommer, K. (2006). Plug conveying in a vertical tube. *Powder Technology*, 162:16–26.

Sumner, M. E. (2000). *Handbook of Soil Science*. CRC Press.

Sumner, R. J., McKibben, M. J., and Shook, C. A. (1990). Concentration and velocity distributions in turbulent vertical slurry flows. *Ecoulements Solide Liquide*, 2(2):33–42.

Talmon, A. M. (2008). Boundary layer theory for solid-liquid mixtures tested against couette flow. *14th International Conference on Transport and Sedimentation of Solid Particles. 23-27 june, Saint Petersburg, Russia.*, pages 293–300.

Talmon, A. M. and Van Rhee, C. (2011). Test set–up for irregular vertical hydraulic transport in deep ocean mining. *ASME 30th international conference on ocean, offshore and arctic engineering*.

Taverra, F. J., Escudero, R., Gomez, C. O., and Finch, J. A. (1998). Determination of solids holdup in thickeners from measurement of electrical conductivity using flow cells. *Minerals Engineering*, 11(3):233–241.

Taylor, G. I. (1953). Dispersion of soluble matter in solvent flowing slowly through a tube. *Proceedings of the Royal Society A*, 219(1137):186–203.

Taylor, G. I. (1954). The dispersion of matter in turbulent flow through a pipe. *Proceedings of the Royal Society A*, 223(1155):446–468.

Terzaghi, K., Peck, R. B., and Mesri, G. (1996). *Soil Mechanics in Engineering Practice*. John Wiley and Sons, third edition.

Torobin, L. B. and Gauvin, W. H. (1961). The drag coefficient of single spheres moving in steady and accelerated motion in a turbulent fluid. *A.I.Ch.E. Journal*, 7(4):615–619.

Tran-Cong, S., Gay, M., and Michaelides, E. E. (2004). Drag coefficients of irregularly shaped particles. *Powder Technology*, 139:21–32.

Turner, J. C. R. (1976). Two-phase conductivity: the electrical conductance of liquid-fluidized beds of spheres. *Chemical Engineering Science*, 31:487–492.

Uijttewaal, W. S. J. and Oliemans, V. A. (1996). Particle dispersion and deposition in direct numerical and large eddy simulations of vertical pipe flows. *Phys. Fluids*, 8(10):2590–2604.

Vames, J. S. and Hanratty, T. J. (1988). Turbulent dispersion of droplets for air flow in a pipe. *Experiments in Fluids*, 6:94–104.

Van den Berg, G. and Cooke, R. (2004). Hydraulic hoisting technology for platinum mines. *International Platinum Conference 'Platinum Adding Value', The South Africa Institute for Mining and Metallurgy*.

Van Dijke, W. (2010). Vertical hydraulic transport of solids. Master's thesis, Delft University of Technology.

Van Leer, B. (1974). Towards the ultimate conservative difference scheme ii. monotonicity and conservation combined in a second order scheme. *Journal of Computational Physics*, 14:361–370.

Van Rhee, C. (2002). *On the Sedimentation Process in a Trailing Suction Hopper Dredger*. PhD thesis, Delft University of Technology.

Van Rijn, L. C. (1984). Sediment transport part ii: Suspended load transport. *Journal of Hydraulic Engineering*, 110(11):1613–1641.

Van Wijk, J. M. and Blok, B. G. (2015). The influence of grain size on the performance of conductivity concentration meters. *Flow Measurement and Instrumentation*, 45:384–390.

Van Wijk, J. M. and Smit, P. M. (2015). Design and internal flow simulation of a vertical hydraulic transport system for mining manganese nodules. *Proceedings of the Seventeenth International Conference on Transport and Sedimentation of Solid Particles, September 22-25, Delft, The Netherlands*.

Van Wijk, J. M., Van Grunsven, F., Van Rhee, C., and Talmon, A. M. (2015). Simulation and experimental proof of plug formation and riser blockage during vertical hydraulic transport. *Ocean Engineering*, 101:58–66.

Van Wijk, J. M., Van Rhee, C., and Talmon, A. M. (2014a). Axial dispersion of suspended sediments in vertical upward pipeflow. *Ocean Engineering*, 92:24–30.

Van Wijk, J. M., Van Rhee, C., and Talmon, A. M. (2014b). Wall friction of coarse grained sediment plugs transported in a water flow through a vertical pipe. *Ocean Engineering*, 79:50–57.

Vergouw, J., Gomez, C. O., and Finch, J. A. (2004). Estimating true level in a thickener using a conductivity probe. *Minerals Engineering*, 17:87–88.

Verloop, J. and Heertjes, P. M. (1970). Shock waves as a criterion for the transition from homogeneous to hetergeneous fluidization. *Chemical Engineering Science*, 25:825–832.

Verruijt, A. (2012). *Soil Mechanics*. Delft University Press.

Wallis, G. B. (1969). *One Dimensional Two Phase Flow*. McGraw-Hill.

Welling, C. G. (1981). An advanced deep sea mining system. *Offshore Technology Conference, May 4-7, Houston, Texas USA*, pages 247–257.

White, F. (2003). *Fluid Mechanics*. McGraw-Hill, fifth edition.

Wilson, K. C., Addie, G. R., Sellgren, A., and Clift, R. (2006). *Slurry Transport Using Centrifugal Pumps*. Springer Science and Media, third edition.

Winterwerp, J. C. (1999). *On the Dynamics of High–Concentrated Mud Suspensions*. PhD thesis, Delft University of Technology.

Winterwerp, J. C. and Van Kesteren, W. G. M. (2004). *Introduction to the Physics of Cohesive Sediment in the Marine Environment*, volume 56 of *Developments in Sedimentology*. Elsevier.

Xia, J. X., Ni, J. R., and Mendoza, C. (2004a). Hydraulic lifting of manganese nodules through a riser. *Journal of Offshore and Mechanics and Arctic Engineering*, 126(77).

Xia, J. X., Ni, J. R., and Mendoza, C. (2004b). Upward flow of large size particles-water mixtures through swaying pipes. *Journal of Transportation Engineering*, 535.

Yang, N., Chen, G., Tang, D., Jin, X., and Xiao, H. (2011). Behaviour of single particles and group particles in vertical lifting pipe in china. *ISOPE Conference*.

Zaki, M. and Amann, H. M. (1980). The red sea pre-pilot mining test 1979. *Offshore Technology Conference, May 5-8, Houston, Texas USA*, pages 197–210.

Zastawny, M., Mallouppas, G., Zhao, F., and Van Wachem, B. (2012). Derivation of drag and lift force and torque coefficients for non-spherical particles in flows. *Int.J. Multiphase Flow*, 39:227–239.

Zielke, W. (1966). *Frequency Dependent Friction in Transient Pipe Flow*. PhD thesis, University of Michigan.

Zou, W. (2007). Comra's research on lifting motor pump. *ISOPE Ocean Mining Symposium, 1-6 July, Lisbon, Portugal*, pages 177–170.

A

BENCHMARK TEST OF THE 1DVHT MODEL

In this Appendix the 1DVHT model is put to the test by performing a one dimensional sedimentation simulation of which experimental data is available in Van Rhee (2002). A sedimentation test is particularly suited for testing the implementation of the advection-diffusion equation, because in sedimentation large gradients in the volume fraction of solids and shock formation occur. These gradients and shocks are complex features to model, so when a succesful sedimentation benchmark can be performed the quality of the model is verified.

First, the implementation of the advection-diffusion equation is tested by neglecting the mixture momentum equation, thus solving Equation 6.7 only. To this end, the Lax Wendroff equation with Van Leer flux limiters according to Leveque (1990) is used as discussed in Section 6.3.2. It is combined with the maximum packing limiter, with $c_{v,max} = 0.53$ based on the data of Van Rhee (2002).

The transport velocities $v_{s,k}$ are modelled with Equation 6.26. The slip velocities of the solid fractions are modelled with Equation 6.32. To account for the influence of the volume fraction of solids on the settling velocity of a particle, Equation 6.27 is used with the hindered settling parameters according to Garside and Al Dibouni (1977). The outcome of the simulation is depending on the choice of the hindered settling exponent. The exponent of Garside and Al Dibouni (1977) proved to work best.

We compare the results of the advection-diffusion equation with the results of the full 1DVHT model, and we compare both simulations with experimental data. Therefor we need an experiment in which mixture dynamics can be neglected (i.e. an experiment in which only the transport of the individual fractions is significant, while the mixture in total does not move). A sedimentation experiment in a closed container would be the perfect test case.

Van Rhee (2002) describes a sedimentation experiment in a tube with $L = 1.4\,m$ and $D = 0.28\,m$. Along the height of the tube, two-point conductivity sensors were placed with a spacing of $0.12\,m$ to measure the volume fraction of solids. This sedimentation test is simulated with both the advection-diffusion and the full 1DVHT model. The particle size distribution for this case is given in Table A.1 and Figure A.1, the settings of the parameters in the numerical simulation is given in Table A.2. The solids density reads $\rho_s = 2650\,kg/m^3$, the water density reads $\rho_f = 1000\,kg/m^3$ and the dynamic water viscosity is $\mu_f = 1.1 \cdot 10^{-6}\,Pa \cdot s$. The full 1DVHT simulation uses $p = 0$ and $\partial v_m / \partial z = 0$ at the top of the container, and it uses $\partial p / \partial z = 0$ and mirrored mixture velocities at the bottom of the container.

Table A.1: Particle size distribution as used in the sedimentation simulation.

Particle diameter $[1 \cdot 10^{-6}\,m]$	$c_{v,k}/c_v$ [−]
76.5	0.02
98	0.04
115.5	0.15
137.5	0.22
163.5	0.29
194.5	0.20
231	0.06
302.5	0.02

In the experiments of Van Rhee (2002), the volume fraction of solids over the length of the tube has been measured at $t = 50\,s$, $t = 100\,s$ and $t = 150\,s$. The results of the simulations are compared with the experimental data, the results are shown in Figure A.2. Both the steady state simulation (advection-diffusion equation only with $v_m = 0\,m/s$) and the full 1DVHT model show good agreement with the experimental data. In this way

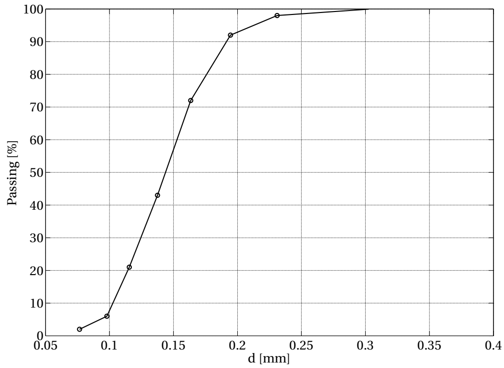

Figure A.1: Cumulative particle size distribution.

Table A.2: Settings used in the one dimensional simulation of the sedimentation test.

Parameter	**Value Steady State Simulation**	**Value 1DVHT**
L $[m]$	1.4	1.4
D $[m]$	0.28	0.28
Simulation time $[s]$	150	150
Δz $[m]$	0.0109	0.0219
Δt $[s]$	0.0957	$9.5703 \cdot 10^{-4}$
c_v $[-]$	0.32	0.32
$c_{v,max}$ $[-]$	0.53	0.53
ϵ_z $[m^2/s]$	0	0

the 1DVHT model has been verified (the full dynamic simulation gives practically the same result as the steady state simulation), and the model itself has been validated for multifraction calculations.

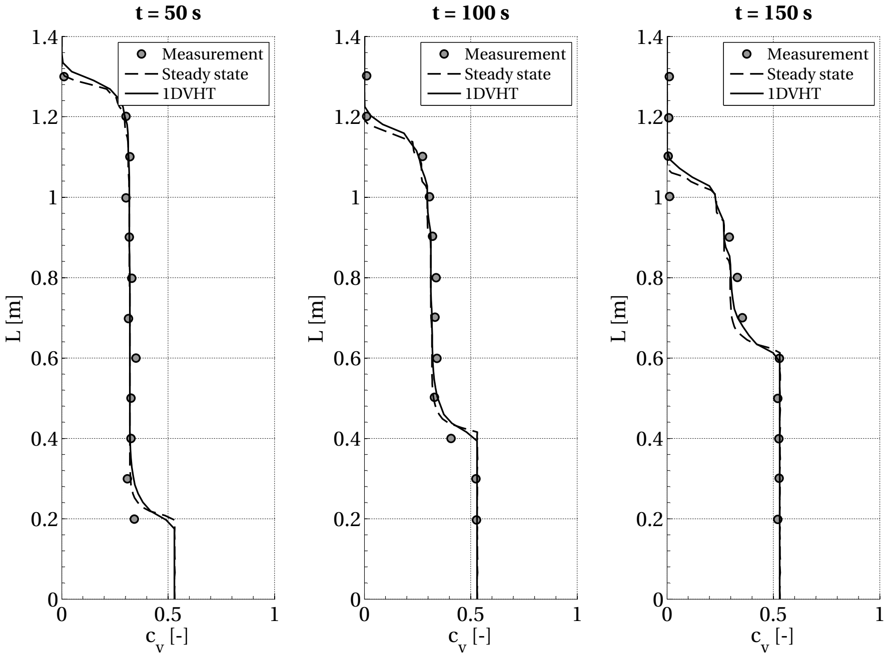

(a) $t = 50\,s$ (b) $t = 100\,s$ (c) $t = 150\,s$

Figure A.2: Simulation results of the one dimensional sedimentation test compared with measurements. The agreement between measurement and simulation is good for both the steady state simulation ($v_m = 0\,m/s$) and the 1DVHT simulation (v_m calculated).

B

The influence of grain size on the output of Conductivity Concentration Meters

The use of conductivity as a means to determine the volume fraction of solids in a suspension of poorly conductive solids in water combines the benefits of high sampling rates and ease of use at the cost of a high sensitivity to salinity and fluid temperature. In this appendix we investigate a custom built CCM, to which a third parameter was found to be of much influence: the grain size of the suspended phase. This appendix describes a calibration experiment with which the influence of grain size on the CCM output has been investigated. The data give rise to an alternative calibration curve which is different from the regular effective media theories.

This appendix has been published in Flow Measurement and Instrumentation **45** (2015) Van Wijk and Blok (2015).

B.1. INTRODUCTION

The electrical conductivity of a fluid containing suspended particles depends on the conductivity of the fluid and the volume fraction of the suspended particles. The larger the volume fraction of the suspended particles, the more the conductivity of the mixture is affected. In the research reported here the electrical conductivity of the suspended particles is very small compared to the conductivity of the fluid. Adding such particles to fluid (water) in a measuring volume forces the measured conductance to a lower value as long as the particles remain well distributed over the entire volume.

By measuring the electric conductance or electric resistance of a mixture, it is thus possible to get information about the volume fraction of the different individual phases in the mixture. There is a wide range of application for this technique, for instance in wellbore logging in the oil and gas industry or the measurement of the volume fraction of suspended solids in a mixture of water and solids. The latter application has been mainly concerned with suspensions or slurries with fine material.

Nasr-El-Din et al. (1987) describe an intrusive conductivity probe that is testsed with spherical glass beads and irregularly shaped particles. Although the conductivity measurement was expected to be dependent on the flow velocity, their results were not sensitive to velocity changes. The electrodes in the probe have a spacing of $1\,mm$, and for particles with $d > 1\,mm$ it proved that the Maxwell model is not valid. MacTaggart et al. (1993) describe an improved version of the intrusive probe of Nasr-El-Din et al. (1987) and use it for measuring the volume fraction of solids with $d < 1\,mm$ in a mixing tank. It proved again that the results were independent of the rotational speed of the stirrer, and it proved that monitoring the background conductivity (i.e. carrier fluid conductivity) is preferred to improve the results.

Holdich and Sinclair (1992) use a different approach by mounting two electrodes opposite of a pipe. Multiple pairs were placed along the length of a $D = 65\,mm$ pipe, which was used for a sedimentation experiment. This method is non intrusive so it will not affect the experiment, but the electric field of the electrodes was found to be influenced by the pipe wall, which gave poor reproducibility of the results. A similar setup was used in Glasserman et al. (1994) to measure the volume fraction of solids (the maximum d/D being $1/17$) in a fluidized bed setup with $D = 50\,mm$. The electrodes were curved stainless steel plates placed opposite of eachother on the fluidization column. No influence of the pipe wall is reported, and the volume fraction of solids based on the conductivity measurement agreed very well with reference measurements based on the inserted mass of solids. The work of Holdich and Sinclair (1992) was continued in Richardson and Holdich (2001) by designing an intrusive probe which could simultaneously measure the mixture conductivity and the background conductivity, thus solving the problem of MacTaggart et al. (1993) as well. The use of intrusive conductivity probes is common practice in the field of mineral processing for monitoring the bed height in thickeners (Taverra et al., 1998; Vergouw et al., 2004; Acuna et al., 2014).

Although many industrial applications are concerned with mixtures of fine material in a carrier liquid, there are exceptions to this case. Since the 1960's deep sea mining is being considered as a viable alternative for terrestial mining, and laboratory research and technology development in this field are still progressing (Chung, 2009). In deep sea mining, the vertical hydraulic transport of the excavated material from seafloor to sea surface over a distance of hundreds to thousands of meters is a key operation. The excavated deposits are large, with d/D up to 1/5, hence laboratory experiments in this field are concerned with relatively large particles as well (Xia et al., 2004a; Yang et al., 2011; Van Wijk et al., 2014a).

The authors are concerned with laboratory scale vertical hydraulic transport experiments of large particles, in which the determination of the in situ volume fraction of solids (up to $c_v \approx 0.6$) at cross sections along the riser is the most important aspect. Conductivity concentration meters are well suited considering the operational range of c_v and the high sampling rates, but their use in combination with relatively large particles (in terms of d/D) has to be investigated in more depth.

B.2. THE CONDUCTIVITY CONCENTRATION METER

Individual particles will not be noticed when the particles are small relative to the size of the measuring volume and the electrodes used to measure the conductance, so the mixture will act electrically homogeneously. If the particles and the electrodes have dimensions of the same order of magnitude, then the measured conductivity will also vary with the position of the particles relative to the electrodes. In that case the measured conductivity will not only depend on the concentration of the suspended matter but also on the ever changing positions of the particles, in particular those close to the electrodes.

The electrical conductance between two electrodes depends on to what extent the current can spatially develop between the electrodes. Would the current be confined to a narrow corridor between the electrodes, then a smaller conductance will be observed than in the case the current can fully spread between the electrodes. When used inside a pipe, the current is confined to some extent, hence the observed conductance will not reach the maximum level.

The Conductivity Concentration Meter used in this research is designed and built by Deltares, The Netherlands. It is based on their standard devices for measurement of the volume fraction of sand particles in different laboratory and commercial applications. The current design has been proposed for the use in vertical hydraulic transport experiments with relatively large particles. The device consists of four pairs of platinum electrodes, placed opposite of each other in the cross section of a pipe section with internal diameter $D = 99.4\,mm$. The PVC pipe is non-conducting so the pipe wall limits the spatial extent of the electrical current. The sensor electrodes are mounted flush with the inside of the pipe wall. The electrodes are manufactured of 4 mm diameter platinum rod. Platinum is chosen for the electrical stability of its metal-water interface.

As mentioned, the measured conductance not only depends on the volume fraction of suspended particles but also on the particle size in relation to the electrode size. The design particle size for this device is $d = 15\,mm$, but in the calibration experiments this range is extended. To limit the influence of particle size, the electrode surface area exposed to the fluid was increased by combining the electrodes in sets of four. This approach also reduces the effect of the spatial distribution of the particles. After all, a particle close to an electrode cannot be close to any of the other electrodes. The configuration is depicted in Figure B.1. The configuration thus obtained effectively consists of two electrodes.

The electrode pairs are subjected to an alternating voltage (sinusoidal). The aver-

(a) Exterior view of the CCM.

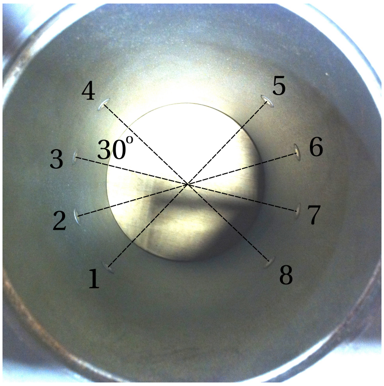

(b) Interior view of the CCM

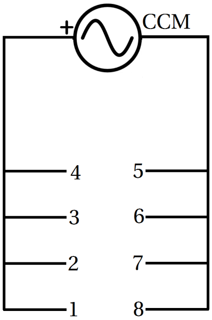

(c) Electric scheme of the CCM

Figure B.1: The Conductivity Concentration Meter as used in the experiments.

age voltage, i.e. the DC component, is kept zero to avoid polarisation of the electrodes. The CCM electronics supports 16 channels, so alternative connections between pairs are possible. Combining electrodes 1-5, 2-6, 3-7, 4-8 for instance could provide information about the spatial distribution of the suspended sediment. Other combinations could also be made, e.g. 1-5, 1-6, 1-7 and 1-8 and also 2-5, 2-6, 2-7, and 2-8, and so on. By making various combinations more detailed information about the spatial and temporal distribution of the suspended particles could be obtained. This is especially interesting for future work, but it is outside the scope of our present research.

The relation between electrical conductivity and the volume fraction of individual phases is often modelled with the Effective Medium Theory, which treats the mixture as a continuum (Choy, 1999). The CCM output is related to conductivity by calibration of the fluid phase. The conductivity of the fluid phase is denoted k_f, the conductivity of the mixture is denoted k_m. According to the effective medium approach, the fluid conductivity k_f and mixture conductivity k_m are related by the volume fraction of solids c_v.

The review of Banisi et al. (1993) points out that the models of Maxwell (for monodisperse mixtures of spheres), Bruggeman (for wide particle size distributions) and Fricke (for spheroids) are the most obvious choices for conductivity concentration meters. Although the theoretical grounds of the Maxwell model sets an upper limit to the volume fraction of solids of $c_v = 0.2$, in practice it proves to perform well up to $c_v = 0.5$, and it is therefor commonly used (Turner, 1976; Nasr-El-Din et al., 1987; Banisi et al., 1993; Glasserman et al., 1994).

The Maxwell model, for non-conductive solids reads:

$$\frac{k_m}{k_f} = \frac{2 - 2 \cdot c_v}{2 + c_v} \tag{B.1}$$

An alternative to Equation B.1 is the empirical Archie Equation, which has its origin in the oil and gas industry (Archie, 1942):

$$\frac{k_m}{k_f} = (1 - c_v)^{\xi} \tag{B.2}$$

The exponent ξ in Equation B.2 is determined empirically. For sand it is found $1 < \xi < 2$.

The conductivity of water shows a linear relation with the water temperature (Sorensen and Glass, 1987). The relation between conductivities at different temperatures is given by:

$$\frac{k_{f,T}}{k_{f,T_0}} = 1 + \alpha \cdot (T - T_0) \tag{B.3}$$

In Equation B.3 the conductivity at temperature T is denoted $k_{f,T}$, the conductivity at reference temperature T_0 is denoted k_{f,T_0} and $\alpha = 0.02$ (Hem, 1985).

B.3. SENSITIVITY TO GRAIN SIZE VARIATIONS

The grain size dependency first emerged in a series of experiments at the MTI Holland Laboratory, see Van Wijk et al. (2014a). In these experiments single batches of sediment were transported through a $D = 99.4\,mm$ vertical pipe, in which four CCM devices were mounted, see Figure 3.1. A centrifugal pump induced a flow of water with average velocity $v_f \approx 2\,m/s$, after which a batch of sediment was launched in the riser. The propagation of a batch has been recorded by the four CCM devices.

The single batch experiments have been checked in hindsight for conservation of mass, i.e. to check whether the measured volume fraction of solids is quantitatively correct. The mass passing a CCM can be found by calculating:

$$m = \rho_s \cdot A \cdot \int_t v_s(t) \cdot c_v(t)\,dt \tag{B.4}$$

The volume fraction of solids $c_v(t)$ is measured with a CCM, but $v_s(t)$ can only be estimated from the time interval between a batch passing two CCM's: $v_s(t) \approx \overline{v_s}$ with $\overline{v_s}$ found by cross-correlation of the $c_v(t)$ and time data. This procedure is only valid when the batch velocity is (approximately) constant. By means of cross correlation the average batch velocity has been determined for the sections between CCM1-CCM2, CCM2-CCM3 and CCM3-CCM4. Figure B.2 shows the results, where the CCM1-CCM2 trajectory is denoted 1, the CCM2-CCM3 trajectory is denoted 2 and the CCM3-CCM4 trajectory denoted 3. As can be seen the velocities do not change significantly between the last two sections, so in the analysis we use the data from the third trajectory (CCM3-CCM4) where the assumption $v_s(t) \approx \overline{v_s}$ is valid.

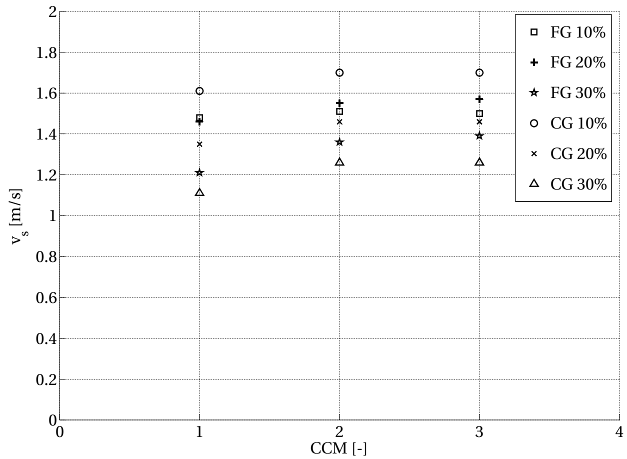

Figure B.2: Batch velocities between CCM1-CCM2, CCM2-CCM3 and CCM3-CCM4 (Figure 3.1) for the fine gravel (FG) and coarse gravel (CG) experiments. In the last section, the velocity is approximately constant.

The procedure of finding m is illustrated with Figure B.3. Since the mass m_i inserted in the system is accurately known by measurement in advance, quantitative correctness can be checked by comparing m and m_i.

When this procedure is applied to the single batch experiments with fine sand, coarse sand, fine gravel (FG) and coarse gravel (CG), the results as shown in Figure B.4 are obtained. The data was obtained by using Equation B.1. The differences between the inserted mass m_i and measured mass m_m is large for every particle type. It can be seen that the larger the particle, the larger the deviation between the inserted mass and the measured mass. The particle sizes are $d_{50} = 0.389\,mm$ for fine sand, $d_{50} = 1.05\,mm$ for coarse sand, $d_{50} = 6.34\,mm$ for fine gravel and $d_{50} = 11.20\,mm$ for the coarse gravel. The density of the sediments is $\rho_s = 2650\,kg/m^3$.

Since the relatively large particles are of special interest for experimental research into vertical hydraulic transport for deep sea mining, there is a need for improved calibration.

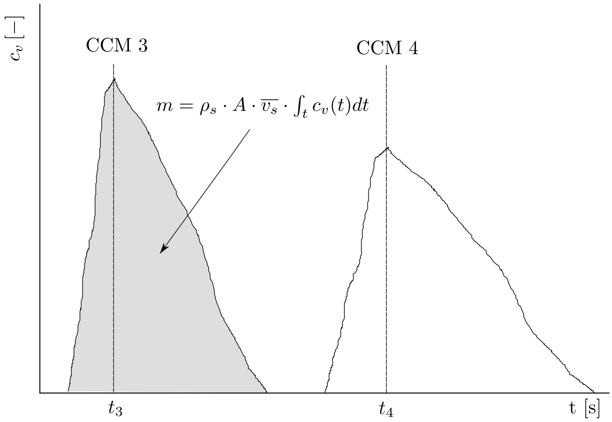

Figure B.3: Example of the procedure of finding the mass m passing two CCM's.

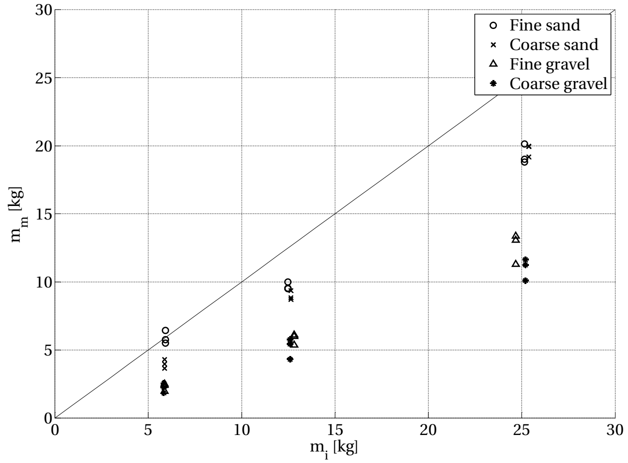

Figure B.4: Measured mass m_m versus the inserted mass m_i of the single batch experiments. The data has been obtained using Equation B.1.

B.4. CALIBRATION OF THE CCM FOR DIFFERENT GRAIN SIZES AND VOLUME FRACTIONS OF SOLIDS

B.4.1. CALIBRATION METHOD

The calibration needs a large range of c_v values, but since a dependency on d is expected, the particle diameter needs to be varied as well. The properties of the particles used in the calibration are summarized in Table B.1.

The calibration is done by means of fluidization. A schematic view of the setup is shown in Figure B.5. The test setup has an internal diameter of $D = 99.4\,mm$. In the

Table B.1: Properties of the particles used for calibration of the CCM. In case of sediment, the particle size is the d_{50}. The ratio d/D is based on the fluidization setup internal diameter of $D = 99.4\,mm$.

Particle type	**Particle size** $[mm]$	d/D [-]	ρ_s $[kg/m^3]$
Fine gravel	$6.34\,mm$	0.063	2650
Coarse gravel	$11.20\,mm$	0.11	2650
Glass bead	$10.0\,mm$	0.10	2520
Glass bead	$12.8\,mm$	0.13	2530
Glass bead	$14.0\,mm$	0.14	2570
Glass bead	$15.7\,mm$	0.16	2490
Glass bead	$20.0\,mm$	0.20	2510
Glass bead	$24.5\,mm$	0.25	2660
Glass bead	$24.8\,mm$	0.25	2660

upward pipe a flow straightener, a grid and the CCM are mounted. The flow straightener consists of a bundle of pipes which attenuates the rotation in the flow. The grid is used to support the batch of particles at the start of an experiment. The setup has a Krohne Optiflux electromagnetic flow sensor with a range of $v_f = \pm 12\,m/s$ and a temperature sensor. For the data acquisition a Dataq DI-720 interface is used. Along the riser a ruler is mounted (with mm scale) which is used to measure the expanded bed height. The expanded bed height h is related to the volume fraction of solids by the inserted mass m_i, the solids density ρ_s and the cross sectional area of the riser A:

$$c_v = \frac{m_i}{\rho_s \cdot A \cdot h} \tag{B.5}$$

The fluidization experiment follows the following procedure. A batch of particles is inserted at the top section of the riser by opening the valve and letting the particles settle on the grid, see Figure B.5. Then the fluid velocity range is explored by increasing the flow towards the point where the first particles start leaving the setup at the top section of the riser (towards the hopper). The bulk velocity at this stage is close to the terminal settling velocity of a particle. Since the fluid velocity in the riser and the volume fraction of solids are inversely related (Richardson and Zaki, 1954), the velocity associated with this point is the upper limit of an experiment, and the associated volume fraction of solids thus is the lower limit. The velocity is the controlled parameter, and its range is divided in ten steps typically.

Each calibration experiment follows a standard procedure. First the fluid conductivity and temperature are measured with a Greisinger GMH 3430 portable conductivity meter (its conductivity range is set $0-2000\,\mu S/cm$, its temperature range is set $5-100^oC$ and its resolution is $0.1\,\mu S/cm$ and 0.1^oC). Then the CCM output voltage, for fluid only, is measured for about $2\,s$ and checked with the Greisinger output. The conductivity is converted to the reference temperature $T_0 = 25^o$ with Equation B.3. Then the conductivity of the mixture is measured with the CCM, the temperature of the mixture is measured, and the conductivity again is converted to the reference temperature $T_0 = 25^o$ using Equation B.3. This conversion is based on the assumption that the presence of solids does not influence the constant of proportionality in Equation B.3.

Before starting the experiments, the relation between k_f and the output voltage V_{out}

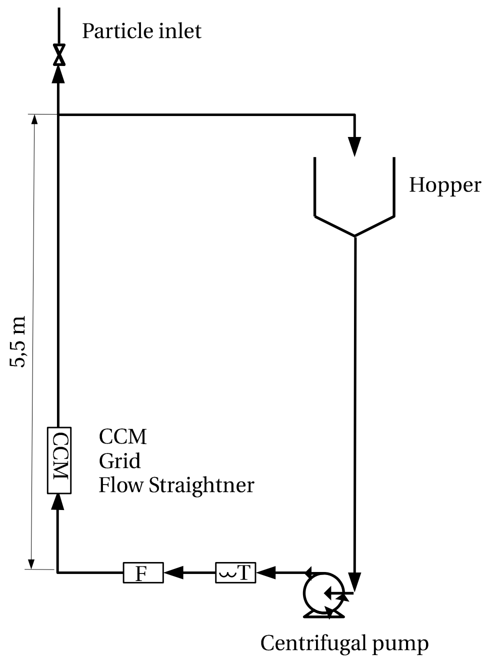

Figure B.5: The experimental setup used for the fluidization experiment.

of the CCM device has been investigated using demineralized water. By filling the CCM (blinded on one side) with tap water and by adding demineralized water in four steps, Figure B.6 was obtained.

B.4.2. RESULTS

The results of the calibration are shown in Figure B.7. The calibration curves are totally different from Equations B.1 and B.2, lying far above the line $c_v = 1 - k_m/k_f$.

For the purpose of the analysis, an alternative relation is introduced:

$$\frac{k_m}{k_f} = 1 - c_v^{\zeta} \tag{B.6}$$

Note that Equation B.6 is the Archie equation mirrored on the line $k_m/k_f = c_v$. It proves that $\zeta = 1.59$ gives a reasonable fit through all the data, but since a dependency of the CCM output on d/D is expected, the exponent ζ will be specified for each experiment.

To this end, a least square fit is made of the form $c_v = (1 - k_m/k_f)^{1/\zeta}$ using the data of the glass bead experiments (Table B.1). This excercise yields the data as shown in Figure B.8. The linear approximation of $\zeta(d/D)$ is given by:

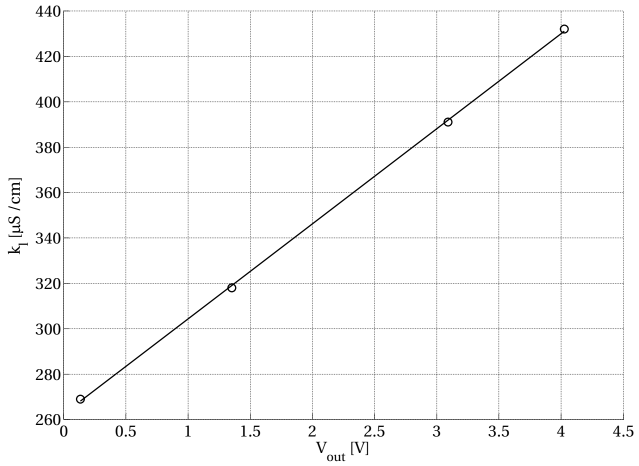

Figure B.6: CCM output as measured with tap water and demineralized water at $T = 10.3\,^oC$. The least square fit through the data reads $k_f = 41.89 \cdot V_{out} + 262.4$.

$$\zeta = 1.457 + 0.689 \cdot \frac{d}{D} \tag{B.7}$$

Equation B.7 is valid on the domain $0.1 < d/D < 0.3$. For the coarse gravel fluidization experiment $\zeta = 1.49$ is found, Equation B.7 gives $\zeta = 1.50$.

B.5. DISCUSSION: RELATING MIXTURE CONDUCTIVITY AND VOLUME FRACTION OF SOLIDS

The data shows a trend very different from the classic calibration curves, and no other reference could be found in literature in which this is the case. The trend in the data is very consistent. In finding a suitable calibration curve, the first step was to look at Equation B.6. A dependency of the exponent ζ on d/D was found, and a very reasonable fit was obtained.

For practical application there is a downside to Equation B.6 with $\zeta > 1$. Minor fluctuations in fluid and mixture conductivity were encountered due to local temperature gradients at the start of a test or small quantities of dissolved matter, which could result in $k_m > k_f$. The excess regularly is only very small (order of tenths of percents), but already sufficient to give $(1 - k_m/k_f) < 0$ so complex roots occur. Analysis of the single batch experiments suffered from this problem and therefor in the implementation of Equation B.6 the ratio k_m/k_f has been substituted by $min\left(1, k_m/k_f\right)$.

The new calibration will be used to recalculate the results of Figure B.4. For the fine sand an coarse sand, a linear relation between k_m/k_f and c_v is assumed. For the fine gravel and coarse gravel Equation B.6 is used with Equation B.7 for ζ. It proves that the

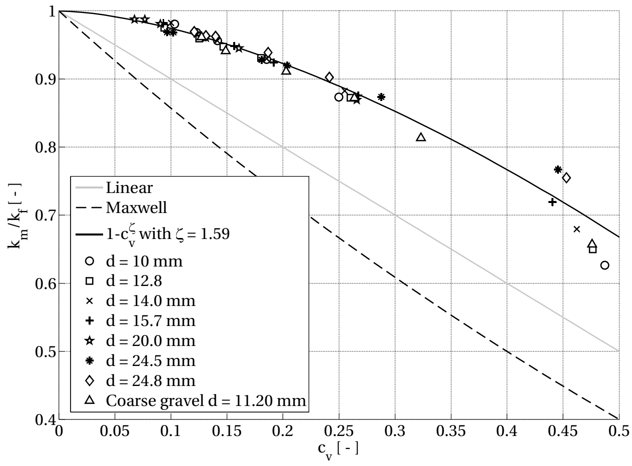

Figure B.7: The results of the calibration with a fluidization test compared with Equations B.1, B.2 and B.6. The data lies above the $c_v = 1 - k_m/k_f$ line, it is approximated reasonably well with $\zeta = 1.59$.

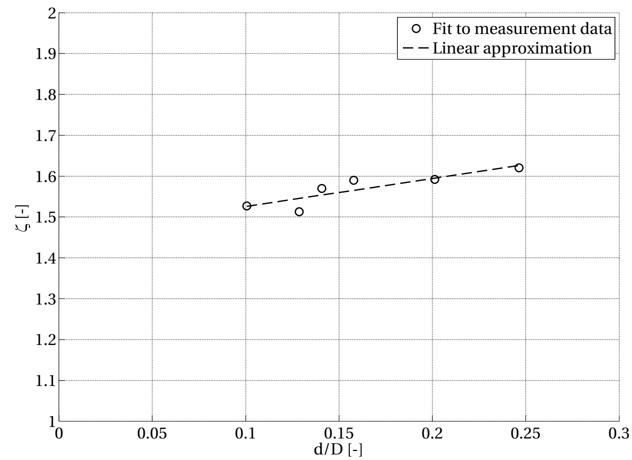

Figure B.8: When the fluidization data is fit to Equation B.6 for each d/D individually, the values of ζ can be approximated by a linear fit, Equation B.7.

fine sand an coarse sand data fit to the $m_m = m_i$ perfectly in Figure B.4, but the masses of the fine and coarse gravel fractions are overestimated.

The sensitivity to the choice of ζ is rather large, and the results of the fine and coarse gravel batch transport tests can be largely improved by chosing $\zeta \approx 1.3$ instead of $\zeta \approx 1.5$, which is also included in Figure B.9. Since a batch of gravel contains differently sized and shaped particles, in a fluidization experiment the smaller particles will be in the upper side of the column while the largest particles remain at the bottom. In Equation B.7 the d_{50} of the batch is used, while at the CCM plane there might be a different dominant particle diameter due to the nature of the fluidization experiment. Furthermore, particle shape is expected to play a role, and the large variation in particle shapes is likely to result in variation of ζ as well.

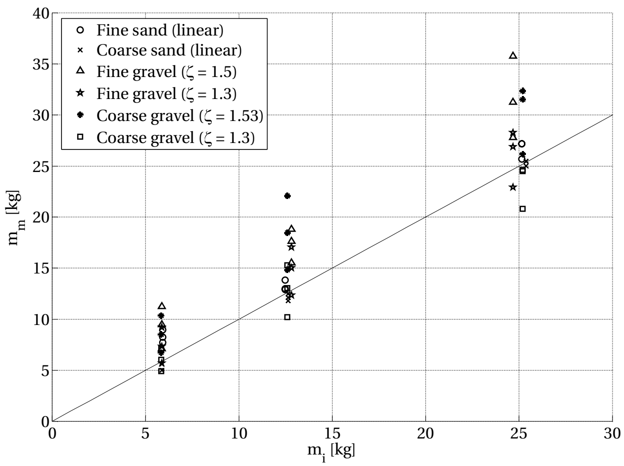

Figure B.9: Measured mass m_m versus the inserted mass m_i of the single batch experiments. The fine sand and coarse sand data has been obtained using a linear calibration $c_v = 1 - k_m/k_f$, the fine gravel and coarse gravel data has been obtained using Equation B.6 with ζ according to Equation B.7 and $\zeta = 1.3$.

B.6. CONCLUSIONS AND RECOMMENDATIONS

The output of conductivity concentration meters has been shown to depend on particle size. For particles with a diameter up to $d_{50} \approx 1.0\,mm$, the classic effective medium theories still hold (e.g. Bruggeman, Maxwell, Archie up to a linear relation $c_v = 1 - k_m/k_f$), but for larger particles it was found that the relation between c_v and k_m/k_f could be totally different.

The fluidization experiment as described in Section B.4.2 shows that a calibration curve of the form $k_m/k_f = 1 - c_v^{\zeta}$ approximates the fluidization experiments best. It was found that for glass beads ζ depends on d/D by an approximately linear relation.

The new calibration curve was tested against a transport experiment which shows an improvement over the use of the Maxwell equation. When ζ is used according to the linear approximation, the CCM output overestimates the volume fraction of solids. When ζ is chosen about $10-15\%$ smaller than predicted by the linear approximation (e.g. $\zeta = 1.3$), the calibration curve shows good results.

Besides particle size, the particle shape and particle size distribution are expected to play a role. In this appendix these effects are included by tuning ζ in the case of the gravel transport experiments, but a more extensive set of experiments is recommended to investigate the influence of these additional parameters.

The configuration as used in this research project consists of four pairs of electrodes, coupled in such a way that one pair of two virtual electrodes results. The virtual electrodes cover a part of the pipe's circumference, so the shortest distance from one electrode to the opposite is not constant. Calibration with water has shown that this configuration does work well for well mixed media (i.e. almost perfect continua), but when a mixture contains large particles, there could be preference paths of least resistance along the circumference of the pipe, where the volume fraction of solids is smallest due to geometrical constraints. This would be an interesting topic for further investigation, and modelling the currents in the CCM plane is recommended for this can provide more insight in the influence of both relative particle size and particle orientation with respect to the electrodes.

List of Publications

Journal publications

4. **J.M. van Wijk, B.G. Blok**, *The influence of grain size on the performance of conductivity concentration meters*, Flow Measurement and Instrumentation **45**, 384–390 (2015).

3. **J.M. van Wijk, F. van Grunsven, A.M. Talmon, C. van Rhee**, *Simulation and experimental proof of plug formation and riser blockage during vertical hydraulic transport*, Ocean Engineering **101**, 58–66 (2015).

2. **J.M. van Wijk, C. van Rhee, A.M. Talmon**, *Axial dispersion of suspended sediments in vertical upward pipe flow*, Ocean Engineering **94**, 20–30 (2014).

1. **J.M. van Wijk, C. van Rhee, A.M. Talmon**, *Wallfriction of coarse grained sediment plugs transported in a water flow through a vertical pipe*, Ocean Engineering **79**, 50–57 (2014).

Conferences

4. **J.M. van Wijk, P.M. Smit**, *Design and internal flow simulation of a vertical hydraulic transport system for mining manganese nodules*, Seventeenth International Conference on Transportation and Sedimentation of Solid Particles, 22-25 September, Delft, The Netherlands (2015).

3. **J.M. van Wijk, C. van Rhee, A.M. Talmon**, *Advances in the modelling of vertical hydraulic transport by a continuum approach*, WODCON 2013 World Dredging Conference, The Art of Dredging, 3-7 June 2013, Brussels, Belgium.

2. **J.M. van Wijk, A.M. Talmon, C. van Rhee**, *Flow assurance of vertical solid-liquid two phase riser flow during deep sea mining*, Offshore Technology Conference 2012, 30 april - 3 May 2012, Houston, Texas, USA.

1. **J.M. van Wijk, P.M. Vercruijsse, P.A. Lucieer, A.M. Talmon, C. van Rhee**, *An experimental and numerical study of vertical hydraulic transport for deep sea mining applications*, CEDA Dredging Days 2011, Dredging and Beyond, 10-11 November 2011, Rotterdam, The Netherlands.

Magazines

2. **J.M. van Wijk, S.A. Miedema, C. van Rhee**, *Meeting the challenges of deep sea mining*, Sea Technology March, 40–42 (2012).

1. **J.M. van Wijk**, *Onderzoek naar knelpunten vertical hydraulisch transport diepzee*, Offshore Visie **4**, 32–33 (2012).

SUBMITTED

1. **J.M. van Wijk, A.M. Talmon, C. van Rhee**, *Stability of vertical hydraulic transport processes for deep ocean mining: an experimental study*, Ocean Engineering (2015).

ACKNOWLEDGEMENTS

Op een zonnige middag in oktober 2010 wandelde ik het laboratorium van IHC MTI binnen. Ik had zojuist groen licht gekregen om een paar maanden onderzoek te doen naar verticaal hydraulisch transport voor diepzee mijnbouw toepassingen, en mijn eerste actie zou een experimentje zijn. Onderweg naar het lab had ik een aantal stenen uit de bedrijfstuin meegenomen, en op die bewuste middag heb ik ze in een bak met water laten vallen om wat gevoel te krijgen voor de materie.

We wilden graag weten hoe je het verticaal transport proces goed kan modelleren, en nog belangrijker was de vraag of een verticaal-transportsysteem verstopt kan raken. Dit zijn grote vragen, en die paar maanden onderzoek werden uiteindelijk enkele jaren werk, en die paar stenen werden uiteindelijk een uitgebreid proevenprogramma. Het resultaat heeft u nu in handen.

Promoveren doe je niet alleen. Ik wil Henk van Muijen, Robert van de Ketterij en Robert Plat van het MTI bedanken dat zij mij alle ruimte gaven voor dit onderzoek. Op de TU hadden Cees van Rhee en Arno Talmon inmiddels al enkele gedachten gevormd over het mogelijk blokkeren van een verticaal transportsysteem onder extreme beladingscondities. In dit promotie-onderzoek konden we zowel hun blokkadehypothese toetsen als simulatiegereedschap maken voor IHC, met het gedeelde belang om maximale stromingszekerheid te garanderen in verticaal-transportsystemen. Cees en Arno wisten mij bij hardnekkige vraagstukken precies weer de juiste richting te wijzen, soms met slechts een paar suggesties, soms door lange discussies. Bedankt voor de fijne samenwerking en jullie enthousiasme voor het onderzoek, ik heb ontzettend veel van jullie geleerd.

Ik kijk terug op een mooie periode in de vakgroep Offshore and Dredging Engineering waar ik me enkele dagen per week kon terugtrekken uit de bedrijvigheid van de industrie, om met collega's de stand van zaken in de wereld te beschouwen en de finesses van zand-water mengsels onder de loep te nemen. Collega's, bedankt!

Een groot deel van het werk dat in dit proefschrift beschreven is bestaat uit experimenteel onderzoek. Ruben van der Vet, Thomas Fonville, Pieter Smit, Frans van Grunsven, Thomas Combe, Axel Smit, Tom Corstjens en Rian Oudewortel, bedankt voor jullie enorme inzet, enthousiasme en de vele discussies. Zonder jullie bijdrage had slechts een fractie van de proeven uitgevoerd kunnen worden en hadden we zeker niet zo ver gekomen.

We hebben diverse experimenten bedacht, en naarmate het project vorderde werden de benodigde proefopstellingen steeds groter. Ik wil Yarno Ketting, Henk Verhoeven en de mannen van de Meetdienst bedanken voor de ondersteuning bij het bouwen van alle proefopstellingen.

Tot slot: lieve familie, ouders, José en Joris, bedankt.

Curriculum Vitæ

Jort Merijn van Wijk

14-01-1986	Born in Dordrecht, The Netherlands.

Education

1990–2004	Elementary School Atheneum, C.S.G. De Lage Waard, Papendrecht (1998–2004)
2004–2009	B.Sc. Mechanical Engineering (2004 – 2007) M.Sc. Offshore and Dredging Engineering, with honours (2008–2009) Delft University of Technology
2011–2015	PhD. Offshore and Dredging Engineering Delft University of Technology *Thesis:* Vertical hydraulic transport for deep sea mining - a study into flow assurance *Promotor:* Prof. dr. ir. C. van Rhee *Co-promotor:* dr. ir. A. M. Talmon

Work Experience

2010 – 2014	Research Engineer, IHC MTI (Royal IHC)
2015 – present	Senior Research Engineer / Team Lead Laboratory and Measuring and Diagnostics department, IHC MTI (Royal IHC)

At the bottom of our oceans, kilometers below the sea surface, large amounts of metal-rich deposits are found. These deposits are seen more and more as an alternative for terrestrial resources.

One of the technological challenges in deep sea mining is the vertical hydraulic transport of the material from the seafloor to the sea surface. Flow assurance is vital to the entire mining operation.

How to model long distance transport? What about flow stability? Can solid plugs develop? How much pressure is needed to overcome a blocked riser? And how to design for flow assurance?

ISBN 978-90-9029-540-4